DRAPER LABORATORY

EXTRACTION OF ANTIPARTICLES CONCENTRATED IN PLANETARY MAGNETIC FIELDS

JAMES BICKFORD
PRINCIPAL INVESTIGATOR
jbickford@draper.com

NIAC PHASE II
YEAR 1 REPORT

AUGUST 2007

555 TECHNOLOGY SQUARE
CAMBRIDGE, MA 02139

TABLE OF CONTENTS

ACKNOWLEDGEMENTS

I would like to thank the numerous individuals and organizations that participated in one form or another in this exciting effort. The program would not have succeeded without the contributions of many people. First, I would like to acknowledge the NASA Institute for Advanced Concepts, which generously funded our effort. It is unfortunate the organization is now closing since it fostered a unique atmosphere for promoting groundbreaking space research. I will miss the lively interactions and stimulating conversations found at the NIAC meetings.

I also owe a special debt of gratitude to the entire technical team who enabled the program to succeed. William Schmitt (radiation transport analysis) and Walther Spjeldvik (positron and magnetosphere modeling) were integral parts of both the phase I and phase II efforts. Daniel Zayas and his MIT advisor Ray Sedwick joined the phase II effort and focused on modeling the system which enables the tenuous antiproton flux to be collected efficiently. Daniel's work is in partial fulfillment of his MS degree in aerospace engineering. Manuel Aleman, a MIT undergraduate researcher, also participated in the collector modeling effort. Harlan Spence from Boston University provided great insights to the team throughout the program.

I would also like to thank the numerous individuals within Draper who helped in one capacity or another. Linda Fuhrman, John West, Joe Kochocki, Don Fyler, Darryl Sargent, Seamus Tuohy, Chris Trainor, Phil Hipol, and Brendan Crowley all lent their skills to assist during the past year. Finally, I would like to thank my friends and family who supported me throughout. In particular, I'd like to thank my wife Shari for listening to all my stories and providing valuable feedback.

Jim Bickford
Cambridge, MA
August 31, 2007

CHAPTER 1 – BACKGROUND AND SUMMARY

OVERVIEW

Antiparticles are the exotic counterparts of the traditional matter that forms all objects we encounter in everyday life. Though there is no definitive reason for nature favoring one form over another, the observable universe appears to be comprised almost exclusively of traditional protons, neutrons and electrons. However, antiparticles are quite real and have been measured in both the laboratory and natural environment. Among the hundreds of other sub-atomic particles that can be formed during high-energy nuclear collisions, antiprotons, antineutrons and positrons are created in nature as well as with Earth-based particle accelerators. Figure (1.1) shows the flux of antiprotons found in the cosmic ray background, which is pervasive throughout our galaxy and beyond.

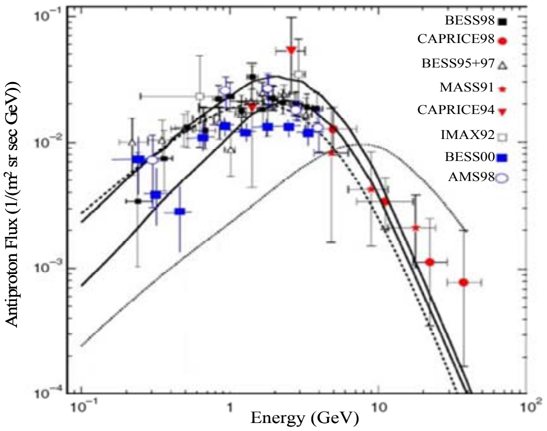

Figure 1.1 – Measured GCR antiproton spectrum. (Picozza and Morselli, 2003)

When a particle and antiparticle come into contact, they annihilate to release all of their rest mass as energy. This process is more than two orders of magnitude more efficient than nuclear reactions (fission/fusion) and ten orders of magnitude more efficient than chemical reactions. Antiparticles are the densest form of energy storage known. This very property is what makes antimatter so valuable. The particles have enormous potential in a variety of applications due to the energy that is easily released during annihilation. In particular, it has been suggested that tens of nanograms to micrograms of antiprotons can be used to catalyze nuclear reactions and propel spacecraft to velocities up to 100 km/sec. This is well beyond the capability of traditional chemical propellants and opens up new exciting options for space exploration. Larger supplies of antiprotons would eventually enable spacecraft capable of relativistic velocities. In addition, numerous other uses for antimatter have been proposed which span areas such as medicine, sensors, and pure science.

The conventional techniques used to generate and trap antiparticles are extremely inefficient since they rely on extracting antimatter from sub-atomic collision debris in particle accelerators. The worldwide output is currently in the low nanogram per year range at an estimated cost of ~$100 trillion per gram. The antiparticles are extremely difficult to control since they annihilate on contact with traditional matter. The generated particles must be stored in a high vacuum environment and levitated in magnetic, electric and/or RF fields to avoid having them annihilate with the container holding them.

In comparison, high-energy galactic cosmic rays (GCR) bombard the upper atmosphere of planets and material in the interstellar medium to naturally generate antiparticles through pair production. The antimatter is created by converting the kinetic energy of the incident GCR particle into mass during a high-energy collision with another particle. The GCR background represents a nearly infinite source of antiprotons though the natural flux is extremely tenuous, making it difficult to collect a large number of particles with conventional systems. Though a kilogram of antiprotons enters our solar system each second, only a few grams will reach the general vicinity of the Earth in a year. However, the properties of the natural environment surrounding planets with magnetic fields can generate much larger fluxes as the particles interact with the magnetic field and atmosphere.

In this report, we review the natural sources of antiparticles in our solar system and evaluate systems for extracting them for beneficial use. We focus on antiprotons since they are the most useful for the applications being considered, though fluxes of positrons and antineutrons are also discussed. The maximum fluxes, trapped mass, and replenishment rates were calculated for all major solar system bodies. Surprisingly, the radiation belts around the Earth provide the most intense localized source of antiprotons with a maximum flux of nearly 4000 $m^{-2}s^{-1}$ due to the trapping ability of the Van Allen radiation belts. However, the greatest total supply of antiprotons is the magnetosphere of Saturn. Reactions in the rings inject nearly 250 micrograms per year into the magnetosphere of the planet.

The available antiproton supplies in our solar system exceed the nanogram to microgram quantities needed for most applications. For example, 100 nanograms of antiprotons can be used to catalyze sub-critical nuclear reactions and drive a one metric ton payload to 100 km/sec. This capability would enable the first precursor interstellar missions. In comparison, if traditional chemical propellants were used for the same task, nearly 10^9 metric tons of hydrogen and oxygen would have to be launched into space. To put this in perspective, the space shuttle can carry approximately 20 metric tons to low Earth orbit. If one space shuttle filled with fuel were launched every day, it would take nearly a half million years to lift that much propellant into orbit. The influence of the rocket equation is very pronounced in these scenarios. The traditional propellant required to accelerate a 1 kg payload to 1000 km/sec exceeds the mass of the observable universe by 44 orders of magnitude. In comparison, the same velocity could be achieved with a spacecraft utilizing just micrograms of antiprotons.

The key to enabling such antimatter-fueled missions is the ability to first concentrate and then store antiprotons collected from the natural environment. The proposed collection system adapts a plasma magnet (Slough, 2006) to create a lightweight magnetic scoop, which can influence the trajectory of a charged particle over large spatial scales. This is the basic premise of the Bussard magnetic scoop first proposed for interstellar travel. (Bussard, 1960) However, our concept is to use the system on a spacecraft in an equatorial orbit to direct and then trap radiation belt antiparticles as they bounce between their mirror points in the Northern and Southern hemispheres.

The baseline concept calls for using conventional high temperature superconductors to form two pairs of RF coils that have a radius of 100 m and weigh just 7000 kg combined. A 5000 kg nuclear or solar power system provides the 200 kW required to operate systems and compensate for dissipative losses in the plasma. The magnetic field induced by plasma motion driven by the RF coils is used to first concentrate the incoming antiprotons and then to trap them. Based on the Earth antiproton flux, the system would be capable of collecting 25 nanograms per day and storing up to 110 nanograms of it in the central region between the coils. The system is more than five orders of magnitude more cost effective than Earth based antiproton sources for space-based applications.

UTILITY OF ANTIMATTER

The annihilation of antimatter with its normal matter counterpart liberates the total amount of energy predicted by Einstein's famous equation, $E=mc^2$. As shown in table (1.1), on a mass basis this is about 10^{10} times more efficient than chemical reactions and 10^2 -10^3 times more efficient than nuclear reactions. To put this in perspective, the annihilation of 1 kg of antimatter releases the energy equivalent to 30 million barrels of oil. The total worldwide energy consumption per year corresponds to approximately 2200 kg of antimatter. The extremely high-energy content and other properties of antiparticles enable new applications in both space and on the Earth. In particular, the annihilation of antimatter with its regular matter counterpart enables extremely high-performance space propulsion systems.

Fuel	Energy Density (J/kg)	Notes
Battery	7.2×10^{5}	Lithium Ion
Chemical	1.4×10^{7}	LO_2/LH_2
Fission	8.2×10^{13}	U^{235}
Fusion	3.4×10^{14}	DT
Antimatter	9.0×10^{16}	$E=mc^2$

Table 1.1 – Fuel energy density.

As early as 1953, Eugene Sanger suggested utilizing positrons for spacecraft propulsion. Beamed core antiproton propulsion approaches the theoretical ISP limit of about 30×10^{6} seconds. Compared to the best chemical propulsion (ISP ~400 seconds), antimatter rockets have extremely good mass fractions due to the ISP influence on the rocket equation. Schmidt et al. (1999, 2000) reviewed the performance of several antimatter propulsion methods in the context of aggressive interplanetary and interstellar precursor missions. Antimatter Catalyzed Microfission/Fusion (ACMF) requires only nanogram quantities of antiprotons to achieve spacecraft ΔVs in the range of 100 km/sec. Small-scale thruster experiments with a variant of this technology were previously proposed as part of another NIAC-funded program. (Howe and Jackson, 2004) However, the fundamental challenge common to all of these concepts remains the production and long-term storage of antimatter.

The high ΔV potential enables new classes of aggressive space exploration missions. Less than 10 micrograms of antiprotons are required to send a 100 metric ton payload on a one-year round trip mission to Jupiter. Similar class missions include fast trips beyond the heliopause (100+ AU) and to the Sun's gravity focus point (550 AU) which effectively enables the Sun to be used as a giant telescope with unprecedented resolution. More traditional missions, such as those to Mars envisioned in NASA's current vision for space exploration, are also improved substantially. For example, a traditional low energy Mars trajectory entails an average one way flight time of approximately 180 days while a 30-nanogram antiproton-driven ACMF variant would have a flight time of about 45 days and reduce the overall mass launched into LEO for each mission. (Gaidos, 1998) Table (1.2) summarizes the various forms of antiproton-based propulsion. Positron propulsion concepts also exist though they are generally limited to the heated core variety (Smith, 2005) since positron annihilation does not directly induce secondary nuclear reactions.

Antiproton Propulsion Concepts

Class	***ΔV Limit***	***Antimatter Use (1mT payload at max ΔV)***	***Notes***	***References***
Beamed Core	1×10^{5} km/sec	2000 kg	The charged products created from proton/anti-proton annihilations are directed via a magnetic nozzle to produce thrust. This is the most straightforward technique with the highest potential velocity (~0.33c) though antiproton requirements are well beyond quantities obtainable with any known technique.	Forward, 1985 Howe and Metzger, 1989 Frisbee and Leifer, 1998
Heated Core	2×10^{3} km/sec	300 g	Antiproton annihilation products directly heat a working material through which propellant flows before being ejected through a nozzle to produce thrust. Solid, gas, and plasma cores can be used with a plasma core offering the highest performance.	Howe and Metzger, 1989 Cassenti, 1991 Frisbee and Leifer, 1998
AIM	1×10^{3} km/sec	300 μg	Antimatter-Initiated Micro-fusion (AIM) uses electric and magnetic fields to repetitively compress an antiproton plasma, which is then used to ignite D-T or D-He3 fusion aided by a fissile seed. The combined products are then directed out of a magnetic nozzle to generate thrust. This is considerably more complicated than the heated core concept but antiproton requirements are reduced significantly since a large fraction of the propulsive energy is provided by the fission and fusion reactions.	Gaidos et al., 1998 (1)
Catalyzed Nuclear Cascades	100 km/sec	100 ng	Antiprotons are used to induce sub-critical nuclear reactions. The annihilation of the antiproton with one of the target nuclei induces a fission reaction. This energy can be used directly or serve to cascade further reactions and generate thrust. In the antimatter sail concept, a stream of low-energy antiprotons is used to induce reactions in a thin foil layer of uranium. The nuclear debris from this reaction is then redirected to generate thrust.	Gaidos et al., 1998 (2) Jackson, 2006

Table 1.2 – Summary of antiproton propulsion concepts.

New non-space applications have also been proposed. One of the most promising concepts is to use antiprotons to image the interior of solids. Material properties and their distribution in the solid can be determined by examining the annihilation products. (Forward and Davis, 1988) This has profound implications in both medical diagnostics and homeland security. Also in the medical area, picogram quantities of antiprotons can be used to locally treat inoperable tumors. (Gray and Kalogeropoulos, 1982) Finally, from a pure science perspective, improving the availability of antimatter will allow new experiments to be performed to confirm theoretical predictions in atomic and gravitational physics.

CURRENT PRODUCTION AND STORAGE CAPABILITIES

Currently, the primary source of controlled antiprotons is from high-energy particle accelerators. Both CERN in Switzerland and the Fermi National Accelerator Laboratory (FNAL) produce antiprotons during the collision of high-energy proton beams with a solid target. Resulting reactions produce copious numbers of various particles through pair production and other nuclear events. A small percentage of the ejecta can be magnetically confined and focused to separate out the antiprotons, which are then decelerated and placed in a confinement ring for use in subsequent experiments.

At FNAL, approximately 10^7 antiprotons per pulse can be 'stacked' in the accumulator ring. Presently, 10^{11} antiprotons per hour can be produced for 4500 hours per year. (Schmidt et al., 1999) If the facility were used to exclusively create and accumulate antiprotons, a total of almost one nanogram (1 ng) would be produced over the course of a year. A number of improvements have been discussed which could enhance this by a factor of 10 or more by increasing the efficiency of the collection process. It has been suggested that a dedicated facility could be built for $5-$17 billion, which could increase production still further. (Augenstein, 1988)

Schmidt et al. discuss some of the fundamental energy cost constraints of producing antiprotons in particle accelerators. Currently, only one in about 10^5 proton collisions produces an antiproton that can be collected. Due to the energy requirements for accelerating the proton beam, even with a wall plug efficiency of 50%, $0.10 per kilowatt-hour yields a net antiproton production cost of $62.5 trillion per gram collected due to electricity costs alone. In another analysis, LaPointe (2001) estimated the current electricity costs to be $160 trillion per gram.

A number of alternative production techniques have been proposed. Hora (1973) and Crowe (1983) have suggested using high intensity lasers to produce antimatter. However, efficiently generating laser pulses with sufficient energy remains an obstacle. Chapline (1982) proposed using heavy ions instead of proton beams to increase accelerator production, though the antiprotons are still generated isotropically making it difficult to collect the antiprotons from the ejecta debris. Cassenti (1993) has suggested redirecting pions generated during collisions, though this approach also suffers from the difficulty of containing and redirecting the debris. These variations all have similar energy cost limitations.

LaPointe (2001) proposed using the Casimir force to suppress local vacuum fields as a means to generate the steep gradients required for antiproton production at a potential boundary. The concept calls for holding two conducting metal plates nearly a meter on a side to within 1 nanometer of each other. This approach, too, has yet to be demonstrated in practice and remains outside the realm of manufacturability, at least in the near term. However, the basic physics of production can be validated with positrons, which the author suggests could be accomplished with half-meter plates placed about 100 nanometers apart. Though this would be challenging, the production of positrons would validate the relevant physics.

After production in Earth-based facilities, antiparticles must be stored in a high-vacuum environment and suspended in magnetic/electric/RF fields to avoid losses due to annihilation with air nuclei and the container walls. Howe and Smith (1998) reviewed antiproton storage concepts in a previous NIAC phase I program. The long-term storage of antiprotons is limited by storage density and the hardness of the vacuum since introduced particles will annihilate with antiprotons in the trap. Currently, the most advanced portable trap (HiPAT) can, in principle, store approximately 10^{12} antiprotons (~1 picogram) for days or more at a time by maintaining the trap at a temperature of 4 Kelvin. The storage density can be increased by forming electrically neutral anti-hydrogen atoms to address space charge and Brillouin trapping limits though this has not been demonstrated at a relevant scale. A variety of other condensed-matter concepts have been discussed including leveraging photonic band-gap structures, quantum reflection, parelectricity and other techniques to improve antiproton trapping. Related to this, it has been postulated that extended storage of positrons can be accomplished by preventing excited positronium from decaying to its ground state. (Barker, 2004) Edwards (2004) reported on efforts at Positronic Research LLC to store positrons in quantum dots by using the Lorentz force to maintain a separation between the electron and positron in positronium. He presented data showing that the lifetime before annihilation could be extended to almost 300 nanoseconds. No other publically available data is available to suggest that it is possible to maintain stable positronium for periods extending beyond this.

The first trap capable of transporting 10^{10} antiprotons (~10 femtograms) was 100 cm tall by 30 cm across and weighed 55 kg fully loaded. (Holzscheiter, 1997) The system mass to antiproton mass is therefore 10^9 kg/μg though it is unclear how, or even if, this can scale to the nanogram to microgram class storage levels needed for space applications. The particles would need to be produced and then stored over a period of months to years without significant annihilation losses. The ability to transport antiprotons (in their traps) generated on the ground into orbit remains a serious obstacle even if ground-based production can be scaled to much higher rates.

IN SITU PRODUCTION AND TRANSPORT

In comparison to artificial production, natural sources of antimatter are plentiful and relatively easy to exploit for benefit. A natural antiproton radiation belt is generated in a manner analogous to the traditional Van Allen radiation belts, which surround the Earth. The high-energy portion (E>30 MeV) of the proton belt is primarily formed by the decay of neutrons in the Earth's magnetosphere. The GCR flux interacts with the planet's upper atmosphere to release free neutrons with a half-life of just over 10 minutes. A fraction of these neutrons travel back into space (albedo) and decay into a proton, electron, and an anti-neutrino while still within the influence of the magnetosphere.

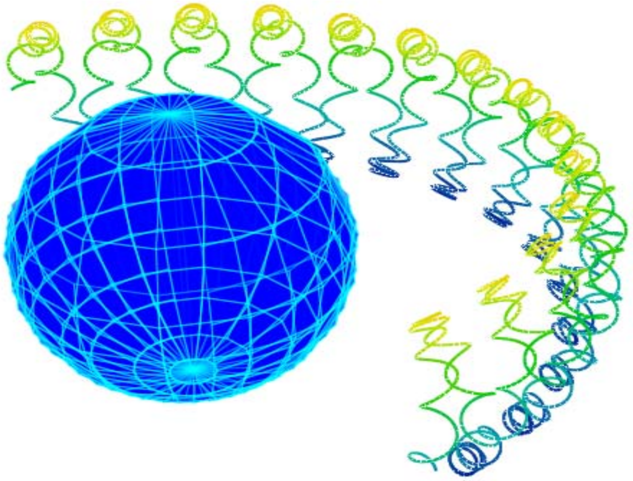

Figure 1.2 – Motion of a charged particle trapped in a planet's magnetosphere.

The magnetic field of the planet forms a bottle to stably hold the protons and electrons from the decay process. If the trajectory of the ejected proton from the decay process is outside of the planet's loss cone for magnetic confinement, the proton will be trapped on the magnetic field line (L-shell) on which it was formed. The periodic motion (figure 1.2) is explained by the Lorentz force, which causes the particles to spiral along the magnetic field lines and mirror between the

Northern and Southern hemispheres. In addition, the particles have a slow drift motion around the planet. As particles are lost through diffusion and loss processes, new ones are generated to maintain a quasi-static supply trapped in the magnetic field of the planet.

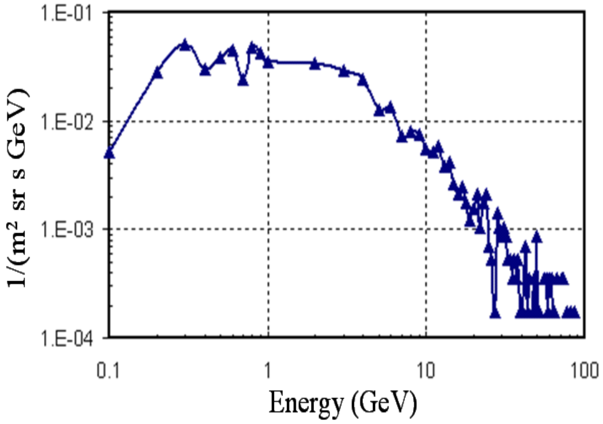

Figure 1.3 – Production spectrum for antineutrons generated in the Earth's atmosphere.

The interaction of cosmic radiation with the upper atmosphere also produces antiparticles from pair production. Figure (1.3) shows computer simulations of the nuclear transport phenomena that generate antineutrons from the incident particle flux. The produced antineutrons follow a trajectory primarily along the path of the original cosmic ray, but can be backscattered after interacting with the atmosphere. These albedo antineutrons decay in a manner similar to the regular neutrons. However, the antineutron will decay into a positron, antiproton, and neutrino and therefore acts as a source for the antiparticle radiation belts surrounding the Earth. The physics that govern the trapping and motion are identical between the particle and its antiparticle with the exception that the two will spiral and drift in opposing directions due to their opposing electric charges.

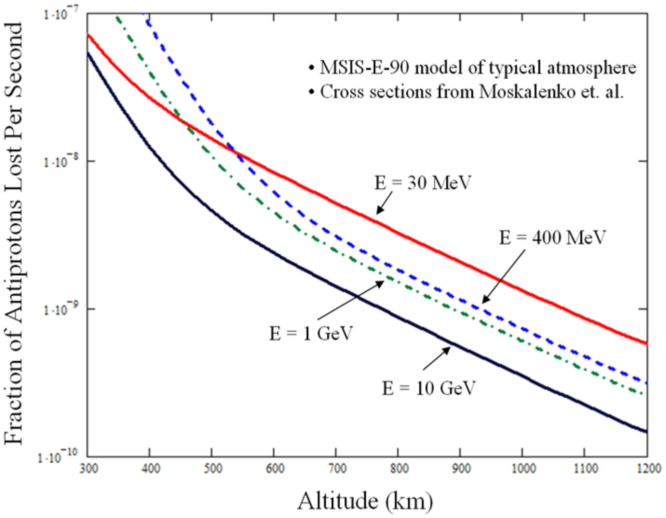

Figure 1.4 – Fraction of antiprotons lost per second due to annihilation with the atmosphere. (Earth)

The residual atmosphere of Earth extends thousands of kilometers from the planet. The trapped antiprotons can annihilate with these atmospheric constituents, especially at low altitudes where this becomes the primary loss mechanism. Figure (1.4) shows the estimated loss rates for particles at several energies as a function of its altitude. At typical radiation belt altitudes, this loss rate is extremely low enabling a large supply of antiprotons to form.

NATURAL SOURCES OF ANTIPROTONS

The production of antiparticles can occur at any location where there is sufficient energy to induce pair production. Under natural conditions in our solar system, only galactic cosmic rays (GCR) are energetic enough to produce proton/antiproton pairs. However, virtually all bodies in our solar system interact in this way and generate antiparticles via these reactions. Figure (1.5) shows the resulting flux of antiprotons, which are stored in the radiation belts surrounding the Earth.

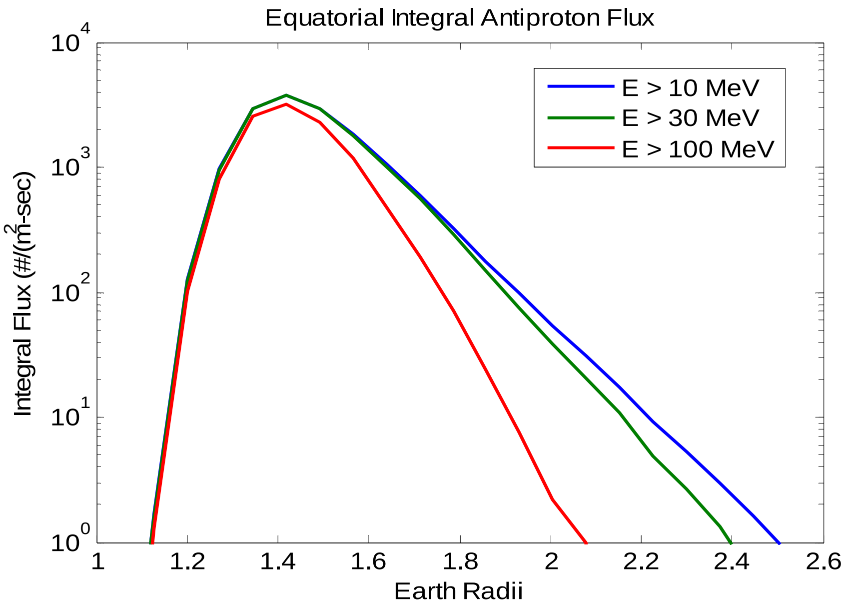

Figure 1.5 – Antiproton flux in the Earth's magnetic field.

All major objects in our solar system were evaluated for their ability to generate antiprotons. The values vary from one location to another due to the relative strength of the transport and production mechanisms around each body. The relative density, diffusion rates, and local field strength all play major roles. For example, figure (1.6) shows the integral flux around the planet Saturn where the influence of its unique ring and Moon structure can clearly be seen. Table (1.3) summarizes the results, which are detailed in subsequent chapters. The table includes all the planets with magnetic fields sufficient to support radiation belts. In addition, solar system bodies which may support larger transient fluxes were also evaluated.

Natural Antiproton Fluxes

Source	*Peak Flux*	*Trapped Supply*	*Fill Rate*	*Notes*	*Detail*
 Galactic Cosmic Rays (GCR)	3 m^{-2}s^{-1}	N/A	N/A	Antiprotons are generated when the GCR flux interacts with the 5-7 gm/cm^2 of material that it encounters as it travels through the interstellar medium. This creates a pervasive flux that has been well characterized by balloon and space based measurements. About 1 kg/sec enters the solar system but only a few grams reach the Earth's magnetosphere each year. The influence of the Earth's magnetic field may locally increase the flux levels by a factor of 5 near the magnetic poles.	Chapter 4

Source	***Peak Flux***	***Trapped Supply***	***Fill Rate †***	***Notes***	***Detail***
 Earth's Magnetosphere	4000 $m^{-2}s^{-1}$	160 ng	2 ng/yr	Albedo antineutrons generated from GCR interactions with the atmosphere decay to produce antiprotons, which can be trapped by the planet's magnetic field. Their diffuse nature enables an antiproton belt analogous to the protons in the Van Allen radiation belt to form.	Chapter 2
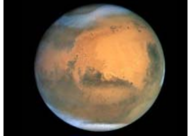 Mars' Surface	30 $m^{-2}s^{-1}$	N/A	N/A	The GCR proton flux passing through the average atmospheric thickness of 65 gm/cm^2 will generate the maximum antiproton flux near the surface. The magnitude is roughly equivalent to 10 times the GCR antiproton background flux.	Chapter 4
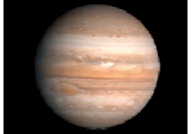 Jupiter's Magnetosphere	10 $m^{-2}s^{-1}$	6 μg	7 μg/yr	Antiprotons are primarily formed from the interaction of the GCR flux with the atmosphere of Jupiter to produce antineutrons via pair production. A portion of the antineutron flux decays into antiprotons, which are then trapped in the planet's magnetic field. The strong magnetic field of the planet assists in the trapping of the particles but also shields the atmosphere from much of the GCR source flux.	Chapter 3
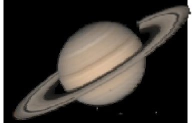 Saturn's Magnetosphere	70 $m^{-2}s^{-1}$	10 μg	240 μg/yr	Saturn is similar to Jupiter but the source strength is increased substantially due to the rings surrounding the planet. The belt is far more efficient at generating antineutrons, which can decay in the trapping region of the planet since the generated particles do not have to go through a secondary scattering reaction like the atmospheric albedo source.	Chapter 3
 Uranus' Magnetosphere	320 $m^{-2}s^{-1}$	1.4 μg	0.9 μg/yr	Primarily formed from the interaction of the GCR flux with the planetary atmosphere to produce antineutrons via pair production. A portion of the antineutron flux decays into antiprotons, which are then trapped in the planet's magnetic field.	Chapter 3
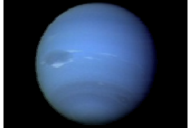 Neptune's Magnetosphere	600 $m^{-2}s^{-1}$	2 μg	0.9 μg/yr	Primarily formed from the interaction of the GCR flux with the planetary atmosphere to produce antineutrons via pair production. A portion of the antineutron flux decays into antiprotons, which are then trapped in the planet's magnetic field.	Chapter 3
 Sun	$<0.02\ m^{-2}s^{-1}$	N/A	N/A	GCR interactions with the solar atmosphere produce albedo antineutrons via pair production, which escape and decay into antiprotons. Nearly 6 g/yr is produced by the Sun though the flux is less than $10^{-6}\ m^{-2}s^{-1}$ at 1 A.U. Approximately 100 ng/yr will impinge of the Earth's magnetosphere though only a small fraction ($\sim 10^{-3}$) will be trapped for any length of time.	Chapter 4
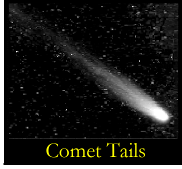 Comet Tails	$< 10^{-6}\ m^{-2}s^{-1}$	N/A	N/A	The GCR flux interacts with comet material to generate antiprotons through pair production. Only very small fluxes are produced due to the low density of the tail.	Chapter 4

Table 1.3 – Summary of natural antiproton sources in our solar system.

---

† Replenishment rate from natural sources.

Surprisingly, Jupiter is not the best source of antiprotons in the solar system. Even though it is the largest in terms of size and field strength, the magnitude of the magnetic field shields much of the atmosphere from the GCR production spectrum, which reduces the overall effectiveness of the process. In comparison, a larger fraction of the flux reaches the atmosphere of Saturn. In addition, the antineutrons that are copiously produced in the rings do not have to be backscattered to yield stable trapping. However, the highest flux is actually found around Earth where the relatively slow radial transport in the magnetosphere produces long residence times, which allow the antiproton trap to fill over a period of years.

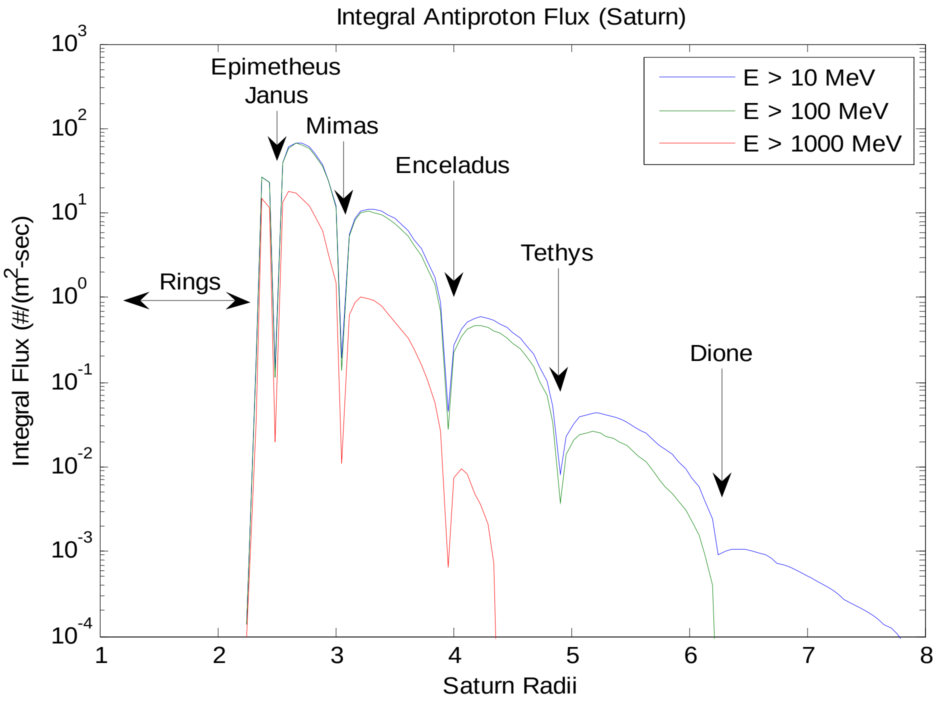

Figure 1.6 – Antiproton flux in Saturn's magnetic field.

ANTIPROTON COLLECTORS

In the phase I program we evaluated the efficiency and collection rate of a single coil magnetic scoop designed to extract large quantities of trapped antiparticles from the natural space environment. The magnetic scoop was formed from superconducting wires to generate a dipole field for modifying the trajectory of incident particles. The system was evaluated for its ability to extract antiprotons from an ambient flux efficiently. It was found that the required system size to collect a microgram of antiprotons from the cosmic ray background would be mass-prohibitive without improvements in superconducting technology.

During the phase II effort, our analysis was expanded to look for alternatives that would yield better performance so systems could be built without fundamental advances in superconducting technology. Table (1.4) summarizes the relative performance of the various concepts considered. Collection rates are based on the Earth flux unless stated otherwise and costs are based on the cost to launch the relevant systems or material into low Earth orbit. It was found that a plasma magnet is orders of magnitude more mass efficient than the single coil loops originally analyzed. This can be compared to other options for antiproton generation, which are shown in table (1.5). Plasma magnet systems are more than four orders of magnitude more cost effective than Earth based production for space propulsion. Orbital antimatter factories offer better theoretical performance though they require fundamental advances, which are highly uncertain. Chapter (4) discusses space based antimatter platforms and chapters (6) and (7) provide a detailed description of collector concepts.

Charged Particle Collection Systems

Type	*Coil Rad*	*Sys Mass*	*Sys Power*	*Collection Rate*	*Perf Metric*	*Pbar Cost*	*Notes*
 Single Coil	100 km	10^{10} kg + power system (10^{9} kg)	10 GW	0.05-0.1 ng/yr	10^{-11} ng/yr/kg_{sys}	~10^{15} \$/ng/yr	A large-scale magnetic field is generated with superconducting coils to form an antiproton 'funnel' and particle trap. Large collectors operating at very high currents are required for significant focusing, but steep gradients near high-field regions place an upper limit on performance. A significant improvement in superconductor technology is needed for concept viability.
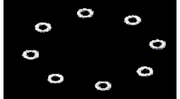 N Coils	10 km	10^{10} kg + power system (10^{10} kg)	100 GW	0.1~0.25 ng/yr	10^{-11} ng/yr/kg_{sys}	~10^{15} \$/ng/yr	The use of multiple collectors in formation allows for a favorable increase in performance by exploiting the symmetry of the incident particle flux. Performance is roughly one half order of magnitude improved though formation control may be a significant obstacle.
 Concentric Coils	100 km	10^{10} kg + power system (10^{9} kg)	10 GW	4-10 ng/yr	10^{-9} ng/yr/kg_{sys}	~10^{13} \$/ng/yr	The limiting case of N-coil collection systems, with an effectively infinite N. The reduction in power system mass due to only two coils dramatically improves cost-effectivenes. However, the system is dynamically unstable which limits practicality.
 Step Ladder	100 km	10^{4} kg	N/A	10^{-2} ng/yr	10^{-12} ng/yr/kg_{sys}	~10^{10} \$/ng/yr	A staggered series of wire coils placed close to a Debye length away are used to electrostatically focus incident antiprotons. Debye shielding and the natural repulsion of the charged coils limit the viability of this concept.
 Jackson Sphere	16 km	10^{9} kg + power system (10^{8} kg)	10 GW	1 ng/yr	10^{-9} ng/yr/kg_{sys}	~10^{11} \$/ng/yr	Concentric wire spheres (Jackson, 2006) collect GCR antiprotons via electrostatic interactions. The mass estimate is driven by the positron/electron mix used to cool the antiproton beam as it passes through the system. Power requirements are based on the need to generate a 1GV voltage.
 Electrostatic Sphere w/ RF	16 km	10^{4} kg + power system (10^{8} kg)	20 GW (?)	1 ng/yr	10^{-9} ng/yr/kg_{sys}	~10^{10} \$/ng/yr	Here we propose replacing Jackson's positron/ electron mix with RF energy to cool incident antiprotons via plasma wave interactions. This removes the most serious difficulty with the Jackson sphere (the need for 10^{9} kg of positrons) though the power system mass is still significant. Operation in the Earth's radiation belt could improve performance since the flux is 10^{3} higher and the antiproton energy is 10 times lower.
 Plasma Magnet	100 m	~$5\text{x}10^{4}$ kg + power system (~$5\text{x}10^{4}$ kg)	~200 kW	~8.6 μg/yr	~0.73 ng/yr/kg_{sys}	~10^{4} \$/ng/yr	The superconductor used in the single coil system is replaced with a plasma magnet to reduce system mass. The relatively shallow field gradients allow for highly efficient focusing, while the use of a hot, sparse plasma mitigates the cost of maintaining an intense magnetic field. The inclusion of a non-neutral species as a supplemental focusing mechanism could possibly improve performance at minimal cost.

Table 1.4 – Summary of antiproton collection concepts.

Artificial Antiproton Generation

Type	Size	Space Power	Collection Rate	System Mass	Pbar Cost	Notes
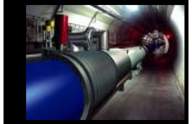 Earth Based	8 km (e.g.)	N/A	1-10 ng/yr	10^7 kg‡	~10^5 \$/ng (Earth) ~10^9 \$/ng (space)	This assumes that the worldwide production of antiprotons from particle accelerators would be diverted to space propulsion needs instead of science. The mass of the trapping system is the largest driver in system cost due to the need to launch each trap into orbit. This will remain the dominant constraint until a fundamentally new approach is developed for antiproton storage.
 Space Based (Haloulakos & Ayotte, 1991)	200+ m	54 GWe	1 g/wk	10^8 kg	~100 \$/ng/yr	Hypothetical space based antimatter factory assuming a five order of magnitude improvement in production efficiency. One major obstacle is the need for nearly 50 GWe of power in orbit, which is the equivalent of nearly 50 large Earth based power plants. The advantage of the system is that the antiprotons do not have to be transported to orbit.
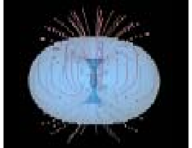 Space Based (Bickford, 2006)	200 m	300 kWe	9.5 μg/yr	>10^4 kg	~10^4 \$/ng/yr	Space based variant which improves production efficiency by placing the antiproton production target within the effective volume of the antiproton trap. The high vacuum space environment enables the antiprotons to be stored in a diffuse plasma surrounding the space platform.

Table 1.5 – Summary of artificial antiproton generation capabilities.

SYSTEM CONCEPT

The baseline concept of operations calls for a magnetic scoop to be placed in a low-inclination orbit, which cuts through the heart of the inner radiation belt where most antiprotons are trapped. Placing the vehicle in an orbit with an apogee of 3500 km and a perigee of 1500 km will enable it to intersect nearly the entire flux of the Earth's antiproton belt. The baseline mission calls for a fraction of the total supply to be trapped over a period of days to weeks and then used to propel the vehicle to Saturn or other solar system body where there is a more plentiful supply. The vehicle then fully fills its antiproton trap and propels itself on a mission outside of our solar system. Future enhanced systems would be able to collect from the GCR flux en route to further supplement the fuel supply. Alternatively, another mission concept calls for a fast crewed transit to Mars by transferring collected antiprotons from a fuel depot to a smaller vehicle capable of supporting the crew on an accelerated mission to the red planet.

Table (1.6) shows the performance parameters of a system based on a plasma magnet. A large-scale magnetic field is generated by an orthogonal rotating magnetic field, which induces the motion of electrons in the plasma. The resulting field, superimposed over existing natural fields, influences the trajectory of charged particles in the spacecraft's vicinity. The particles follow the field lines where they are concentrated as they approach the 'throat' of the collection system. Annihilation losses are negligible as the antiprotons pass through the plasma due to the relatively low density and cross section. RF and/or electrostatic methods are then used to degrade the particle momentum as it approaches the throat so it can be trapped in the inner coil region. Long term trapping without the

---

‡ This is the mass of the storage traps only and does not include the accelerator mass.

risk of major annihilation losses is possible since the region between the coils is relatively devoid of protons.

Once in the trapping region near the spacecraft, the antiprotons stored in the field can be directed to react with material near the throat to catalyze a nuclear reaction, producing ejecta which can be used to propel the vehicle with high efficiency. The magnetic field gradient is used to direct the trajectory of the ejecta and therefore acts as a magnetic nozzle. Finally, this same field acts as a radiation shield to partially protect equipment (and possibly astronauts) within the center region. Therefore, the magnetic field acts as a multi-functional device, providing:

- An antiparticle collection system
- Stable antiparticle fuel storage
- A nozzle and propulsion system
- Radiation shielding

Table (1.6) shows the performance of the baseline collection system. The antenna mass, power system, and launch costs are shown for currently available technology as well as for hypothetical advances which may occur in the next 20-30 years. Even with current technology, the system is very competitive with other propulsion options and offers the potential for mission profiles that are not feasible with any other demonstrated technology. In addition, the design has not been fully optimized and significantly better performance is possible.

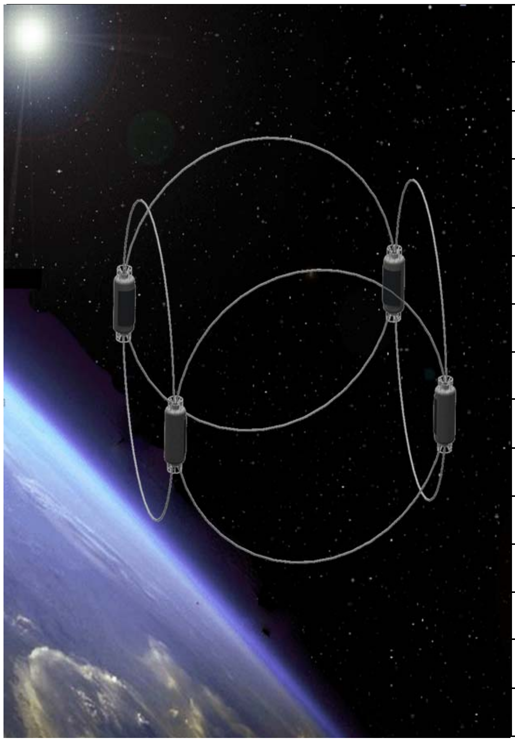

Parameter	***Current Tech***	***Future Tech***
Antenna Loop Radius	100 m	100 m
Operating Current	10^5 A	10^5 A
Plasma Density	$2 \cdot 10^{16}$ m^{-3}	$2 \cdot 10^{16}$ m^{-3}
Plasma Temperature	15 eV	15 eV
Antenna Mass	6650 kg	< 1000 kg
Power	200 kW	200 kW
Power System Mass	5200 kg	< 1000 kg
Total Mass	12,000 kg	2000 kg
Collection Rate	25 ng/day	25 ng/day
Storage Density	8.4 x 10^9 m^{-3}	8.4 x 10^9 m^{-3}
Storage Capacity	110 ng	110 ng
Launch Cost	$100M	$10M
Mass Metric	2.0 ng/day/mt$_{sys}$	1.2 ng/day/mt$_{sys}$
Cost Metric§	$900k/ng	$90k/ng

Table 1.6– Baseline antiproton collection system for current and projected superconductor and power technology.

---

§ The cost metric is based on the one-time use of a device filled to capacity. The specific cost is reduced if the trap is re-filled and/or the system is reused since the launch represents a single non-recurring cost.

GOVERNING EQUATION AND DIFFUSIVE TRANSPORT

Two fundamentally different sources of protons are at work to populate the Van Allen radiation belt. The first is Cosmic Ray Albedo Neutron Decay (CRAND), which is the primary source function for the high-energy population. The second is the diffusion of protons from an external source, namely the Sun. This external diffusion process primarily serves to populate the low energy portion of the belts, especially at higher L shells. There is no equivalent external source for the antiproton population since the Sun is not energetic enough to generate antiprotons through pair production on its own. However, cosmic rays interacting with the atmosphere are energetic enough to produce an antiproton source that is exactly analogous to the CRAND source.

The nature of the CRAND process is shown in figure (2.1) and reviewed by Ifedili (1991). The generation of radiation belt protons is driven by high-energy cosmic rays, which induce nuclear reactions in atmospheric nuclei. Many particles are generated, some of which are free neutrons following trajectories which leave the atmosphere. The majority of these albedo neutrons are formed below 10 MeV due to the physics of the spallation process.

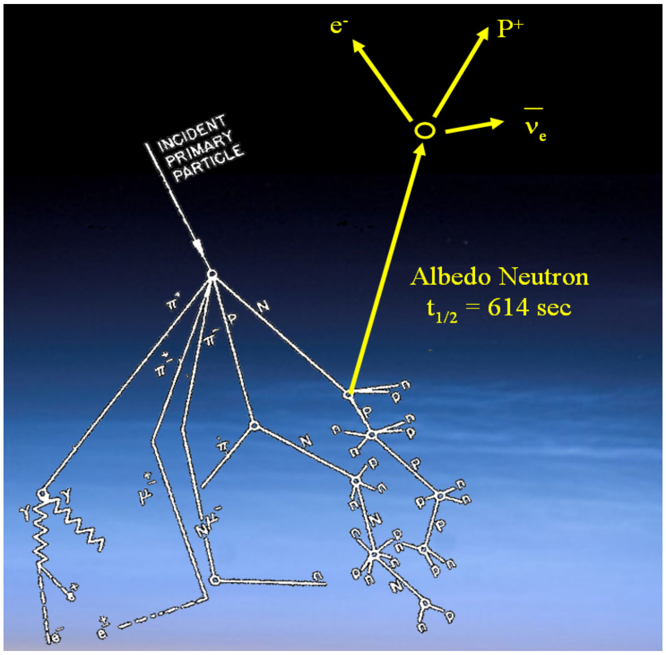

Figure 2.1 – Cosmic Ray Albedo Neutron Decay (CRAND)

Neutrons are stable when bound in nuclei but decay into an electron, proton, and anti-neutrino in their free state with a half-life of just over 10 minutes. Although the majority of neutrons will be absorbed by the atmosphere or pass outside the influence of the Earth before decaying, a small fraction of the particles will decay while inside the magnetosphere. If the ejected proton is properly oriented, with a velocity vector outside the loss cone for a particle at that energy and location, it will be stably trapped within the radiation belt. The decay of albedo neutrons thus acts as a source to populate the proton belt. The generation of antineutrons from pair production in the atmosphere leads to an equivalent source for the antiproton radiation belt.

The evolution of trapped particles in phase space (*f*), is described by the equation,

$$\frac{\partial f}{dt} = L^2 \frac{\partial}{\partial L}\left[\frac{D_{LL}}{L^2}\frac{\partial f}{\partial L}\right] + Sources + Losses \tag{2.1}$$

where D_{LL} describes the radial diffusion rate across L-shells due to magnetic and electric fluctuations in the global field (Schulz and Lanzerotti, 1974). Here we have ignored pitch angle diffusion since this is a minor effect (Selesnick, 2007) for antiprotons due to their relatively large mass compared to an electron. After the appropriate physics for the source and loss terms are modeled, the elliptic partial differential equation can be solved to estimate the quasi-static spatial distribution of charged particles trapped in a planetary magnetosphere.

Diffusive radial transport is due to a number of combined effects, which arise when the third adiabatic invariant of the trapped particle is violated. Forces derived from electromagnetic or other sources acting on the particle over a time span shorter than its drift period will transport the particle across magnetic L shells. A model proposed by Jentsch (1981) was used to estimate proton diffusion rates in the Earth's magnetosphere due to the combined effects. The average diffusion coefficient,

$$D_{LL} = 3.75\times 10^{-12} L^9 \sin^{2.7}\alpha_0 \left(\frac{1MeV}{E}\right)\sec^{-1} \tag{2.2}$$

was derived from empirical measurements of the Earth's radiation belts. The L shell dependence is consistent with theoretical estimates for diffusion caused by magnetic and electric field perturbations, which are the result of the planet's magnetic field interacting with the solar wind. As particles are diffusively transported across field lines, they will either gain or lose energy due to the conservation of the first adiabatic invariant. Conveniently, this can be modeled by using the magnetic moment of the particle instead of energy as one dimension in the phase-space density solution.

TRAP STABILITY LIMITS

Long-term stable trapping relies on consistently conserving the adiabatic invariants. Hudson et al. (1998) describes particle stability limits in the Earth's magnetosphere as it reacts to dynamic changes introduced by field fluctuations. A more formal treatment of the trap stability limit due to field gradients is presented by Northrop (1963), Schulz (1991), and Chirikov (1987). The Alfvén criterion describes the limit of stable trapping based on the conservation of the first adiabatic invariant. Particles with energy that place it above this limit are quickly lost from the magnetosphere. The criteria requires that the particle rigidity ($\mathfrak{R}$) and magnetic field gradients characteristics satisfy,

$$\rho = \frac{|\nabla B|}{B} = \mathfrak{R}\frac{|\nabla B|}{B^2} = n \ll 1 \tag{2.3}$$

where n is taken to be ~0.05 based on experimental results. (Hovestadt, 1978)

Violating one of the adiabatic invariants leads to instabilities and chaotic motion. In particular, if the radius of gyration is very large relative to the scale of the field, the magnetic field seen by the particle is not constant through its periodic gyration motion and the first invariant is violated. This eventually allows the particle to escape and effectively limits what could be considered stably trapped. The trapped particles can be considered to be trapped forever until the gyration radius begins to approach the radius of curvature for the field line about which it is gyrating (Pugacheva, 2003). The radius of curvature is functionally dependent upon the latitude but remains constant when normalized by L shell. In the trapping region, the minimum radius of curvature occurs at the equator with a value equal to L/3 in a dipole field.

Pugacheva's criteria for long-term stability is related to the Alfvén criterion but expressed as a function of field parameters in a planetary magnetosphere. It assumes that the gyration radius must be less than 10% of the radius of curvature for the field line on which it resides. Based on this, stable trapping occurs when,

$$L < \frac{30p}{Bq} \tag{2.4}$$

which is only an approximation based on observation but matches empirical data for the Earth's magnetosphere fairly well. Based on this approximation, figure (2.2) shows the estimated values for the Earth, Jupiter, and several traps formed from current loops.

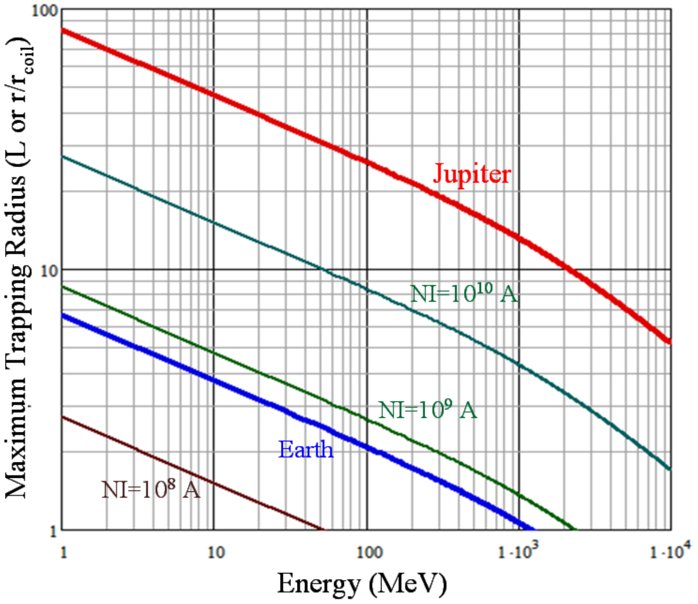

Figure 2.2 – Maximum trapping region for antiprotons.

ANTIPROTON SOURCE TERMS

PAIR PRODUCTION IN THE ATMOSPHERE

The galactic cosmic ray flux impinging on the atmosphere is energetic enough to generate particles through pair production. For source calculations, we adopted the simplified form of the standard ISO standard GCR spectra suggested by Selesnick (2007). The parametric spectra,

$$\frac{dN}{dE_p} = \frac{A_i C_i \beta^{\alpha_i - 1}}{Z_i} \left(\frac{1GV}{\Re}\right)^{\gamma_i} \left(\frac{\Re}{\Re + \Re_0}\right)^{5.5} \frac{1}{m^2 \cdot sr \cdot s \cdot GeV} \tag{2.5}$$

was calculated for nominal solar conditions by setting the solar radio flux value F10.7 to 140. The modulating effect of solar activity is minimal for the high-energy portion of the spectrum that is responsible for the majority of the antiproton production. However, for consistency and for proton belt calculations, the solar conditions were averaged to represent the mean cycle likely to influence radiation belt evolution. To simplify calculations, the nuclear transport Monte Carlo calculations were based on the dominant Hydrogen portion of the spectrum and multiplied by the heavy nuclei correction factor suggested by Sina (2001).

The magnetic field of the planet will modify the spectrum by partially shielding the atmosphere from the incoming flux. The vertical cutoff rigidity ($\Re_{cv}$) is given by Selesnick et al. as,

$$\Re_{cv} = \frac{\mu_p \cdot c \cdot \cos^4(\lambda)}{4r^2} \tag{2.6}$$

for a simple dipole field where μ_p is the magnetic moment of the global field, λ us the latitude, and r is the radius of the point being evaluated. Overall, the cutoff does not significantly reduce antimatter production around Earth since pair production primarily is driven by the source spectrum above 20 GeV while the cutoff for a proton approaching the equator is less than 14 GeV. Particles below the vertical cutoff and with large initial pitch angles can also be shielded resulting in a bias in the angular distribution of the particles. However, this also does not play a play a significant role since antineutron production that subsequently leads to trapped antiproton fluxes are biased towards particles that approach the atmosphere at a shallow angle.

The atmosphere which the GCR flux impinges upon was based on the MSISE-90 model (Hedin, 1987), which was approximated as multiple atmospheric layers modeled as concentric shells. Each layer in the model contained the average number density of Hydrogen, Helium, Oxygen, Nitrogen, N_2, O_2 and Argon. The model was used to predict nuclear reactions due to collisions between the neutral atmosphere and the source flux. Ionized particles given by the IRI-2001 model (Bilitza, 2001) do not play a significant role in pair production due to their low number density at the relevant altitudes.

The interaction of the GCR flux with the neutral atmosphere was calculated with the Geant4 Monte Carlo simulation package (version 4.6.2). Geant4 is a toolkit for the simulation for the passage of particles through matter, and has been validated extensively for modeling these effects (Agostinelli, 2003). Geant4 was used to predict the flux of antineutrons generated in the atmosphere of the Earth by impinging the GCR proton spectrum on a model of the atmosphere. The antineutron spectrum shown in figure (1.3) is substantial but, unfortunately, the particles are mostly produced within a tight angular cone centered on the original path of the impinging cosmic ray. Therefore, as shown in figure (2.3) the majority of the antineutrons produced lie within a narrow 10-degree cone on a downward trajectory away from the magnetosphere.

Pugacheva (2003) estimated the efficiency of albedo antineutron production at about 1 part in 10^9 relative to neutron production at an energy of 100 MeV. However, antineutrons may also go through a second scattering process within the atmosphere, which can reduce their energy and increase the relative contribution of albedo antineutrons leaving the atmosphere. In addition, particles generated by the GCR flux, which approach the atmosphere at a shallow angle, are very likely to exit the atmosphere. These combined effects can increase the relative efficiency of albedo antineutron production by up to five orders of magnitude. As we will show below, the relative ratio of albedo antineutron production increases to 1 part in 10^4 for particles with energy near a few hundred MeV and trajectories near the horizon.

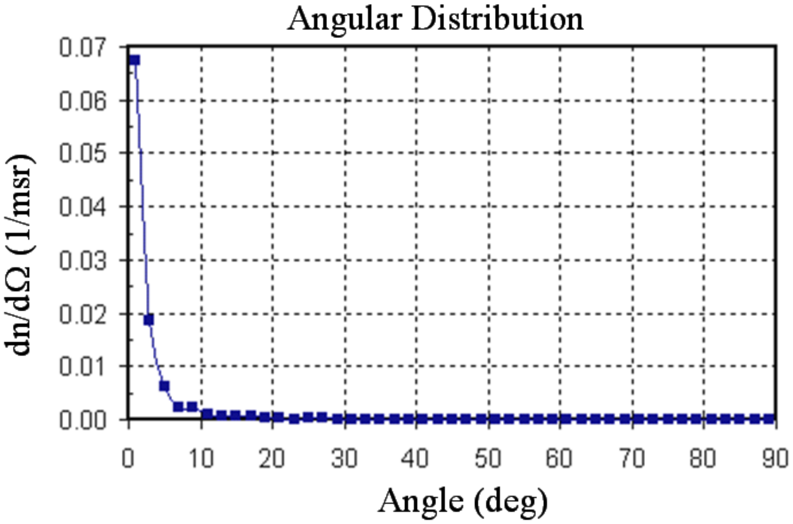

Figure 2.3 – Angular distribution of pair produced antineutrons.

An extensive set of Monte Carlo calculations were performed in Geant using the incident GCR spectrum as an input. For each case, the albedo antineutron flux was estimated by transporting a total of more than 10^6 particles through the Earth's atmosphere. An equation was parametrically fit to the results to define the antiparticle flux as a function of the albedo angle (θ) relative to the local zenith and the albedo particle energy (E). The approximate albedo antineutron flux is,

$$j_{\bar{n}} = \delta \cdot k_1 \cdot \frac{E}{MeV} \cdot e^{k_2 \cdot \frac{E}{MeV} \cdot \frac{\theta}{\deg}} \frac{1}{m^2 \cdot s \cdot sr \cdot MeV} \text{ for E< 500 MeV and } \theta < 90 \text{ deg.} \tag{2.7}$$

where

$$k_1 = 10^{-6}\left(0.1275 - 0.1280 e^{-97689 \cdot \left(\frac{E}{MeV}\right)^{-2.7519}}\right) \tag{2.8}$$

$$k_2 = 0.1173 - 0.1073 e^{-0.0035755 \cdot \left(\frac{E}{MeV}\right)^{1.1083}} \tag{2.9}$$

and the flux reduction factor (δ) due to rigidity cutoff limits is approximately equal to unity for Earth albedo antineutron production. Fit accuracy at higher flux values was emphasized since these play the greatest role in the formation of the antiproton belt. Figure (2.4) shows the estimated flux at four albedo angles.

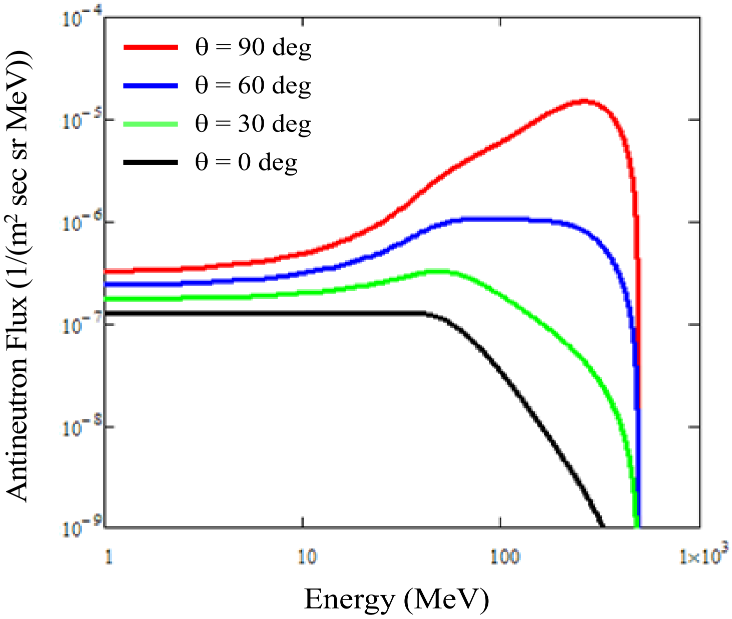

Figure 2.4 – Earth's albedo differential antineutron flux.

Conveniently, the albedo neutron spectrum was also available from the simulation and a fit was generated for this as well. The albedo neutron flux is approximately,

$$j_n = \delta \cdot a_n \left(\frac{E}{MeV}\right)^{b_n} \frac{1}{m^2 \cdot s \cdot sr \cdot MeV} \tag{2.10}$$

where

$$a_n = 470.4 - 1.375\frac{\theta}{\deg} - 0.0106\left(\frac{\theta}{\deg}\right)^2 \qquad \text{for E < ~100 MeV} \tag{2.11}$$

$$b_n = -1.17 - 9.62 \cdot 10^{-4}\frac{\theta}{\deg} - 7.70 \cdot 10^{-6}\left(\frac{\theta}{\deg}\right)^2 \qquad \text{for E < ~100 MeV} \tag{2.12}$$

$$a_n = 4.72 \cdot 10^{11} e^{-0.20\frac{\theta}{\deg}} \qquad \text{for E > ~150 MeV} \tag{2.13}$$

$$b_n = 0.0413\frac{\theta}{\deg} - 5.5672 \qquad \text{for E > ~150 MeV} \tag{2.14}$$

and

$$\delta = \frac{1}{1 + 0.4114 \cdot \left(\frac{E_{pcut}}{GeV}\right)^{1.4935}} \tag{2.15}$$

where E_{pcut} is the cutoff energy for GCR protons at the latitude (λ) of interest which can be calculated based on equation (2.6). There is a noticeable knee in the curve at around 120 MeV. The fit does not accurately capture this behavior. Validation simulations used the minimum flux value in the transition range. However, this will still over predict the neutron flux through the transition regime. The antineutron production efficiency relative to neutron production is shown in figure (2.5). The unusual behavior near 100 MeV for shallow angles is due to the error generated from the fit in the transition region. The neutron/antineutron production efficiency varies between ~1:10^4 and ~1:10^{10}, which is substantially better than the Pugacheva's estimate likely due to the influence of shallow angle scattering.

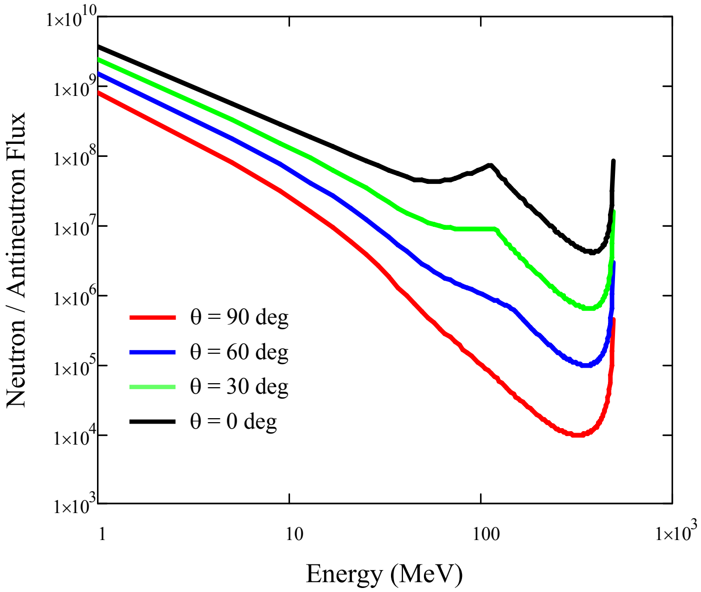

Figure 2.5 – Relative albedo neutron to antineutron flux near Earth.

There is another local source of antiparticles near the Earth. The GCR flux directly produces antiprotons via pair production in the Earth's exosphere. This has been studied previously in several papers (Pugacheva, 2003; Gusev, 2003; Derome, 2003; Spjeldvik, 2005). Figure (2.6) shows the predicted production spectrum of antiprotons in the exosphere normalized to the density of the atmosphere based on Geant4 simulations. Unlike the antineutron decay process, antiprotons are trapped on the L shell where they are initially pair produced since their charge prevents them from freely traversing the magnetosphere to a higher L shell. There is a careful balance here since production at lower altitudes results in much higher fluxes but also in much higher loss rates due to interactions with the upper atmosphere.

The number of trapped antiprotons formed from direct production in the Earth's exosphere appears to be negligible since the relative source is small and the majority of the flux generated is > 1 GeV, which is above the trapping limits for the Earth's magnetic field according to equation (2.4) and empirical observations of the Earth's radiation belts. The maximum directly produced antiproton flux will occur at an altitude < 40 km where the density is near the mean free path of a typical antiproton traveling through the atmosphere (~50-100 gm/cm^2).

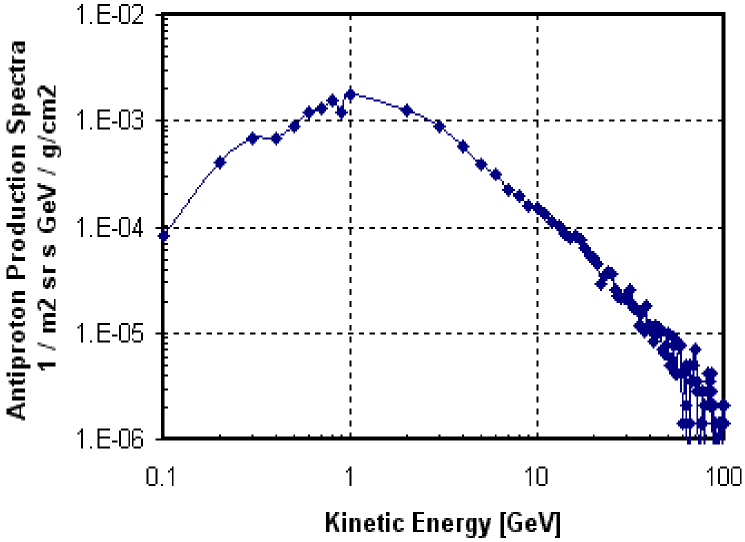

Figure 2.6 – Antiproton Production Spectrum in the Earth's Exosphere at L=1.2.

ALBEDO NEUTRON AND ANTINEUTRON INJECTION MODEL

A model which mathematically describes the physics of cosmic ray albedo neutron decay (CRAND) is required to estimate the source function for the antiproton radiation belt. The basic properties are the same for neutron and antineutron decay though the flux generated by the atmosphere differs between the two. Otherwise, the basic physics of the injection process are identical between matter and its antimatter counterpart. A quasi-closed form solution for the decay and injection process was developed based on common vector rotations to describe the appropriate geometry of the system. Figure (2.7) shows a diagram of the relevant geometry describing the problem.

We will start with an idealized spherical planet of unity radius located at the origin surrounded by a dipole field aligned with the y-axis in Cartesian coordinates. First, we will define a vector in the Earth centered reference frame pointing to the atmospheric source of the albedo neutron/anti-neutron. The vector ($\mathbf{v_e}$) can be found by rotating the vector [1 0 0] around the z-axis by an angle equal to the source latitude (λ_s) in magnetic coordinates. Here we have neglected the thickness of the atmosphere and assumed that all source particles are generated at the surface. Therefore,

$$v_e = \begin{pmatrix} \cos(\lambda_s) & -\sin(\lambda_s) & 0 \\ \sin(\lambda_s) & \cos(\lambda_s) & 0 \\ 0 & 0 & 1 \end{pmatrix} \begin{pmatrix} 1 \\ 0 \\ 0 \end{pmatrix} \tag{2.16}$$

though the unit vector can be scaled to represent an arbitrary formation altitude if so desired. Now we will define a second vector ($\mathbf{v_s}$) aligned with the motion of the particle as it leaves the atmosphere. This can be found by rotating the surface normal reference frame ($\sim\mathbf{v_e}$) by the heading relative to North (ϕ) and albedo angle (θ) of the particle leaving the atmosphere. Combined we have,

$$v_s = \begin{pmatrix} \cos(\lambda_s) & -\sin(\lambda_s) & 0 \\ \sin(\lambda_s) & \cos(\lambda_s) & 0 \\ 0 & 0 & 1 \end{pmatrix} \begin{pmatrix} 1 & 0 & 0 \\ 0 & \cos(\phi) & \sin(\phi) \\ 0 & -\sin(\phi) & \cos(\phi) \end{pmatrix} \begin{pmatrix} \cos(\theta) & \sin(\theta) & 0 \\ \sin(\theta) & \cos(\theta) & 0 \\ 0 & 0 & 1 \end{pmatrix} \begin{pmatrix} 1 \\ 0 \\ 0 \end{pmatrix}. \tag{2.17}$$

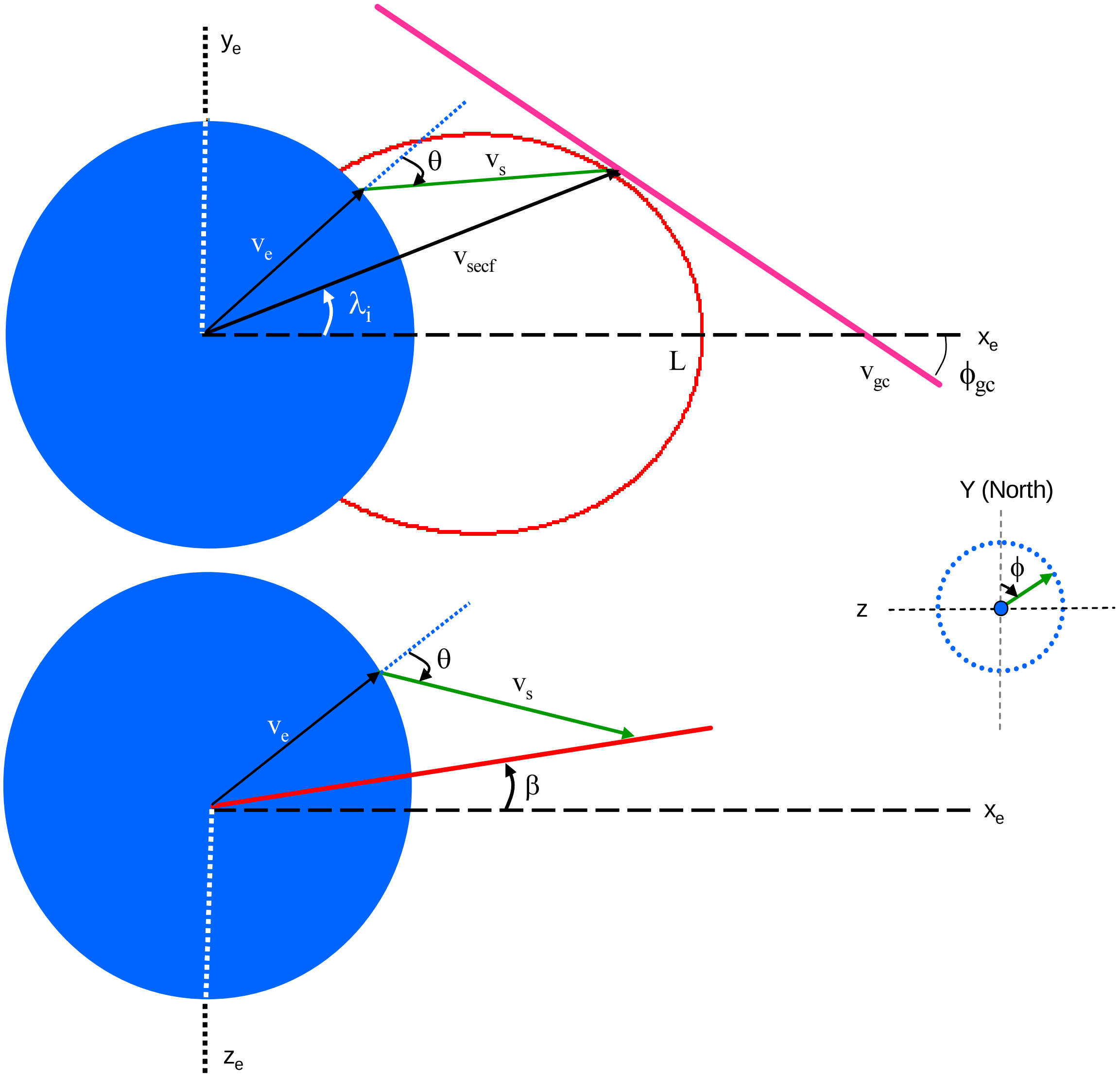

Figure 2.7 – Albedo particle decay model geometry.

Though the figure shows this vector with the tail at the atmospheric source, it is actually a unit vector with the tail at the origin. We can combine it with the flight path vector of the particle to estimate the injection point where the (anti)neutron decays in the Earth reference frame. The injection point at decay is,

$$v_{iecf} = kv_s + v_e \tag{2.18}$$

where *k* is a path length multiplier used to scale the length of the trajectory before the (anti)neutron decays. Now we need to rotate the L shell reference frame so it coincides with the injection point. We originally assumed that the source point was in the XY plane based on equation (2.16). The L shell where the injection occurred will be at some angle relative to the original reference frame. The resulting rotation angle (longitude) about the y-axis is,

$$\beta = \tan^{-1}\left(\frac{v_{iecf\,3}}{v_{iecf\,1}}\right) \tag{2.19}$$

where *1* and *3* denote the x and z vector components of $\boldsymbol{v_{iecf}}$ and β is defined between ±π. Similarly, we can find the injection latitude,

$$\lambda_i = \tan^{-1}\left(\frac{v_{iecf\,2}}{\sqrt{v_{iecf\,1}^{\;2} + v_{iecf\,3}^{\;2}}}\right). \tag{2.20}$$

Now we must determine the L shell of the injection point. For simplicity, we will assume a dipole field centered at the origin. The field lines are,

$$r = R_0 \cos(\lambda) \ . \tag{2.21}$$

The vector components of the field lines at a given latitude λ and longitude β are,

$$\begin{pmatrix} v_x \\ v_y \\ v_z \end{pmatrix} = \begin{pmatrix} L \cdot \cos^3(\lambda) \cdot \cos(\beta) \\ L \cdot \cos^2(\lambda) \cdot \sin(\lambda) \\ L \cdot \cos^3(\lambda) \cdot \sin(\beta) \end{pmatrix} . \tag{2.22}$$

Combining the y component of (18) with the y component of (22) allows us to solve for L directly with simple algebraic manipulation. The L shell of the injection point is therefore,

$$L_i = \frac{v_{iecf\,2}}{\cos^2(\lambda) \cdot \sin(\lambda)} \ . \tag{2.23}$$

Now we can move on to find the equatorial pitch angle of the injected particle. We start by finding the guiding center angle (ϕ_{gc}) relative to the rotated L shell frame by relating the Cartesian coordinates to the polar reference frame used to describe the L shell in equation (2.21). The derivative of the field line is,

$$\frac{dy}{dx} = \frac{\frac{dr}{d\lambda}\sin(\lambda) + r\cos(\lambda)}{\frac{dr}{d\lambda}\cos(\lambda) - r\sin(\lambda)} \tag{2.24}$$

where

$$\frac{dr}{d\lambda} = -2R_0 \cos(\lambda)\sin(\lambda) \ . \tag{2.25}$$

Combing (2.24) and (2.25), yields,

$$\frac{dy}{dx}=\frac{2-3\cos^2(\lambda)}{3\cos(\lambda)\sin(\lambda)} \quad . \tag{2.26}$$

The guiding center vector for in the non-rotated frame is therefore,

$$v_{gc0}=\begin{pmatrix} 3\cos(\lambda)\sin(\lambda) \\ 2-3\cos^2(\lambda) \\ 0 \end{pmatrix}. \tag{2.27}$$

The guiding center vector for a given injection point can be found by rotating by the longitude so that,

$$v_{gc}=\begin{pmatrix} \cos(\beta) & 0 & -\sin(\beta) \\ 0 & 1 & 0 \\ \sin(\beta) & 0 & \cos(\beta) \end{pmatrix}\begin{pmatrix} 3\cos(\lambda)\sin(\lambda) \\ 2-3\cos^2(\lambda) \\ 0 \end{pmatrix}. \tag{2.28}$$

The local pitch angle at the injection point can be found by taking the dot product of the guiding center and source vectors where,

$$\alpha_i=\cos^{-1}\left(v_{gc}\cdot v_s\right). \tag{2.29}$$

The ejected (anti)proton from the (anti)neutron decay process is injected nearly along the initial trajectory due to conservation of momentum. Therefore, equation (2.29) closely represents the average injected pitch angle of the (anti)proton. The equatorial pitch angle can then be compared to the local pitch angle at the injection point by utilizing the simple relationship,

$$\frac{\sin^2(\alpha_0)}{B_0}=\frac{\sin^2(\alpha_i)}{B_i} \tag{2.30}$$

The magnetic field intensity along a field can be related to the equatorial strength with,

$$B_i=B_0\frac{\sqrt{1+3\sin^2(\lambda_i)}}{\cos^6(\lambda_i)}. \tag{2.31}$$

Combining equation (2.30) with (2.31) and solving algebraically, the equatorial pitch angle is,

$$\alpha_0=-\sin^{-1}\left[\cdot\cdot\frac{\sin(\alpha_i)\cdot\cos^2(\lambda_i)}{4-3\cos^2(\lambda_i)}\cdot\left(\cos^2(\lambda_i)\cdot\sqrt{\left(4-3\cos^2(\lambda_i)\right)^{3/2}}\right)\right]. \tag{2.32}$$

By combining the equations for the injected L shell (equation 2.23) and equatorial pitch angle (equation 2.32) with equations (2.17, 2.18, and 2.20) one can determine the trapping parameters for a source particle originating at some arbitrary latitude (λ_s), heading (ϕ) and albedo angle (θ) for a relative path length (k). Figure (2.8) shows an example of the albedo neutron trajectory intersecting the magnetic field line.

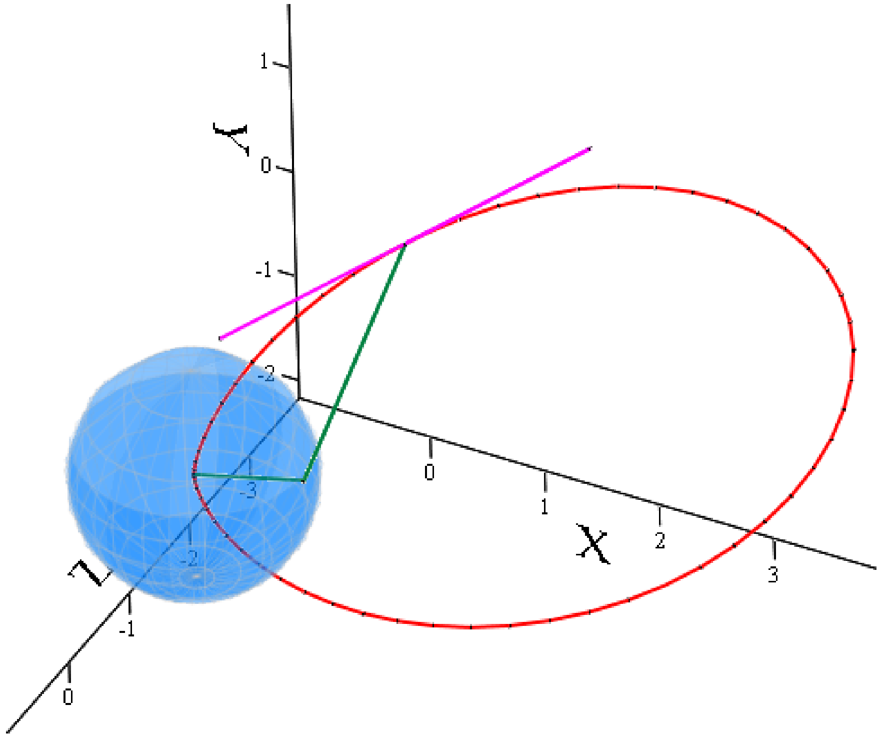

Figure 2.8 – Albedo particle injection example.

At this point, it is necessary to apply this for a distribution of possible trajectories. Using a Monte Carlo approach, the equations are solved for an arbitrary number of points (n_{pts}) uniformly distributed across appropriate ranges. The raw distribution,

$$H_q\begin{bmatrix} 0 < k_q < k_{\max} \\ 0 < \theta_q < \dfrac{\pi}{2} \\ 0 < \phi_q < 2\pi \\ 0 < \sin^{-1}\left(\lambda_{sq}\right) < 1 \end{bmatrix} = \begin{matrix} L\left(\lambda_{sq}, \theta_q, \phi_q, k_q\right) \\ \alpha_0\left(\lambda_{sq}, \theta_q, \phi_q, k_q\right) \end{matrix} \text{ for } j = 1 \ldots n_{pts} \tag{2.33}$$

is computed for 10^7 or more particles, which are then binned according to their injected L shell and pitch angle. The maximum path length multiplier (k_{max}) is set to five (5) or more to cover the maximum L shell range of interest for the problem. The source latitude distribution is purposefully skewed to account for the change in surface area with latitude.

The Monte Carlo distribution is then binned to determine the number of elements (cardinality) in each subset which satisfy the criteria for the phase-space limits at each index across desired L shell and pitch angle ranges. The two dimensional histogram is given as a collection of subsets,

$$I_{f,h} \subset H_j\begin{bmatrix} L_f < L_q < L_{f+1} \\ \alpha_{0h} < \alpha_{0q} < \alpha_{0h+1} \end{bmatrix}. \tag{2.34}$$

The number of elements in each set,

$$n_{f,h} = \left| I_{f,h} \right| \tag{2.35}$$

provides a measure of the strength of the injection process in that segment of the phase space. Figure (2.9) shows the total number of particles in each phase subspace for a simulation with 10^7 and $k_{max} = 8$ (where all particles in the simulation decay when the path length is less than 8 times the radius of the planet.). Note that the histogram has been limited to a smaller subset ($L < 6$) of the overall simulation domain.

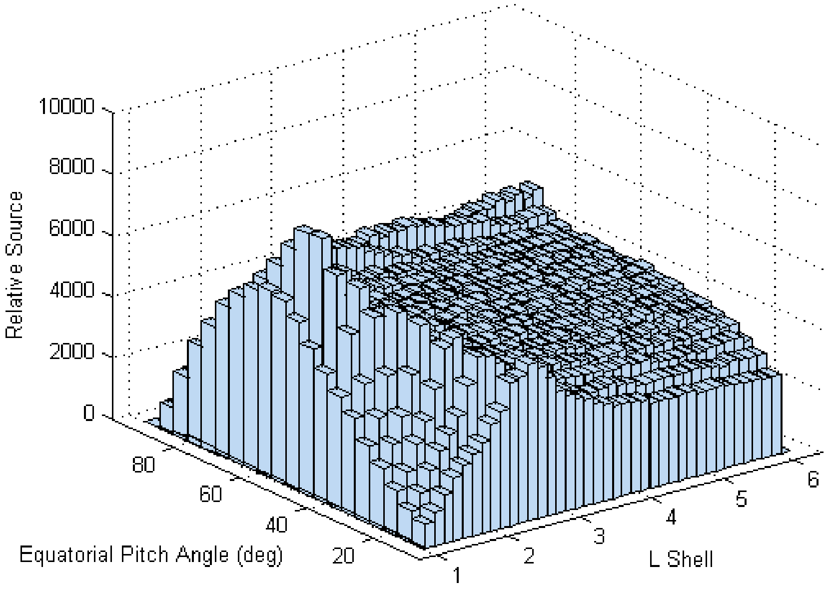

Figure 2.9 – Relative CRAND source strength ($n_{pts} = 10^6$).

To estimate the actual injected flux, we have to calculate the total number of particles which decay within the region. It is functionally dependent on the total antineutron source flux which varies with both latitude and albedo angle. We start by calculating the differential flux for each element of the subspace. The effective differential flux is found by averaging each element based on its source latitude and albedo angle. The differential flux is thus calculated with,

$$j_{dflux\ f,h} = \frac{\sum_{q} I_{f,h} \cdot j_{\bar{n}}}{n_{f,h}} \tag{2.36}$$

where j_n is calculated from equation (2.7) based on θ_q and λ_{iq} for the elements of the subset $I_{f,h}$. If entire planet had such an average flux, the total number of albedo particles injected into the phase subspace would be,

$$j_{tot\ f,h} = \frac{n_{f,h}}{n_{pts}} \int_{E_d}^{E_{d+1}} 4\pi \cdot 2\pi \cdot R_p^{\ 2} \cdot j_{dflux\ f,h} dE \tag{2.37}$$

when integrated over 2π sr and the energy band of interest ($E_d < E < E_{d+1}$). Notice that the expression has been weighted by the number of elements in the subspace divided by the total number of particles used in the initial simulation.

Only a small percentage of the albedo particles will actually decay within the trapping region of the magnetosphere. To calculate the actual number of injected particles into a given phase subspace, we must normalize by the number of particles in the simulation that would actually decay within the trapping region. The source function then becomes,

$$\left.\frac{df}{dt}\right|_{CRAND} = \dot{j}_{tot\ f,h} \frac{k_{\max} \cdot R_p}{v \cdot \gamma \cdot \tau_n} \tag{2.38}$$

where v is the particle velocity at the relevant energy, γ is related relativistic correction factor, and τ_n is the (anti)neutron decay time constant (886 seconds). When combined, figure (2.10) plots the resulting injected flux from antineutron decay. A peak is seen at low L shells (expected due to r^2 effects) and mid-range equatorial pitch angles. There is a sharp fall-off in the source for equatorial pitch angles near 90 degrees due to the low probability of source antineutrons being generated near the local zenith angle. Albedo particles exiting the atmosphere at shallow angles near the equator and on an East or West heading are capable of being injected with an equatorial pitch angle near 90 degrees, but there is little production area for this.

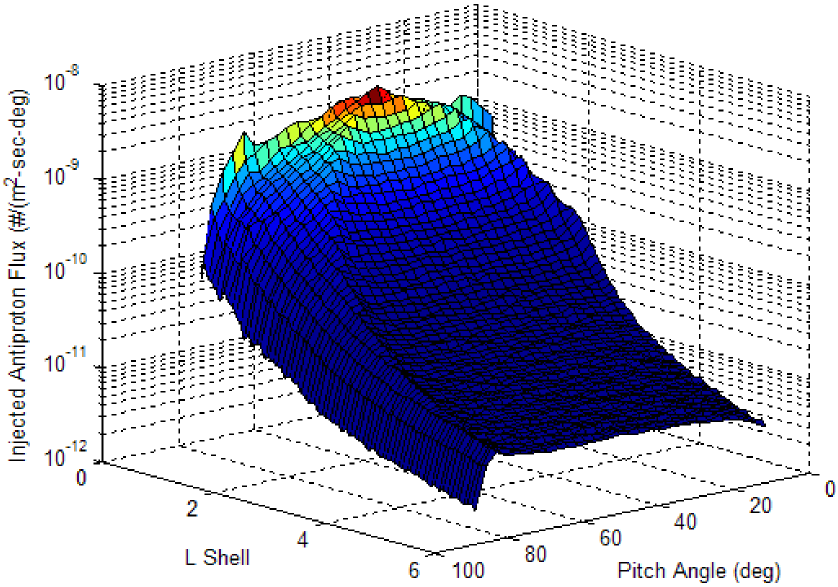

Figure 2.10 –Integrated antiproton source function for Earth (E > 1 MeV).

LOSS TERMS

Losses come from several sources which can cause the protons to be removed or redistributed in phase space. The major losses for antiprotons trapped in the magnetosphere include annihilation with free or nuclei bound protons and energy losses from the ionization of neutral species in the atmosphere. The particle's energy can also change due to adiabatic heating or cooling as the geomagnetic field strength decreases or increases respectively. Figure (2.11) shows the timescale of the relevant antiproton loss and transport processes operating in the magnetosphere. The two true loss mechanisms are from inelastic collisions with the atmosphere (annihilation) and instabilities at higher L shells. Coulomb losses are not true losses per se but instead degrade the energy of the trapped antiproton population. Radial diffusion is also not a true loss mechanism, but rather transports the particles to regions where annihilation or instability losses are more likely to occur. Protons also experience losses due to charge exchange though this is not a relevant loss mechanism for antiprotons since there are no neutral anti-atoms in the atmosphere for the exchange to occur with.

The plot shows the annihilation loss timescale (time until 1/e of the flux is lost) as a function of the magnetic L shell (altitude) for particles with an equatorial pitch angle near 90 degrees. Particles with smaller pitch angles will be lost faster due to the higher loss rates when mirroring at lower altitudes. The particles are transported via radial diffusion in the magnetosphere. This is largely independent of particle energy, but is influenced by the severity of the ambient field fluctuations, which is in turn related to the level of solar activity. The timescale shown is the ensemble-average of the timescale for the particles to be transported a distance of $(\Delta L)^2$.

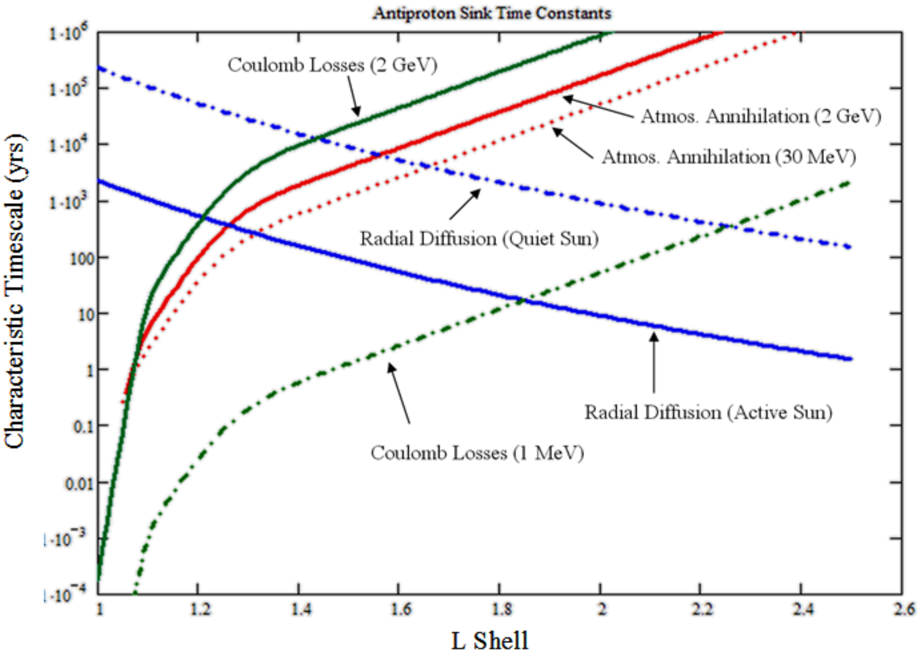

Figure 2.11 – Characteristic loss and transport timescale for antiprotons in the Earth's magnetosphere.

AVERAGE ATMOSPHERE

An accurate accounting of the loss processes must include estimates for the average atmosphere that the particle will pass through over its trajectory. The average number density must therefore be found for each species along its trajectory. In order to obtain the bounce and drift averaged trajectories through the atmosphere, we will start with the guiding center path along a field line,

$$s_{gc} = \int_{\lambda_1}^{\lambda_1} L \cdot R_p \cdot \sqrt{1 + 3 \cdot \sin^2(\lambda)} \cdot \cos(\lambda) \cdot d\lambda . \tag{2.39}$$

In a dipole field, the pitch angle as a function of latitude and equatorial pitch angle can be determined algebraically by using,

$$\sin^2(\alpha_0) = \frac{\sin^2(\alpha_i)}{\frac{\sqrt{1+3\sin^2(\lambda)}}{\cos^6(\lambda)}} \tag{2.40}$$

to solve for the instantaneous pitch angle as a function of equatorial pitch angle and latitude. The resulting equation,

$$\alpha_i = \sin^{-1}\left[\frac{\sin(\alpha_0)}{\cos^4(\lambda)}\left(\sqrt{\cos^2(\lambda)\sqrt{4-3\cos^2(\lambda)}}\right)\right] \tag{2.41}$$

can then be applied to equation (2.39) to determine the total distance traversed by the particle moving between latitudes λ_1 and λ_2. Since the ratio of the guiding center path length to the total path length goes as cos(α), the solution becomes

$$s_{tot} = \int_{\lambda_1}^{\lambda_1} \frac{L \cdot R_p \cdot \sqrt{1+3\cdot\sin^2(\lambda)} \cdot \cos(\lambda)}{\cos\left(\sin^{-1}\left[\frac{\sin(\alpha_0)}{\cos^4(\lambda)}\left(\sqrt{\cos^2(\lambda)\sqrt{4-3\cos^2(\lambda)}}\right)\right]\right)} \cdot d\lambda\,. \tag{2.42}$$

To determine the total path length over one bounce period, we must determine the mirror latitude as a function of the equatorial pitch angle. Since the pitch angle at the mirror latitude will be equal to 90 degrees, we can modify equation (2.40) so that,

$$\sin^2(\alpha_0) = \frac{1}{\frac{\sqrt{1+3\sin^2(\lambda_m)}}{\cos^6(\lambda_m)}} \tag{2.43}$$

and iteratively solve for the mirror latitude λ_m. Figure (2.12) shows the mirror latitude solution.

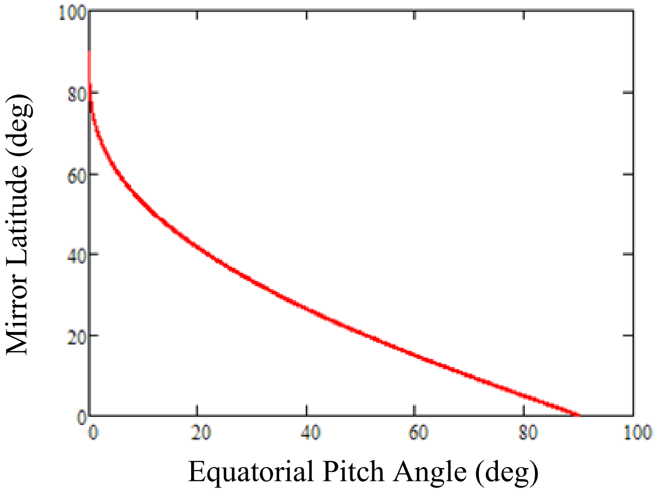

Figure 2.12 – Mirror latitude dependence on equatorial pitch angle.

The total distance traveled over one bounce is therefore,

$$s_b = 4\int_0^{\lambda_m} \frac{L \cdot R_p \cdot \sqrt{1+3 \cdot \sin^2(\lambda)} \cdot \cos(\lambda)}{\cos\left(\sin^{-1}\left[\frac{\sin(\alpha_0)}{\cos^4(\lambda)}\left(\sqrt{\cos^2(\lambda)\sqrt{4-3\cos^2(\lambda)}}\right)\right]\right)} \cdot d\lambda \tag{2.44}$$

where the total distance has been multiplied by a factor of 4 to account for the path back and forth between both the Northern and Southern hemispheres. The bounce period can be easily found by dividing the above expression by the energy dependent particle velocity so

$$\tau_b = \frac{s_b}{v}. \tag{2.45}$$

We can find the interaction rate with the atmosphere as a function of time by including the number density for a given species within the integral of equation (2.44) and dividing by the bounce period so that,

$$\rho_A = \frac{4\int_0^{\lambda_m} \frac{n_A \cdot L \cdot R_p \cdot \sqrt{1+3 \cdot \sin^2(\lambda)} \cdot \cos(\lambda)}{\cos\left(\sin^{-1}\left[\frac{\sin(\alpha_0)}{\cos^4(\lambda)}\left(\sqrt{\cos^2(\lambda)\sqrt{4-3\cos^2(\lambda)}}\right)\right]\right)} \cdot d\lambda}{\tau_b} \tag{2.46}$$

where n_a is the altitude dependent number density of the species of interest. The MSISE-90 (Hedin, 1987) atmosphere model was drift averaged for nominal solar conditions (F10.7 = 140) to estimate typical atmospheric conditions as a function of altitude. Figure (2.13) shows the number density of the four species that play a significant role at magnetosphere altitudes. The altitude can be determined as a function of latitude and equatorial distance with,

$$r = R_0 \cos^2(\lambda) \tag{2.47}$$

for easy inclusion of the atmospheric terms in equation (2.46). The resulting expression provides a drift and bounce averaged atmospheric density for subsequent use to determine loss rates within the belts.

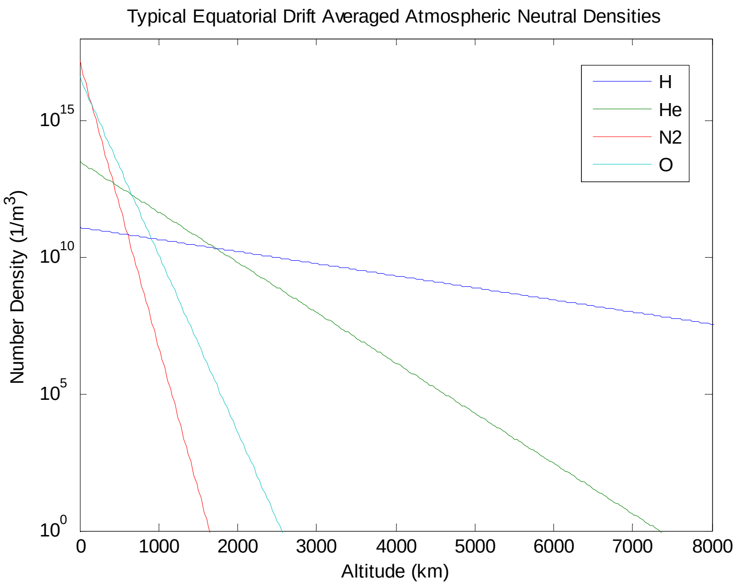

Figure 2.13 – Drift averaged atmospheric model for F10.7 = 140.

INELASTIC LOSSES

Annihilation and other inelastic losses are calculated for drift- and bounce-averaged trajectories through the atmosphere. The annihilation and inelastic loss rate is,

$$\left(\frac{\partial f}{dt}\right)_{annihilation} = f \cdot \sum_{H,He,O,N_2} \sigma_a \cdot \rho_A \tag{2.48}$$

where *f* is the phase space density, ρ_A is the drift and bounce averaged interaction cross section (1/m^2-sec) from equation (2.46) and σ_a is the nuclear interaction cross section (m^2) for each species of interest. Nuclear cross sections were from Meyer (1971) and Letaw (1983) for proton losses and from Tan and Ng (1983) and Moskalenko (2002) for the antiproton cross sections. Little data is available for low energy antiproton cross sections, so the models were extended uniformly for energies below their peak value. Figure (2.14) shows the total inelastic nuclear cross-sections used in the simulations. The equation was calculated along bounce- and drift-averaged trajectories for each segment of phase space and applied to the iterative solution simulation.

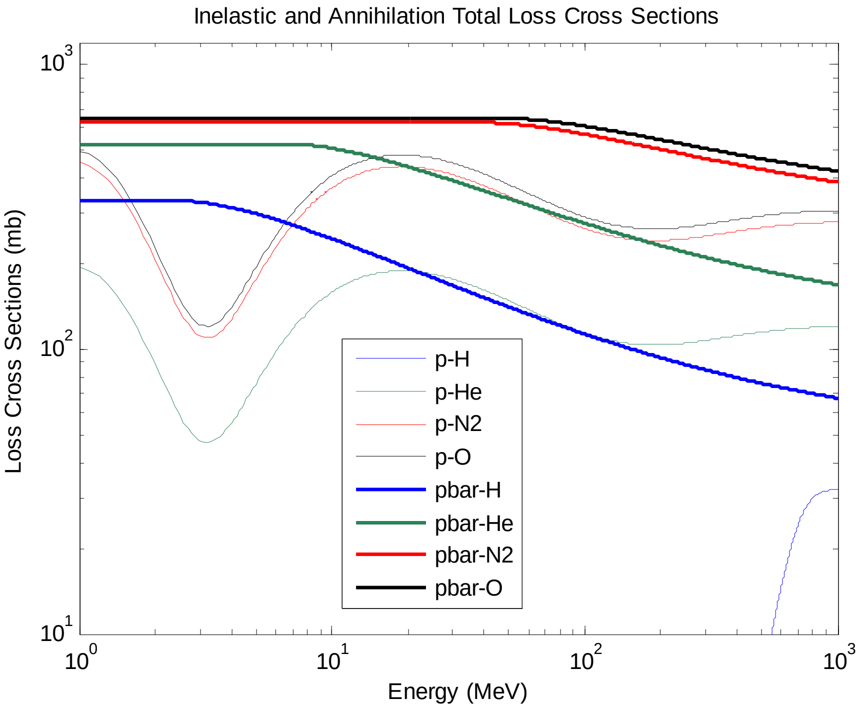

Figure 2.14 – Nuclear cross sections used in calculations.

COULOMB ENERGY LOSSES

Energy loss due to coulomb "friction" with atmospheric neutrals is represented as,

$$\left(\frac{\partial f}{dt}\right)_{Coulomb} = \left(\frac{\partial f}{\partial M}\right)\left(\frac{\partial M}{\partial t}\right) \tag{2.49}$$

where

$$\left(\frac{\partial M}{\partial t}\right) = \left(\frac{\partial E}{\partial t}\right)\left(\frac{\partial M}{\partial E}\right) \tag{2.50}$$

and

$$\frac{\partial E}{\partial t} = -4\pi \cdot z^2 Z \frac{c^3}{\beta} m_e r_e{}^2 n \cdot \left[\ln\left(\frac{4\beta^4 c^4 m_e{}^2}{I^2 \left(\beta^2 - 1\right)^2} \right) - 2\beta^2 \right] \tag{2.51}$$

is based on the Bethe-Bloch equation, which describes the loss of energy per unit time due to atmospheric interactions. The term z is the atomic number of the incident particle, Z is the atomic number of the target species, m_e is the mass of an electron, r_e is the classical electron radius, n is the number density at the target and I is the mean ionization energy for the target. The equation was numerically calculated for bounce and drift averaged trajectories for each segment of the phase space.

STEADY STATE SOLUTION FORM

A convenient form of equation (2.1) must be found so we can determine a steady state solution describing the phase space distribution of the radiation belt. Extending the equation so the source and loss terms are explicitly stated,

$$\frac{\partial f}{dt} = L^2 \frac{\partial}{\partial L}\left[\frac{D_{LL}}{L^2}\frac{\partial f}{\partial L}\right] + \left(\frac{\partial f}{dt}\right)_{CRAND} + \left(\frac{\partial f}{dt}\right)_{Coulomb} + \left(\frac{\partial f}{dt}\right)_{Inelastic} \quad . \tag{2.52}$$

The diffusion coefficient (D$_{LL}$) is a function of L so the diffusion terms must be broken out explicitly using the quotient and product rules. The diffusive portion of the equation is,

$$L^2 \frac{\partial}{\partial L}\left[\frac{D_{LL}}{L^2}\frac{\partial f}{\partial L}\right] = C_{LL}\frac{\partial f}{\partial L} + D_{LL}\frac{\partial^2 f}{\partial L^2} \tag{2.53}$$

where

$$C_{LL} = \frac{\partial D_{LL}}{dL} \tag{2.54}$$

leading to

$$\frac{\partial f}{dt} = C_{LL}\frac{\partial f}{\partial L} + D_{LL}\frac{\partial^2 f}{\partial L^2} + \left(\frac{\partial f}{dt}\right)_{CRAND} + \left(\frac{\partial f}{dt}\right)_{Coulomb} + \left(\frac{\partial f}{dt}\right)_{Inelastic} = 0 \tag{2.55}$$

for the steady state condition where *df/dt=0*. Using a second order central difference approximation,

$$\frac{\partial f}{\partial L} = \frac{f_{iL+1} - f_{iL-1}}{2\Delta L} \tag{2.56}$$

where *iL* is the index where the derivative is being evaluated. Similarly, we have,

$$\frac{\partial^2 f}{\partial L^2} = \frac{f_{iL+1} - 2f + f_{iL-1}}{\Delta L^2} \tag{2.57}$$

assuming uniform grid spacing. To first order with no restrictions on grid spacing,

$$\left(\frac{\partial f}{dt}\right)_{Coulomb} = \left(\frac{\partial f}{\partial M}\right)\left(\frac{\partial M}{\partial t}\right) \tag{2.58}$$

and

$$\left(\frac{\partial f}{\partial M}\right) = \frac{f_{iM-1} - f}{\Delta M} \tag{2.59}$$

with no restrictions on grid spacing. The annihilation losses go as,

$$\left(\frac{\partial f}{dt}\right)_{Annihilation} = f\,\frac{\partial f / \partial t}{f}\,. \tag{2.60}$$

Collecting terms, we obtain,

$$C_{LL}\,\frac{f_{iL+1}-f_{iL-1}}{2\Delta L}+D_{LL}\,\frac{f_{iL+1}-2f+f_{iL-1}}{\Delta L^2}+\frac{f_{iM-1}-f}{\Delta M}\,\frac{\Delta M}{\Delta t}+Sources+f\,\frac{\Delta f / \Delta t}{f}=0 \tag{2.61}$$

The equation can be solved directly for f at grid point (iM, iL). The final form is,

$$f=\frac{S+\dfrac{\partial M / \partial t\cdot f_{iM-1}}{\Delta M}-C_{LL}\,\dfrac{f_{iL-1}-f_{iL+1}}{2\Delta L}+D_{LL}\,\dfrac{f_{iL+1}+f_{iL-1}}{\Delta L^2}}{\dfrac{\partial M / \partial t}{\Delta M}-R_{annilation}+\dfrac{2D_{LL}}{\Delta L^2}} \tag{2.62}$$

which can be applied iteratively throughout the solution domain until it converges to the final result.

EARTH ANTIPROTON BELT RESULTS

A phase space simulation with full source and loss terms was completed with a grid of 70 L shell values between 1 and 6, 30 pitch angle values between 10 and 90 degrees, and 40 magnetic moments which were picked to span the energy range between 1 MeV and 800 MeV. Table (2.1) shows the key parameters found after integrating the results through phase space.

Total Trapped Mass	160 ng
Replenishment Rate	2.0 ng/yr
Peak Equatorial Flux	3800 1/(m^2-sec) for E > 10 MeV
Peak Flux Location	L = 1.4 (alt ~ 2500 km at the equator)

Table 2.1 – Earth antiproton belt characteristics.

Figures (2.15) to (2.20) show results from the antiproton belt simulation of the Earth. A peak in the flux is clearly seen at L ~ 1.4, which equates to an altitude of approximately 2500 km at equatorial latitudes. The long residence time from radial diffusion, a relatively minor loss rate from annihilation at these altitudes, and a strong source function at this location combine to create an area where approximately 4000 antiprotons will pass through each square meter per second. At this location, the energy spectrum peaks near 200 MeV with the greatest flux near a pitch angle of approximately 60 degrees.

The lack of antineutrons generated near zenith prevents the injection of antiprotons close to an equatorial pitch angle of 90 degrees. The pitch angle distribution changes as a function of L shell. For higher L shells, most particles are injected at low altitudes near the loss cone resulting in a narrower distribution of particles near this pitch angle. The energy distribution also changes as a function of L shell. High-energy trapping is limited to lower shells due to trap stability limits.

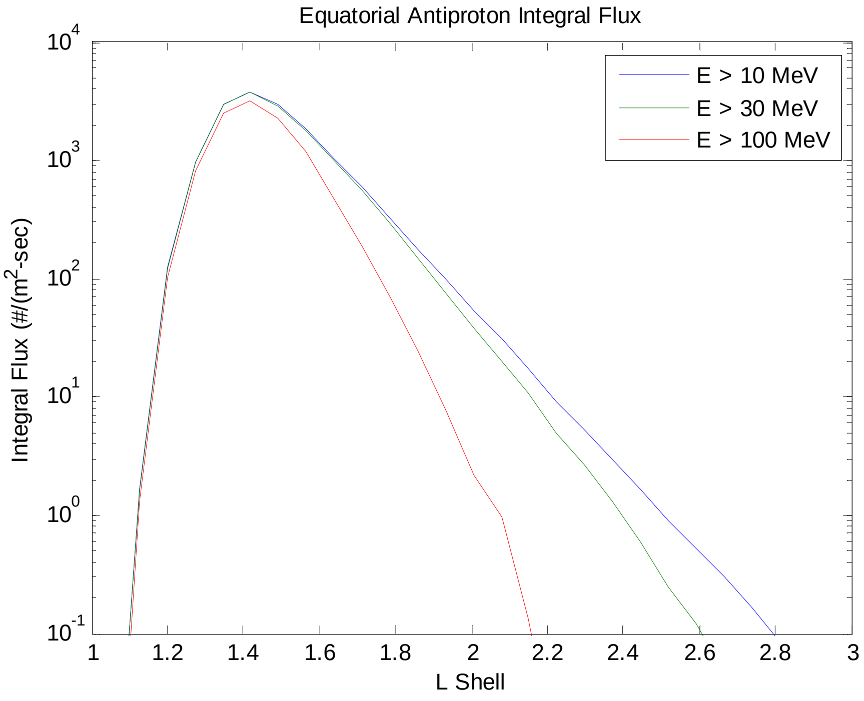

Figure 2.15 – Antiproton integral flux versus L shell (Earth).

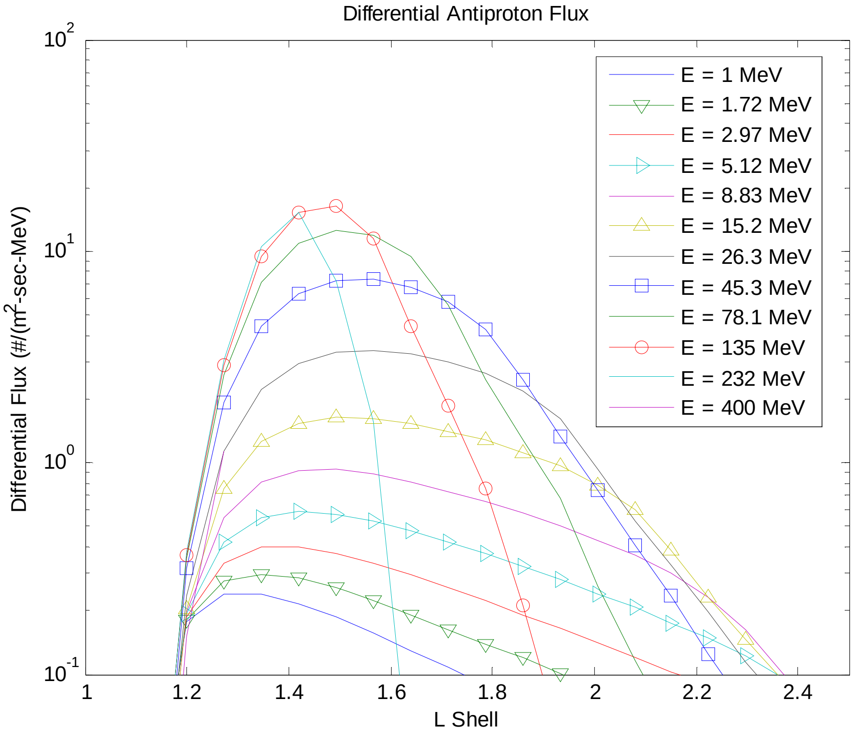

Figure 2.16 – Antiproton differential flux versus L shell (Earth).

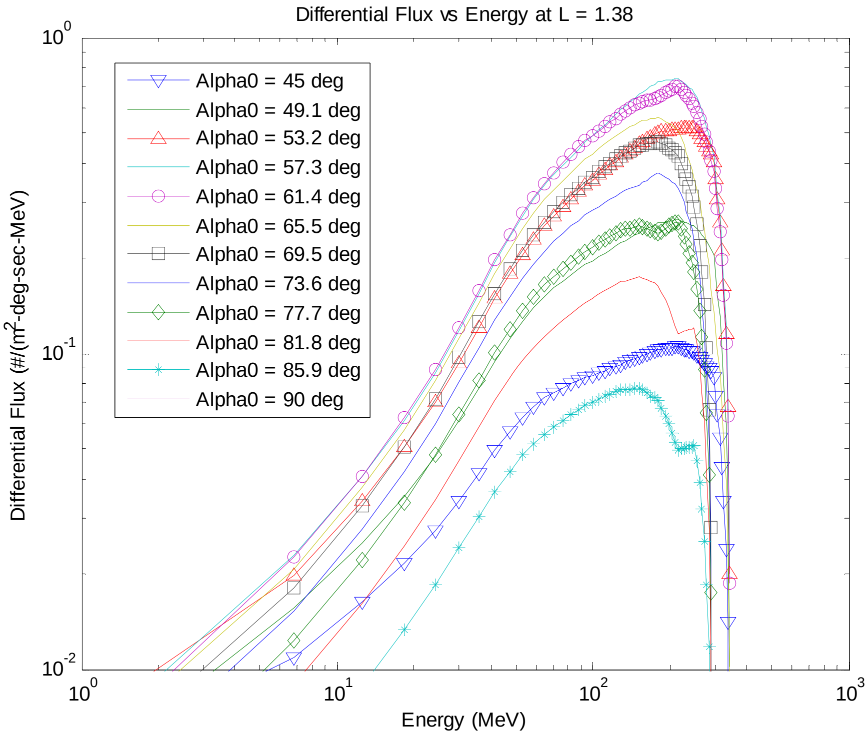

Figure 2.17 – Antiproton differential flux versus energy (Earth).

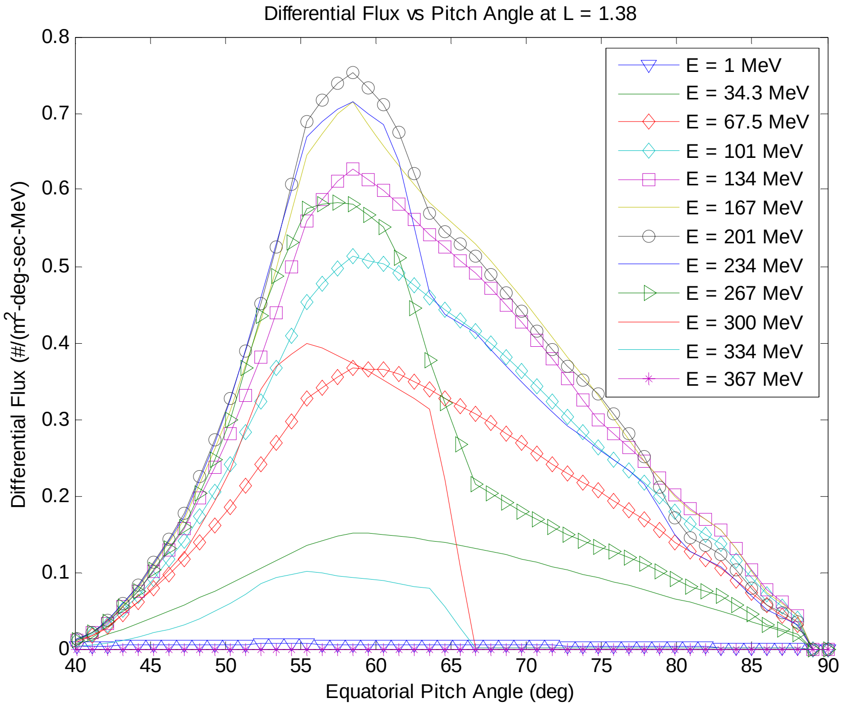

Figure 2.18 – Antiproton differential flux versus pitch angle (Earth).

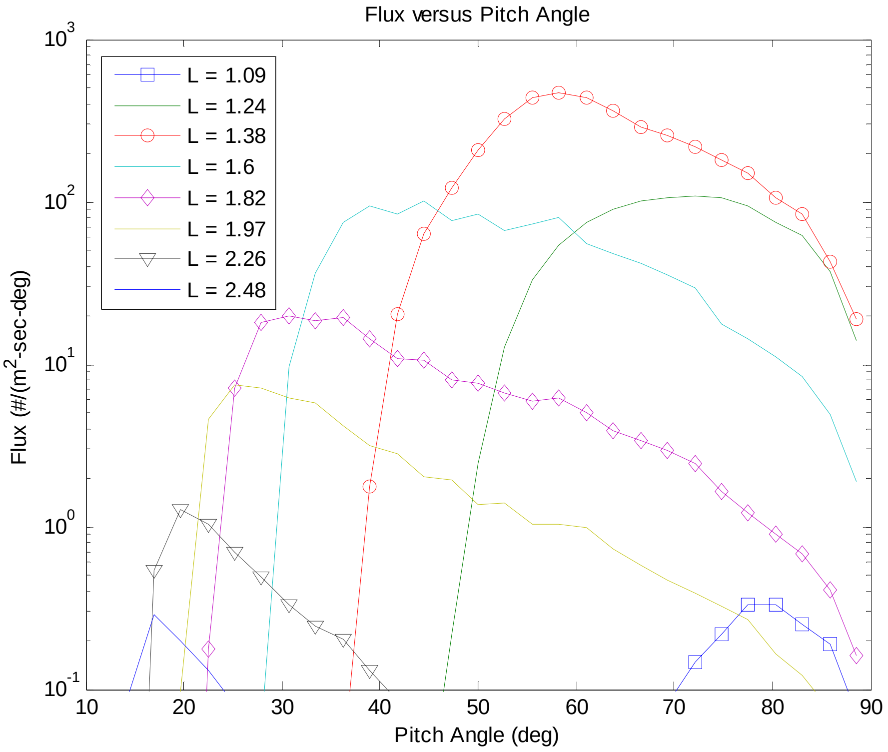

Figure 2.19 – Antiproton flux versus pitch angle for various L shells (Earth).

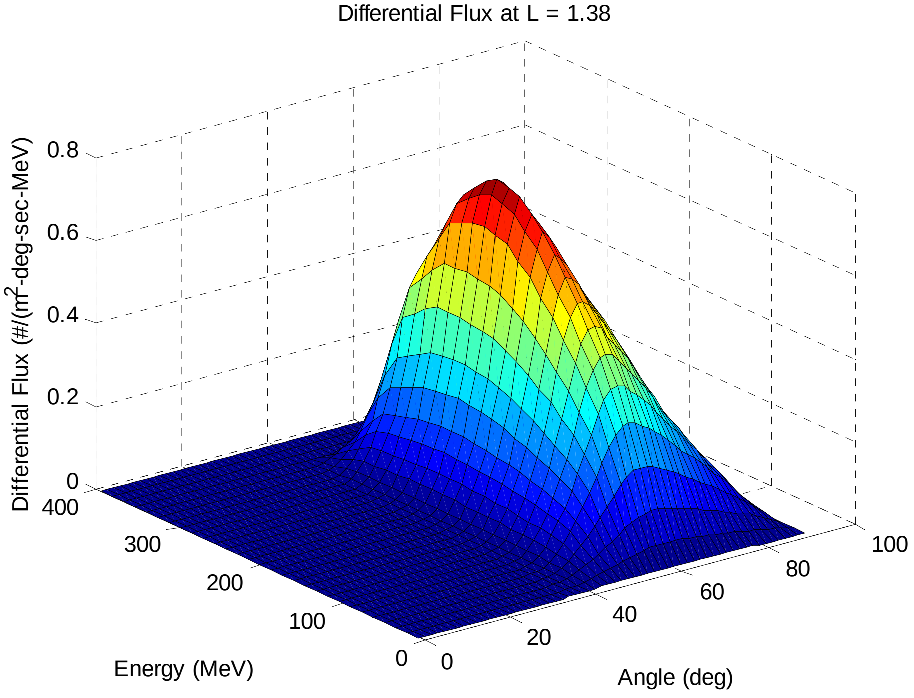

Figure 2.20 – Differential flux at L=1.4 versus energy and pitch angle. .

CODE VALIDATION – PROTON BELT MODEL

Since the general physics which govern proton and antiproton belt evolution are common, a proton belt simulation can be compared to empirical measurements from spacecraft to partially validate the solution technique. The loss processes were modified to match proton cross sections, and the neutron albedo was simulated with Geant4 to determine the strength of the source function. The major aspects of proton physics were duplicated in the simulation with the exception of the external source of solar protons since there is no equivalent antiproton source. This could have been added separately though the results at low L shells and high energies are not greatly influenced by the external source so the general simulation capability could be validated without these conditions.

Figure (2.21) shows the integral flux values as a function of L shell for the simulated domain overlaid on data derived from the AP8 model. The empirical data represents data averaged from numerous spacecraft over several decades of measurements. There is a strong correlation between measured values and those predicted from the model. As expected, the model somewhat underpredicts the flux at high L shells since the model does not include the external diffusive source of solar protons. However, at the peak values where L < 1.8, the model closely follows the empirical data suggesting that the simulation technique is valid. This gives us some measure of confidence in our antiproton results since the only fundamental difference is the change in nuclear cross section.

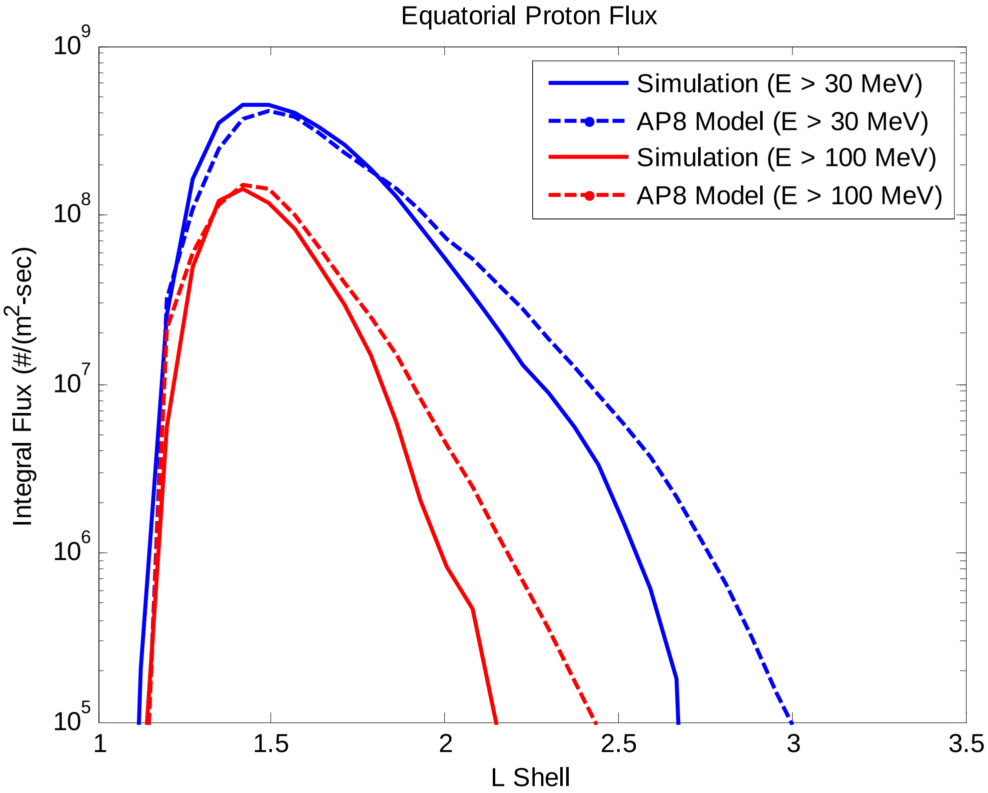

Figure 2.21 – Comparison between measured and simulated proton belt values.

COMPARISON TO PHASE I RESULTS

The new results obtained during phase II are significantly more encouraging than the preliminary extrapolations obtained during phase I. The total estimated trapped mass increased from less than one (1) nanogram to approximately 160 ng. The phase I technique involved extrapolating values from the AP8 proton belt model based on the ratio of internal to external production (CRAND versus solar protons) and the ratio of neutron to antineutron albedo intensity. The three order of magnitude increase in trapped flux may, at first, seem difficult to attribute to the difference between the full simulation and extrapolations. However, a combination of factors contributed to the major change. These factors were identified during phase I though it was only during phase II that a full analysis was available which enabled us to include these parameters. When the phase I technique is updated with the new values, there is a remarkable agreement between the phase I and phase II results which gives us further evidence to support the accuracy of the model since the approaches are fundamentally different from each other but produce similar answers.

The major factors that contributed to the relative increase in the flux are:

- The contribution of albedo antineutrons formed from shallow angle scattering off the atmosphere significantly increases the source function intensity. Though this acts over only a relatively narrow angular range, the relative intensity can increase by five orders of magnitude between production along the horizon and that near zenith. The antineutron/neutron ratio was assumed to be 1:10^9 during phase I though, as figure (2.5) shows, the actual ratio is probably closer to 1:10^6-10^7 when averaged over all angles. The locations where the trapping efficiency is best (low L shells) also corresponds to the areas with the longest residence time which enables the flux to build significantly.

- The relative strength of the antineutron source is not as sensitive to rigidity cutoff limits. The reduction of the GCR flux near the equator due to rigidity cutoff limits can decrease the net albedo neutron flux by more than 20 times since neutrons can be produced by low energy (MeV) spallation reactions. By comparison, antineutron production primarily occurs above 20 GeV, which is beyond the cutoff rigidity for all latitudes.

The gas giants in our solar system are larger in size than the Earth and have significantly stronger magnetic fields. For instance, as shown in table (3.1), the dipole moment of Jupiter is nearly 20,000 times larger than Earth's. Measured radiation fluxes from robotic spacecraft significantly exceed those measured in the Earth's radiation belts. (Divine and Garret, 1983) Dessler (1983) provides a detailed survey of the Jupiter environment and the models which describe it. One can therefore extrapolate and assume that these planets will also have much higher antiproton fluxes and total integrated mass. In this section, we will explore the relative differences between the production mechanisms and develop full models for the planets that can support radiation belts.

Planet	Dipole Moment	Radius
Earth	7.9 x 10^{25} gauss cm^3	6378 km
Jupiter	1.5 x 10^{30} gauss cm^3	71492 km
Saturn	4.3 x 10^{28} gauss cm^3	60268 km
Uranus	3.8 x 10^{27} gauss cm^3	25559 km
Neptune	2 x 10^{27} gauss cm^3	24764 km

Table 3.1 – Radius and magnetic field parameters for selected planets.

The Jovian planets offer a significantly different environment for the production and loss of antiprotons relative to the region around Earth. Like Earth, antiprotons will be created and lost in the residual atmosphere, but the Jovian planets also have moons, rings, gases, and dust, which influence the antiproton flux. These factors can both help and hinder the formation of an antiproton radiation belt. However, when larger dipole moments and increased planet radii are combined with these effects, the net result is the formation of substantial Jovian antiproton belts.

SIGNIFICANT FACTORS IN THE JOVIAN RADIATION BELTS

The production of antiproton radiation belts around the Jovian planets is influenced by a number of relatively major factors, yielding far more trapped antiprotons. Their large size, strong magnetic fields, and other features such as rings, combine to generate magnetospheres that can support a large population of antiprotons that are quickly replenished. The salient terms influencing the formation of the Jovian radiation belts relative to Earth are discussed in the following sections and summarized in the table below.

Factor	Jovian Scaling	Notes
Increased surface area	↑	Antineutron pair production in the atmosphere increases with the available area. Therefore, larger planets offer more atmospheric material (surface area) for the antineutron production to occur over. The atmospheric area of Jupiter is approximately 125 times larger than Earth.
Cosmic ray cutoff rigidity	↓	The increased area is partially offset by the shielding effect of the magnetic fields of the Jovian planets. The large magnetic moment of the planet prevents much of the GCR flux from reaching the atmosphere where production can occur. This is particularly true at Jupiter where local production decreases by more than 90% at the magnetic equator.
Magnetosphere size	↑	The large magnetic fields of the gas giants also offer advantages. The resulting magnetospheres are substantially larger than the

		Earth's. Therefore, the time of flight for an antineutron to traverse the region is substantially longer allowing a far larger fraction of the particles to decay into antiprotons, which are then trapped. For Jupiter, this increases the total fraction of particles decaying in the field by nearly two orders of magnitude.
Diffusive Transport	↓	The radial transport across Jovian L shells appears to be driven by a different mechanism than in the Earth's magnetosphere. The magnetic and electric perturbations that show a L^{10} dependence around Earth are replaced with centrifugally driven plasma interactions that follow a $L^{3\pm1}$ dependence but with a larger multiplier. This appears to be driven by the low-energy plasma and dust background that tends to surround Jovian planets. As a result, the typical residence time in Jovian magnetospheres is reduced which effectively lowers the magnitude of the built up flux.
Maximum trapping energy	↑	The stronger fields spread over large Jovian magnetospheres enable a far larger fraction of the generated antiproton flux to be trapped. Trap stability limits prevent high-energy particles from being trapped in the Earth's magnetosphere. The Jovian fields are capable of trapping a larger portion of the production spectrum.
Atmospheric constituents	↑	The atmosphere of Jovian planets, which are primarily Hydrogen with a small part Helium and a smaller fraction of the heavier elements, improve the production of albedo antineutrons. The low fraction of neutrons reduces the annihilation cross section and improves the antineutron generation efficiency of the atmosphere.
Planetary rings	↑	The rings surrounding Saturn are an impressive source of antineutrons. The cross sectional thickness of the ring is ideal to maximize the production of particles from interactions with the cosmic ray flux. In comparison to albedo antineutrons produced in the atmosphere, antineutrons produced by the rings do not have to be backscattered to decay in the magnetosphere. The relative efficiency of the production target therefore increases by several orders of magnitude for Saturn. Minor ring structures around other planets are not substantial enough to play a similar role in the generation process.
Moons	↑↓	The natural satellites that orbit the Jovian planets can act as additional targets, which act as both sources and sinks. Their source potential tends to be relatively small due to their small relative size. However, some of the larger moons can absorb a substantial fraction of the flux at a given L shell to act as a moderate loss mechanism relative to diffusive transport.
Dust/gas	↑↓	The dust and gas that often are generated by the natural Jovian satellites (Io torus, E-ring at Saturn) act as both source and loss mechanisms though their relatively low density prevents them from playing a major role in the structure of the antiproton belt.

Table 3.2 - Factors influencing Jovian antiproton radiation belt formation relative to the Earth.

JOVIAN ALBEDO ANTINEUTRON SPECTRUM

The Hydrogen/Helium atmospheric mix found in the atmosphere of Jovian planets is a good target for the generation of albedo antineutrons. The basic physics of the source and injection process are similar to that near Earth, albeit over a much larger spatial scale. Geant4 simulations of a generic atmosphere with 75% Hydrogen and 25% Helium by mass were used to generate fit equations describing the atmospheric flux as a function of energy and albedo angle. Equation (3.1) shows the expression and figure (3.1) plots the resulting albedo antineutron flux as a function of energy for several albedo angles at a rigidity cutoff of 21 GV.

$$j\bar{n}_{jovian} = a_j \left(\frac{\theta}{\deg} \right)^{b_j} \frac{1}{m^2 \cdot s \cdot sr \cdot MeV} \tag{3.1}$$

where

$$b_j = 0.0030583783 \left(\frac{E}{MeV} \right)^{1.2626539} \tag{3.2}$$

and

$$a_j = 8.47 \times 10^{-6} e^{-4.49 b_j} \quad . \tag{3.3}$$

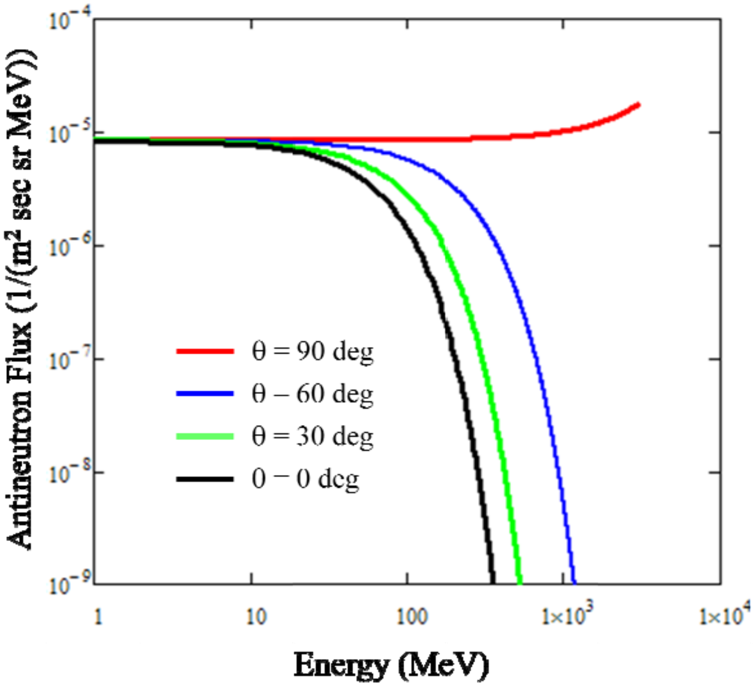

Figure 3.1 – Albedo antineutron spectrum from a typical Jovian atmosphere.

The intensity of the induced flux is slightly improved over the Earth case since the relative scarcity of neutrons in the atmosphere reduces the overall loss rate due to annihilation. However, the flux is reduced when the magnetic field of a planet shields a portion of the GCR spectrum from the atmosphere. The rigidity cutoff limit from equation (2.6) will determine the minimum energy of particles that can strike the atmosphere for a given latitude and altitude in a planetary magnetosphere.

Re-expressed as a function of the minimum proton energy (E_{cut}) and albedo particle energy (E), the flux from figure (3.1) is reduced by the factor (f_c),

$$f_c = b_c + m_c \frac{E}{GeV} \,. \tag{3.4}$$

where,

$$b_c = 1.2711297 - 1.1898622 e^{-155.69769\left(\frac{Ecut}{GeV}\right)^{-1.5517575}} \tag{3.5}$$

$$m_c = 1.6983077 \times 10^{-5} - \frac{0.00032276308}{\frac{Ecut}{GeV}} \,. \tag{3.6}$$

Figure (3.2) shows the resulting flux reduction factor relative to the 20 GeV proton (21 GV) cutoff case.

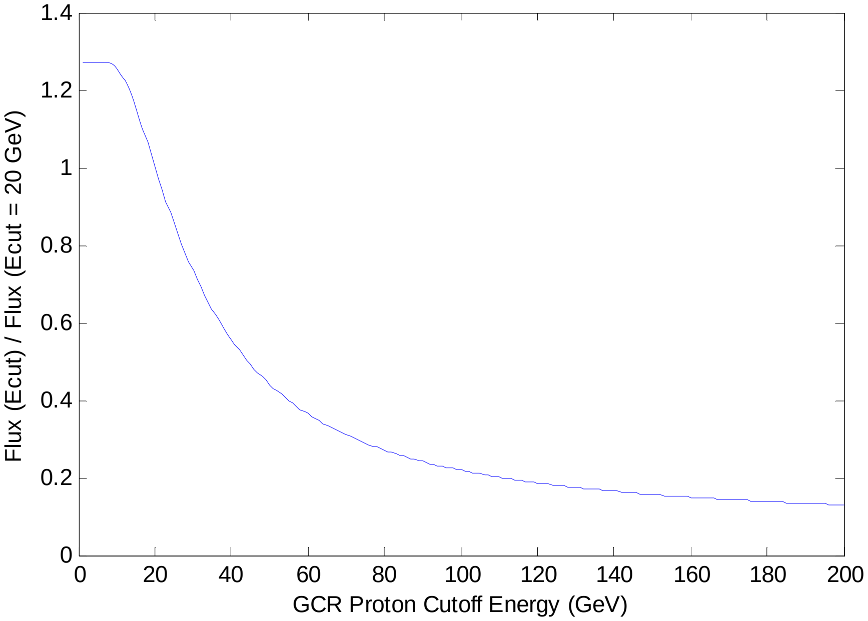

Figure 3.2 – Source reduction factor as a function of the minimum proton energy.

ANTIPARTICLE GENERATION IN SATURN'S RINGS

The rings of Saturn are effectively thin layers of water, which can produce antiparticles from their interaction with high-energy cosmic rays. The ring mass loading is typically close to but less than the mean nuclear interaction length (84 g/cm^2) of protons passing through water. As a result, the antineutron generation is very large compared to the albedo contribution of the atmosphere since the particles need not be backscattered to enter the magnetosphere of the planet.

Nicholson and Dones (1991) reviewed the salient features of the Saturnian ring system including the estimated density of the rings. Figure (3.3) shows the relevant features of the system. The key sections that will generate antiparticles are primarily water ice particles with dimensions spanning the micron to multiple cm range. Due to the slant angle of a cosmic ray passing through the ring, the effective density becomes,

$$\rho_e = \frac{\rho_\perp}{\cos(\theta_r)} \tag{3.7}$$

where θ_r is the angle of incidence relative to a vector normal to the ring. This value was capped at the nuclear interaction length if the path length exceeded this value for shallow approach angles in the dense regions of the ring system.

A combination of particles will be generated as the GCR flux interacts with the ring material. The nuclear events will generate a spray of particles similar to the cosmic ray showers on Earth. Antiprotons will be directly generated but are then trapped on L shells which intersect the ring system and will be quickly reabsorbed. However, antineutrons will leave the local production region and can decay in other parts of the magnetosphere where the antiproton and positron decay products will be trapped.

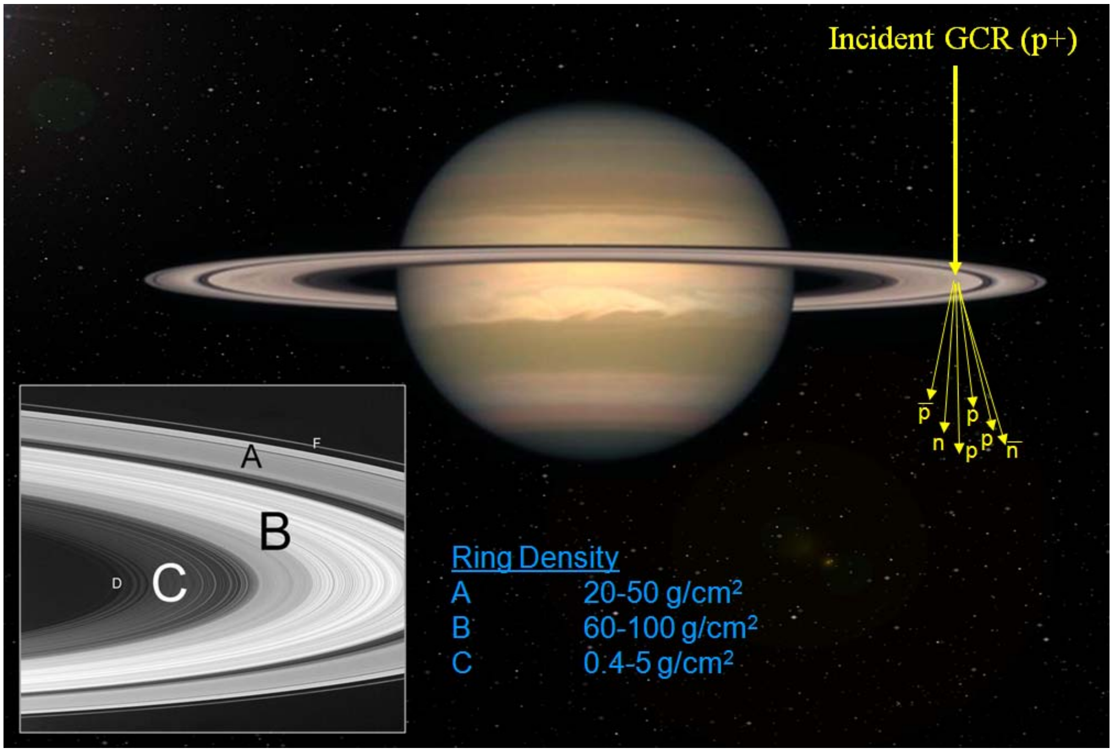

Figure 3.3 – Antiparticle generation in Saturn's rings.

ANTINEUTRON PRODUCTION SPECTRUM THROUGH H_2O

The production spectrum for the ring system was calculated by a Monte Carlo analysis of the GCR flux passing through a 1 gm/cm² slab of water. A fit to the resulting spectrum is given in equation (3.8). Based on a 20 GeV proton cutoff energy in the GCR spectrum, the resulting antineutron (and antiproton) flux is given as,

$$j\bar{n}_{H_20} = \begin{cases} \dfrac{0.9702}{1596.0597 - 0.31073219\frac{E}{MeV} + 7.3672861 \times 10^{-5}\left(\frac{E}{MeV}\right)^2}, & E > 1.5\ GeV \\ 0.00082524007e^{-145.8662\frac{E}{MeV}}, & E \leq 1.5\ GeV \end{cases} \frac{1/(m^2\ s\ sr\ GeV)}{g/cm^2}. \qquad (3.8)$$

These flux values should be scaled by the reduction factor given by equation (3.4) to account for rigidity cutoff effects and the effective ring density from equation (3.7) to estimate the total generated flux. Figure (3.4) shows the resulting flux intensity scaled by the cross sectional density.

The pair produced antiparticles are generated along a narrow distribution following the original trajectory of the source particle. Therefore, due to momentum conservation in the decay process, we can assume that the generated particle follows a trajectory similar to the original GCR source particle.

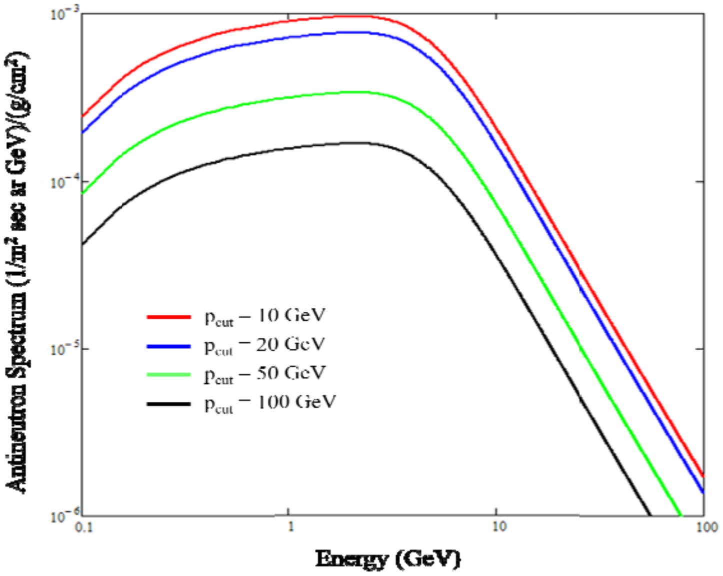

Figure 3.4 – Antineutron production spectrum for GCR flux passing through 1 gm/cm² of water.

RING SOURCE INJECTION MODEL

Similar to the injection model for albedo neutrons generated in planetary atmospheres, a model was developed to analyze the antiproton source function derived from antineutron generation in Saturn's ring system. Figure (3.5) shows the relevant geometry as an antineutron produced in the rings decays after a short distance and is injected into an L shell near the mirror latitude in this example. This trajectory calculation was repeated for more than 10^7 particles exiting the ring system within physical limits.

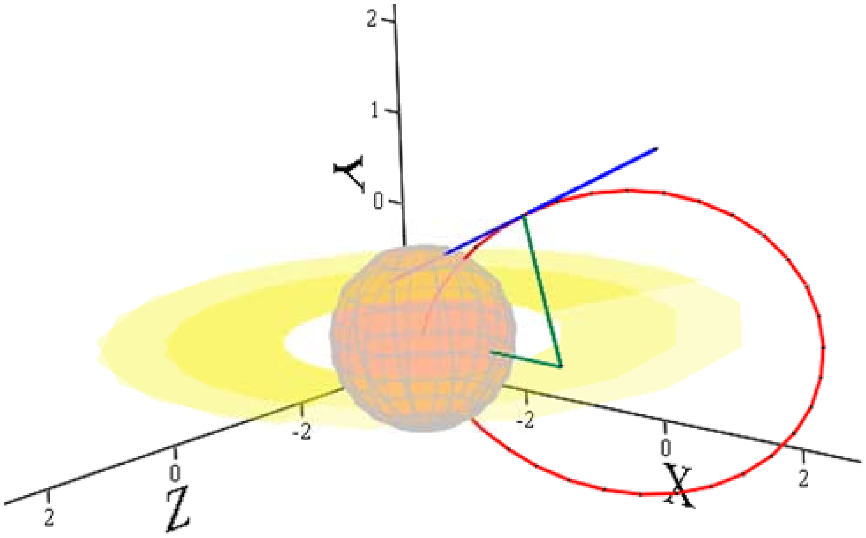

Figure 3.5 – Ring source injection model example.

Similar to the Earth based approach, the source function was calculated as a quasi-closed form solution based on vector rotations. Figure (3.6) shows the relevant geometry where the rings reside in the X-Z plane.

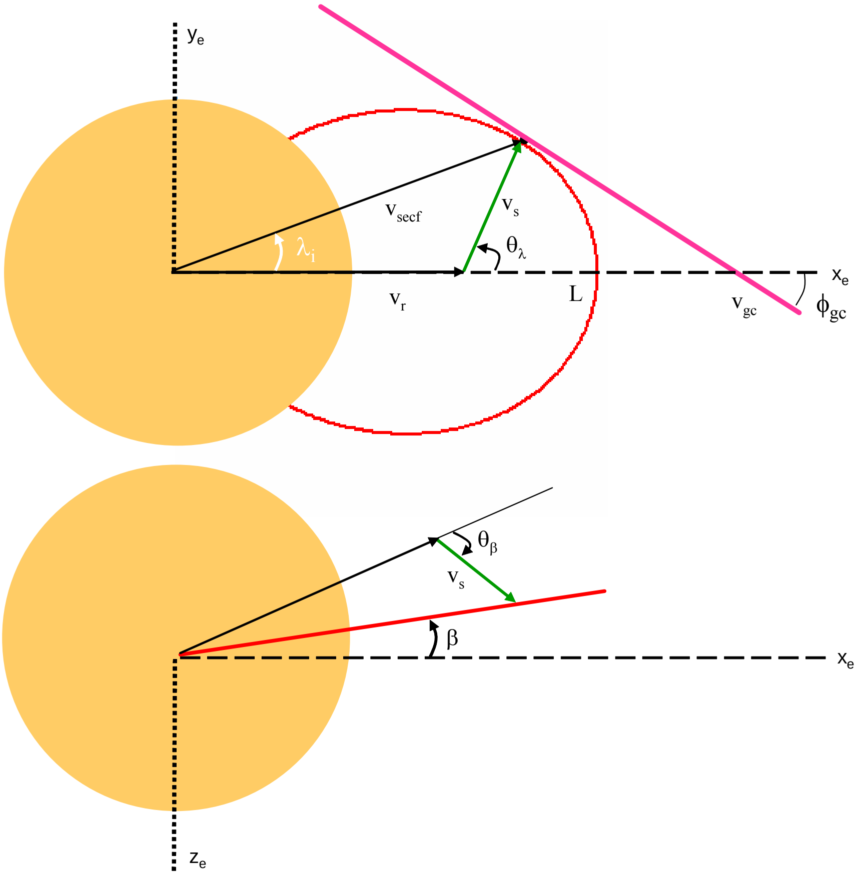

Figure 3.6 – Geometry definitions for the ring source function calculation.

We will start by defining a vector in the Saturn reference frame pointing to the latitude of the source of the albedo neutron / antineutron. Note that the system is symmetrical, so there is no need to perform a rotation in the longitudal direction. The source location vector is,

$$v_r = \begin{bmatrix} L_s \\ 0 \\ 0 \end{bmatrix} \tag{3.9}$$

where L_s is the L shell where the particle originates. The vector which describes the motion of the particle leaving the ring can be found by rotating the reference frame around the surface normal vector to determine heading (relative to North, pos ccw) and then rotating the vector the albedo angle components (θ_λ and θ_β) to determine the angle leaving the atmosphere. The source vector is therefore,

$$v_s = \begin{pmatrix} \cos(\theta_\beta) & 0 & -\sin(\theta_\beta) \\ 0 & 1 & 0 \\ \sin(\theta_\beta) & 0 & \cos(\theta_\beta) \end{pmatrix} \begin{pmatrix} \cos(\theta_\lambda) & -\sin(\theta_\lambda) & 0 \\ -\sin(\theta_\lambda) & \cos(\theta_\lambda) & 0 \\ 0 & 0 & 1 \end{pmatrix} \begin{pmatrix} 1 \\ 0 \\ 0 \end{pmatrix} \quad . \tag{3.10}$$

The analysis is then carried forward with the equivalent progression as the Earth albedo neutron case with the appropriate v_r and v_s replacing v_e and v_s in the derivation from the previous chapter. However, we must also calculate the exit angle relative to the ring plane to determine the effective thickness of the production slab. The exit angle,

$$\theta_r = cos^{-1}\left(v_s\begin{bmatrix}1 & 0 & 0\\ 0 & 0 & 0\\ 0 & 0 & 1\end{bmatrix}v_s\right) \tag{3.11}$$

is applied to equation (3.7) to calculate the effective density of the production area. This, in conjunction with the source spectrum through water replaces the albedo neutron spectrum as used in the Earth albedo case.

In addition, trajectories that intersect the planet should be excluded to prevent non-physical injection scenarios. The view angle to the planet is,

$$\phi_{view} = \frac{\pi}{2} - cos^{-1}(L_s)\,. \tag{3.12}$$

In comparison, the angle to the planet's nadir from the ring source is,

$$\phi_{trajectory} = cos^{-1}\left(v_s{}^T\begin{bmatrix}-1\\ 0\\ 0\end{bmatrix}\right). \tag{3.13}$$

If the view angle is greater than the trajectory angle then the particle may intercept the planet when the trajectory is longer than the slant range to the planet. These cases were excluded from subsequent calculations.

MOON/DUST LOSS MODEL

The natural satellites of the Jovian planets absorb trapped radiation belt particles and effectively remove them from the system. These high-energy collisions can also act as a source, though their primary effect on the planet's radiation belt is as a loss mechanism. The loss rate can be estimated with,

$$\left.\frac{df}{dt}\right|_{moons} = f\sum\nolimits_{moons}\frac{A_{moon}}{2\tau_b A_{slot}} \tag{3.14}$$

where τ_b is the bounce period, A_{slot} is the equatorial area covered by the L shell range being considered in phase space, and A_{moon} is the effective moon area which is the cross sectional area for a radius equal to the moons radius plus the gyro radius of the particle being evaluated for that portion of the phase space. The effect of inclined Moon orbits relative to the magnetic field axis is not presently considered. This is a negligible effect for Jupiter and Saturn where the relevant Moons are inclined less than ~10 degrees from the magnetic equator. However, Uranus and Neptune have a large angle between their magnetic fields and the orbital planes of their Moons. As a result, loss rates are over-predicted for high pitch angles where adiabatic particle motion does not reach the Moon. Future models should include a correction factor in equation (3.14) to account for this effect.

The loss rates from extended gas and dust regions in the magnetosphere are also not explicitly included in the current model. A preliminary analysis suggests these do not play a major role since their characteristic time scales are significantly longer than their removal rates due to radial transport. For example, the annihilation loss timescale is over 10^4 years for a 100 MeV proton trapped in Saturn's E-ring (10^{-3} m^{-3} ice particles with a mean radius of 1.2 μm). In comparison, transport timescales are typically a year or less for Saturn's magnetosphere.

DIFFUSION RATE ESTIMATES

The diffusive transport of the trapped particles is a major driver in determining the intensity of the radiation belt. Slow transport leads to long residence times where a large flux can build up to produce intense antiproton fluxes. Table (3.3) shows the diffusion coefficients used in each radiation belt model. The Earth exhibits behavior that scales as L^9, which is the characteristic of transport due to solar induced fluctuations. In comparison, data from all of the Jovian planets shows they follow a $L^{3\pm1}$ radial dependence which appears to be more consistent with plasma interactions in the ambient medium. The electric and magnetic field perturbations that dominate radial transport at Earth appear to be negligible in Jovian magnetospheres.

Planet	**Diffusion Constant (DLL)**	**Reference**
Earth	$3.75\times10^{-12} L^9 \sin^{2.7}\alpha_0 \left(\frac{1MeV}{E}\right) \sec^{-1}$	Jentsch, 1981
Jupiter	$2 \times 10^{-9} L^{2.5} \sec^{-1}$	Goertz et al., 1983
Saturn	$1 \times 10^{-9} L^{3} \sec^{-1}$	Hood, 1983
Uranus/Neptune	$1.6 \times 10^{-10} L^{4} \sec^{-1}$	Cheng, 1987; Gubar 2001

Table 3.3 – Radial diffusion coefficients for different planets.

RADIATION BELT MODEL RESULTS

The radiation belts of each of the planets that can sustain a magnetosphere were completed to determine the relative abundance of antiprotons surrounding each. The model is consistent with the Earth model but includes the modified source, loss, and transport terms discussed above. The albedo source spectrum is very similar but also includes rigidity cutoff effects that can play a major role in the Jovian magnetic fields. Saturn also includes the ring source, which has no comparable analogy in the Earth system.

SATURN

The radiation belt model for the Earth was modified to include the relevant parameters for the Saturn system with the most notable change being the addition of the ring model. The rings act as the dominate source of injected antiprotons in the magnetosphere since they offer the ideal pass thru target for pair production. Antiprotons, antineutrons along with a variety of other particles are generated via GCR interactions with the rings. Past studies have investigated this as the source of protons in the magnetosphere. (Cooper, 1983) The pair produced antiprotons are quickly reabsorbed by the rings since they are trapped on the field lines where they were generated. However, generated antineutrons can move across field lines and decay within a viable trapping region to form the ring equivalent of the CRAND source. The antineutron generation efficiency is very high since the density thickness of the rings are near the optimal depth (~ nuclear cross section) to promote production and do not have to be backscattered to enter the trapping region.

Figure (3.7) shows the estimated integral flux of Saturn's magnetosphere. A total of 10 micrograms per year are injected via atmospheric albedo antineutron decay while about 230 micrograms per year are injected from the decay of antineutrons generated in the ring system. Ring based antineutron production generates trapped antiprotons with a broader high-energy portion of the spectrum relative to the albedo atmosphere source. However, diffusive transport rates from plasma interactions are high which yields a relatively short mean residence time in the magnetosphere. In addition, the rings absorb trapped fluxes at low L-shells where the highest fluxes are typically found. In total, a steady state supply of 10 micrograms is predicted with a peak equatorial flux of ~70 $m^{-2}s^{-1}$ between the orbits of Janus and Mimas. This is still very large and the high replenishment rate makes Saturn the ideal location for extracting large quantities of antiprotons.

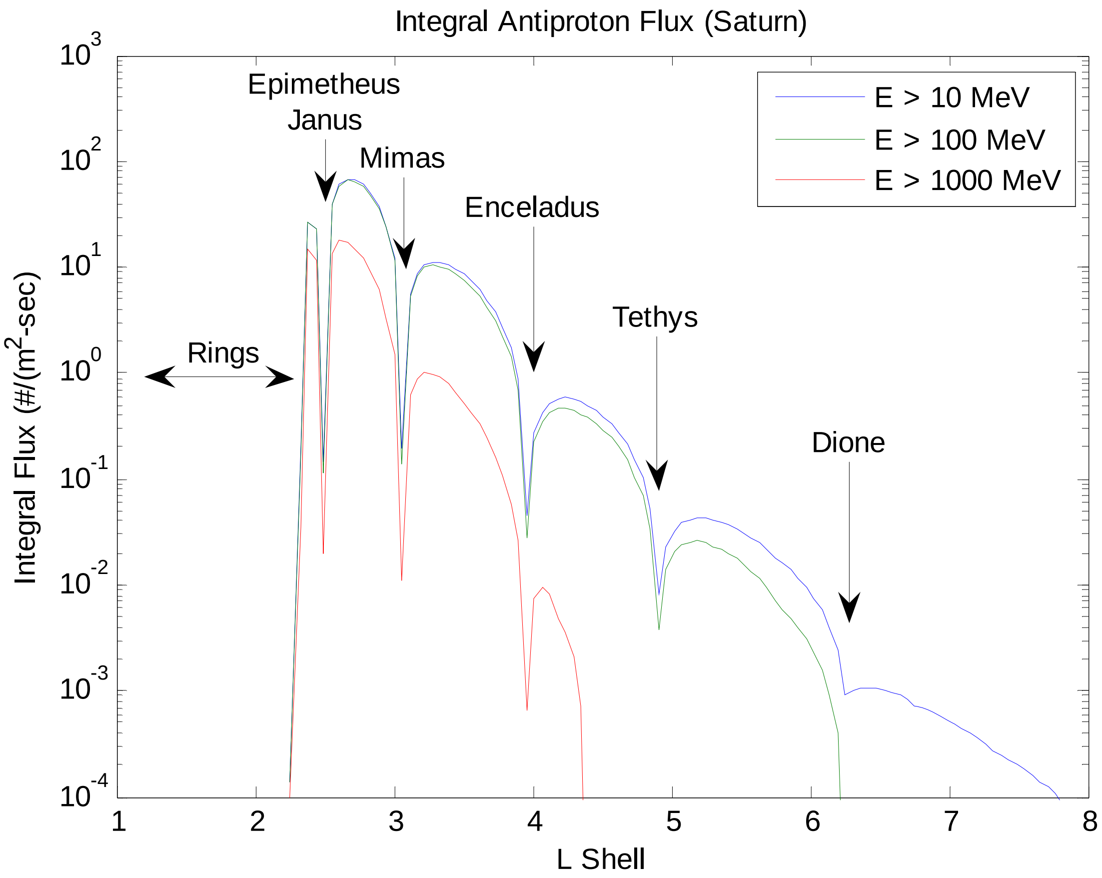

Figure 3.7 – Saturn's equatorial antiproton flux.

JUPITER

Jupiter has the largest magnetosphere of any planet in the solar system. There is also a ring system though it is very tenuous and does not contribute to antiproton production like the rings of Saturn. The strong magnetosphere partially shields the atmosphere from the GCR spectrum, which reduces albedo antineutron production in the atmosphere. However, the sheer size of the magnetosphere and its ability to trap high-energy antiprotons provides a tremendous volume for collecting antiprotons. A total of 7 micrograms per year are injected into Jupiter's trapping region to yield a maximum flux of 10 $m^{-2}s^{-1}$ and a quasi steady state supply of 6 micrograms. Figure (3.8) shows the resulting equatorial flux.

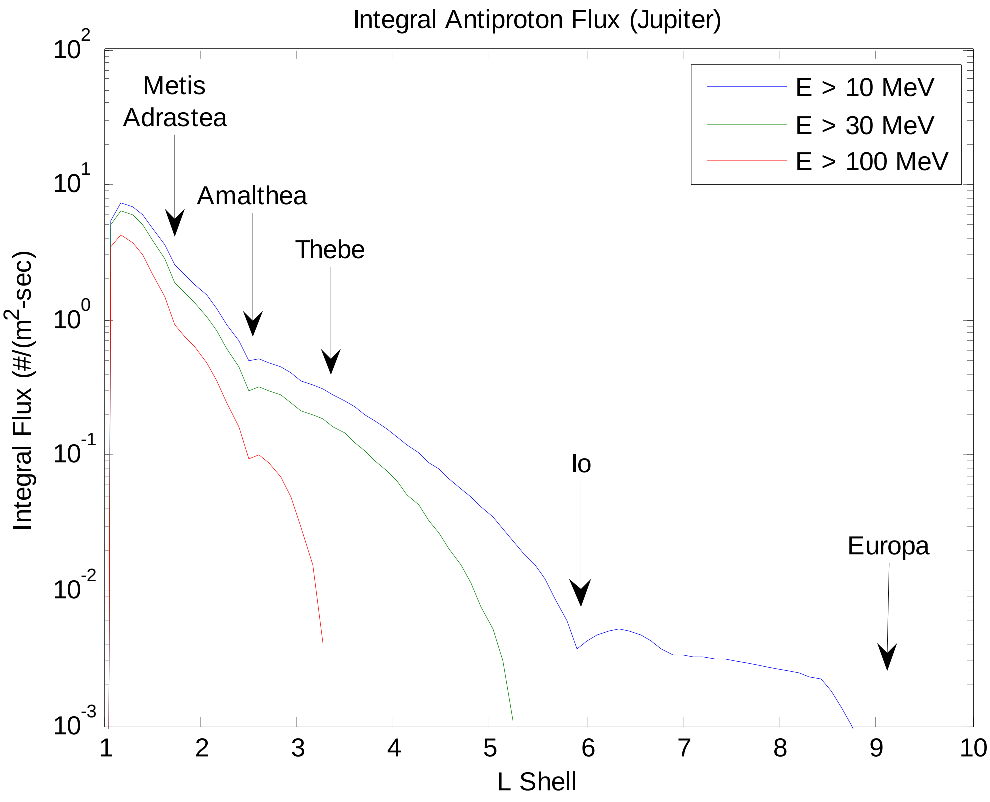

Figure 3.8 – Jupiter's equatorial antiproton flux.

URANUS AND NEPTUNE

Figures (3.9) and (3.10) show preliminary results of simulations of the magnetospheres of Uranus and Neptune. Their magnetospheres are substantially smaller than that of Jupiter and Saturn but are still able to trap between 1 and 2 micrograms of antiprotons with a resupply rate approaching 1 microgram per year. The fluxes are also relatively high though this is very dependent on the rate of radial diffusion, which is somewhat uncertain. The ε ring of Uranus is relatively substantial but spans only a small area relative to the rings of Saturn and therefore plays a minor role as a source. It also acts as a loss mechanism similar to the surrounding Moons as shown. The influence of the many moons is clear though somewhat overstated due to their inclined orbits relative to the magnetosphere. The local reduction in flux due to the Moons would probably be reduced by about 50% if a full accounting of the Moon orbits were included. A future analysis should include these additional effects though the preliminary analysis shown still provides a guide to the structure and intensity of the antiproton belt surrounding these planets.

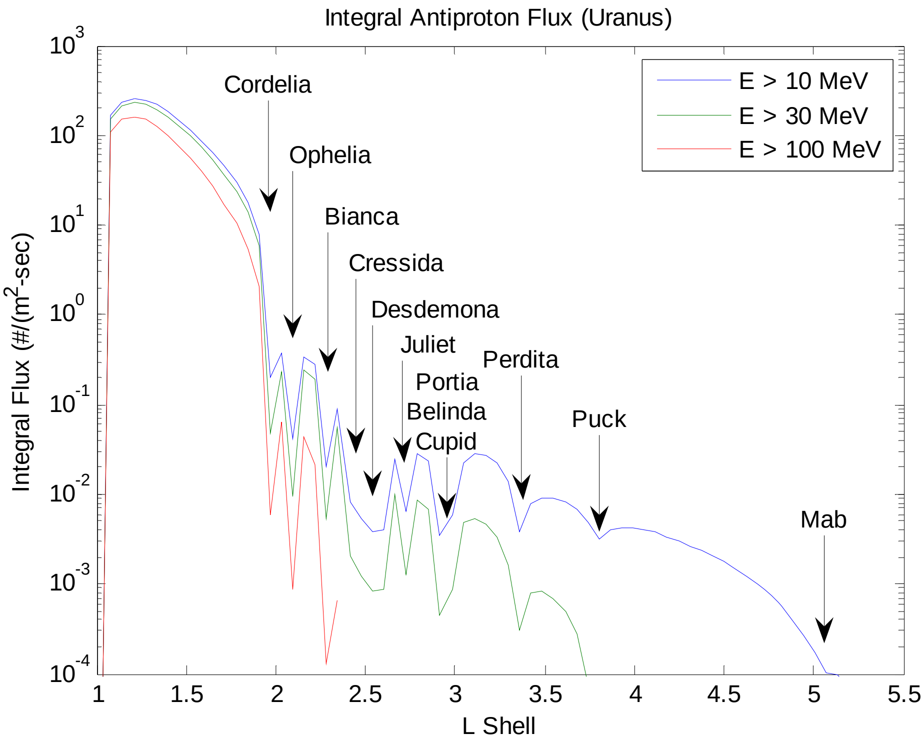

Figure 3.9 – Uranus' equatorial antiproton flux.

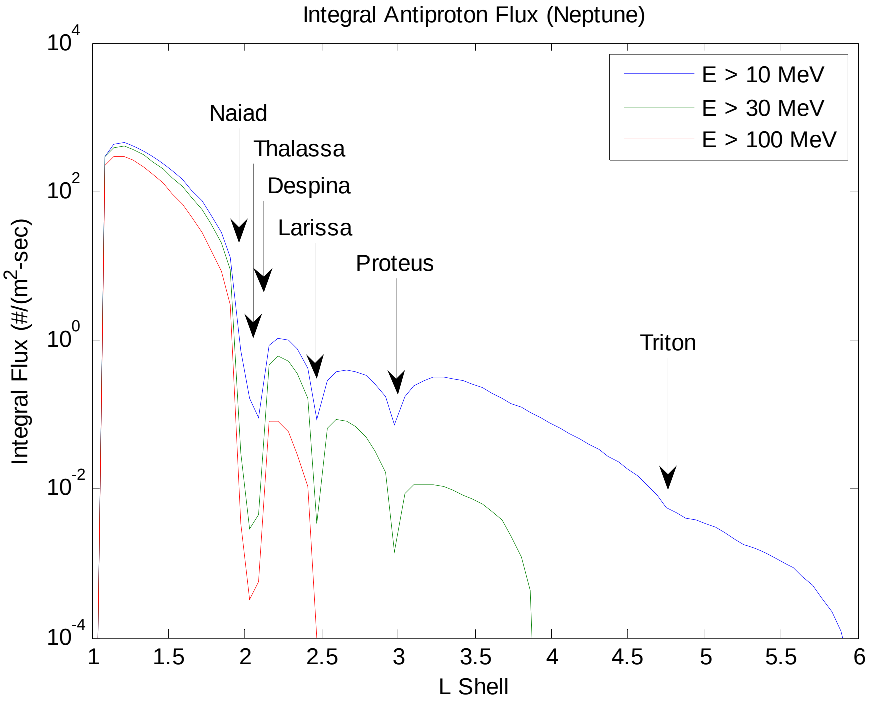

Figure 3.10 – Neptune's equatorial antiproton flux.

DISCUSSION

Though each radiation belt is governed by a common set of physics, the structure of each planet's magnetosphere is clearly unique. Figure (3.11) shows an overlay of the integral flux for each planet with a significant magnetic field. In comparison, the background GCR antiproton flux is about 3 $m^{-2}s^{-1}$. The local fluxes around the planets can exceed this by up to three orders of magnitude. The relative scale of each system is the most obvious change from one system to another with Jupiter clearly dominating in terms of trapped volume. Despite the fact that the total trapped antiproton mass is relatively large, the maximum flux is only marginally larger than the GCR background due to the large volume through which it is distributed.

Uranus and Neptune are the most closely related with the only major difference being the loss rates due to the different Moon configurations. The influence of the many Moons surrounding all the Jovian planets is clearly seen though losses at Jupiter are smallest since the strong field tightens the gyro radius to reduce the effective diameter of each Moon relative to what might be expected in lower field regions.

The low diffusive transport rate around Earth generates very long residence times in the magnetosphere. As a result, the highest flux of antiprotons in our solar system is in our own magnetosphere. However, the relatively small magnetosphere and surface area for production means that the total supply and replenishment rate is low compared to the Jovian planets. In comparison, the rings of Saturn make Saturn the best source of antiprotons in the solar system. The rings keep fluxes at low L shells from forming, though the injected flux at higher L shells makes up for the loss of the high inner zone fluxes found at the other planets.

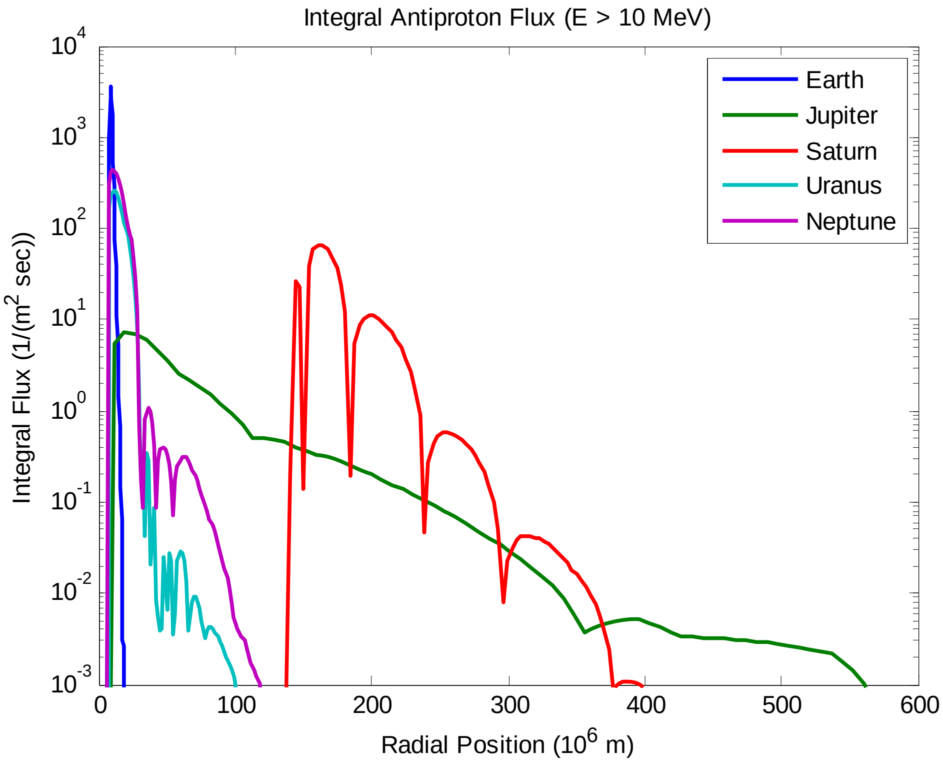

Figure 3.11 – Comparison of the antiproton radiation belts of each planet.

GALACTIC COSMIC RAY FLUX

The galactic cosmic ray (GCR) background includes a significant flux of antiprotons generated by the interaction of particles in the interstellar medium. As shown in figure (4.1), the spectrum has a distinctive peak at 2 GeV. In total, approximately three (3) antiprotons between 1 GeV and 500 GeV will pass through a one square meter plate each second. Though this is extremely tenuous by the standards of radiation belts, the integrated antiproton flux becomes significant over large scales.

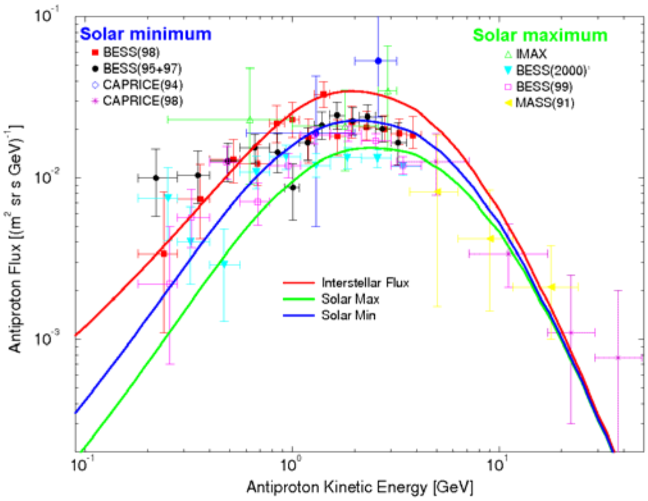

Figure 4.1 – Measured GCR antiproton flux.

Table (4.1) shows the yearly impingement of antiprotons on the inner magnetospheres of the planets. Here we have defined the size of the magnetosphere to be a sphere with a radius equivalent to the approximate sunward side shock boundary where the magnetic pressure balances the solar wind pressure (Kallenrode, 2004). Within this volume around the Earth, a modest 4 grams of antiprotons (1 GeV < E < 10 GeV) pass through on a yearly basis. In comparison, the magnetosphere of Jupiter is the largest structure in our solar system and experiences an integrated flux of over 9 kg of antiprotons per year! Hill (1974) estimated that 10^{-3} of the total incident solar-wind particles are absorbed by the magnetosphere of Earth. This implies that the GCR flux would act as a large antiproton source function for the planets. However, it does not seem likely that this number would carry over to the high-energy GCR flux, especially at the outer planets where solar induced field perturbations are reduced relative to the Earth baseline. The contribution to the overall flux is also unknown but probably small since it is spread over a very large volume and the mean residence time is likely to be short. This should be investigated in more detail during future studies.

Planet	**Standoff Distance** $(2\rho v^2 = B^2/2\mu_0)$	**Antiproton Rate** (1 GeV < E < 10 GeV)	**Yearly Antiproton Impingement** (~inner magnetosphere)
Earth	$11\ R_{earth}$	0.13 μg/sec	0.004 kg
Jupiter	$45\ R_{jupiter}$	287 μg/sec	9.1 kg
Saturn	$20\ R_{saturn}$	41 μg/sec	1.3 kg
Uranus	$26\ R_{uranus}$	12 μg/sec	0.39 kg
Neptune	$25\ R_{neptune}$	10 μg/sec	0.33 kg

Table 4.1 – GCR Antiproton Magnetosphere Impingement

A hint of possible concentration factors is given in the original work by Carl Störmer in the first half of the 20th century (Störmer, 1950). Störmer orbits were calculated by manually integrating the forces on a charged particle to determine the trajectory through a simple magnetic field. He identified specific trajectories based on the particle rigidity and identified the limits of the forbidden regions through which particles of certain energy are not able to pass.

Figure (4.2) shows the results of simulations based on the Earth's magnetosphere interacting with the GCR antiproton flux for particles with an energy of 2 GeV. The plot on the left shows the locations where particles passed through a plane aligned with the magnetic pole of the planet. The Störmer forbidden region (rigidity cutoff) for particles at this energy can clearly be seen in the graph. The plot on the right shows the predicted fluxes of GCR antiprotons. An increase due to the funneling of charged particles along field lines was observed near the poles. This mechanism provides a flux increase of approximately a half order of magnitude relative to the background GCR flux.

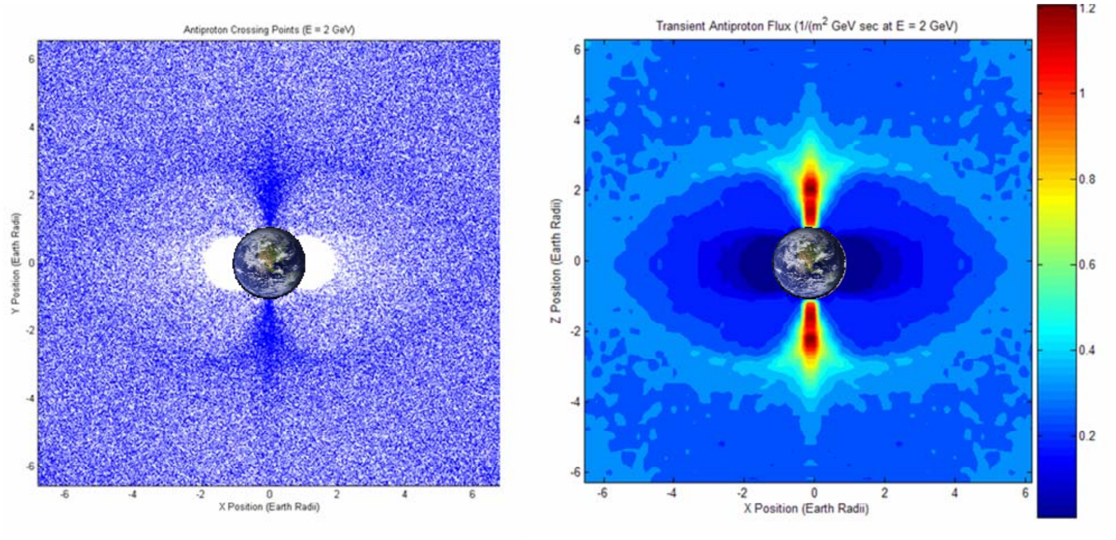

Figure 4.2 – Predicted antiproton flux in the vicinity of the Earth. (E=2 GeV)

Utilizing the higher fluxes of antiprotons near the poles to increase the collection rate can be a challenge due to the required orbital dynamics of spacecraft capable of flying through these regions. Orbits that pass through the high flux zones are restricted to high inclination polar orbits. Unfortunately, a large portion of the orbital period will be spent in the near equatorial regions within the forbidden regions where the background flux is low. If radiation belt antiprotons are also collected, this scenario may become more advantageous. However, the electrodynamics of a magnetic scoop operating in such a field would also be an issue since torque would be applied on a spacecraft in a polar orbit.

Ideally, the collection spacecraft should be placed in a near equatorial orbit for optimal stability and maximum integrated flux intensity. This allows the spacecraft to pass through the radiation belts or to extract portions of the GCR spectrum when orbiting beyond the forbidden regions. The magnetic field of the planet can help in the collection process by biasing the pitch angle of the incident particles. The particles have a tendency to follow field lines as they are deflected by the planet's magnetic field. Therefore, the antiprotons are coming from a restricted portion of the sky, which can greatly assist when collecting the particles via a magnetic scoop. (Chapter 6 & 7)

PAIR PRODUCTION IN COMET TAILS

The tails of comets are a source of material that can interact with the cosmic ray flux to generate antiparticles through pair production. As a comet approaches the Sun, solar heating causes luminous tails stretching for millions of kilometers to form. The solar heating and radiation pressure cause surface volatiles to evaporate and form several distinct tails based on the size and mass of the released particles. (Figure 4.3) An ion trail flows directly away from the Sun while the hydrogen envelope forms another tail slightly offset.

Figure 4.3 – Comet Hale-Bopp showing separated tails.

The dust tail offers a distributed mass of material with which GCR protons can interact to form proton/antiproton pairs. A portion of pair produced antineutrons may also decay which offers a secondary source of antiprotons. A spacecraft flying near the comet could intercept the antiprotons generated from the interaction of the tail with the GCR flux.

A simple spatial distribution model for a comet from Schwadron and Cravens (2000) was used to evaluate the pair production rate. The number density for the non-ionized portion,

$$n = \frac{Q_n}{4\pi \cdot u_n \left(z^2 + b^2\right)} e^{\left(\frac{-\sqrt{z^2+b^2}}{u_n \cdot \tau}\right)} \tag{4.1}$$

is given in cylindrical coordinates where z is the position along the tail and b is the distance from the centerline. Typical values based on comet Levy at 1.25 AU are shown in table (4.2).

Gas production rate	Q_n	10^{29} 1/sec
Outflow speed	u_n	1 km/sec
Ionization time constant	τ	1.6 x 10^6 sec

Table 4.2 – Characteristic values based on Comet Levy at 1.25 AU.

The total mass integrated across the tail is approximately 10^9 kg with a number density of 10^{17} 1/m^3 near the surface. However, the density becomes extremely diffuse further from the nucleus. The total cross is less than 10^{-5} gm/cm^2 both along the tail and across it when integrating both the ionized and non-ionized portion of the distribution. This cross section is very low and is about six orders of magnitude lower than the cross section for GCR protons travelling within our galaxy. Therefore, the net flux of antiprotons will be reduced by approximately this ratio relative to antiprotons in the GCR flux. As a result, the flux of pair produced antiparticles from the tail will not be noticeably larger

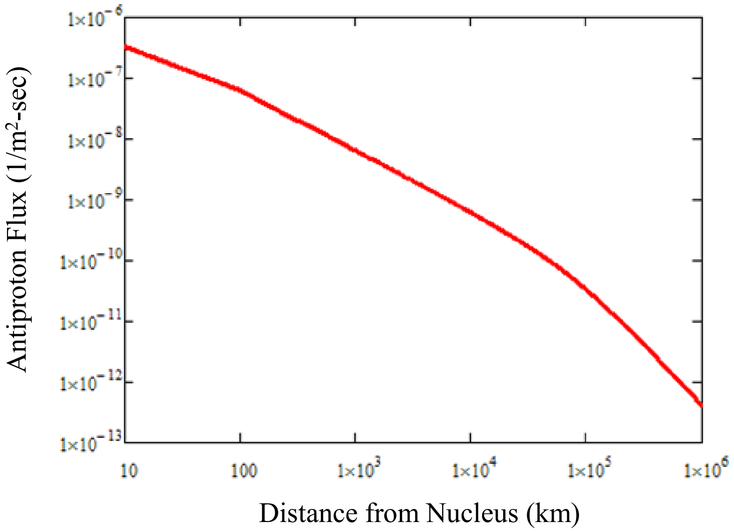

Figure 4.4 – Antiproton flux due to GCR interactions with the tail of a comet.

than the existing background. Figure (4.4) shows the comet portion of the local antiproton flux near a comet based on the production cross section through water.

FLUX IN ATMOSPHERES AND NEAR PLANETARY SURFACES

The atmosphere of planets (e.g. Mars) or Moons (e.g. Titan) can generate antiproton fluxes that can exceed background rates from the GCR antiproton flux. In the case of planets with thick atmospheres such as the Earth and Venus, the peak flux of approximately 40 $1/m^2$-sec occurs at a relatively high altitude (~40 km for Earth) in the atmosphere when the cross section nears the mean free path of antiprotons. Deeper in the atmosphere, annihilations greatly reduce the flux but it remains non-zero even at the surface. However, in the case of Mars, the average atmospheric depth (~65 gm/cm^2) is close to the mean free path, which means the maximum flux will occur near the planet's surface.

On the opposite end of the spectrum, the Earth's Moon has a negligible atmosphere so no additional flux is generated. However, the GCR flux will directly impinge on the surface since there is no appreciable atmosphere or magnetic field to shield it. There may be some residual albedo sputter from the scattering of particles produced from interactions with such an unprotected surface. Asteroids and most other solar system bodies also fall into this category. The efficiency of the scattering process is very low so very few antiparticles are generated. Since these bodies do not have magnetospheres to trap the generated particles, the resulting fluxes around these bodies are negligible compared to the existing GCR background.

GCR/SOLAR INTERACTIONS

High-energy galactic cosmic rays can strike the outer layers of the Sun and generate antiparticle fluxes. The general effects are similar to the Jovian planets where the outer reaches of the solar atmosphere interact with the GCR flux to generate albedo antiparticles. The tremendous area of the Sun enables a large amount of such material to be released. Nearly 10^{17} antineutrons per second leave the immediate vicinity of the Sun yielding a total supply of nearly 6 grams/year. Antiprotons are also released this way though the flux is slightly reduced due to annihilations with protons in the solar atmosphere.

The large area of the Sun makes these numbers somewhat deceiving. Despite nearly ~10 grams/year of antiprotons being produced, the flux near the surface of the Sun is ~0.018 $1/m^2$-sec which is then reduced to about $10^{-6} – 10^{-7}$ $1/m^2$-sec at the orbit of Earth. However, over large spatial scales this is not neglible with 100 ng/yr of the solar induced antiproton flux impinging on the Earth's magnetosphere. Most of the flux will be deflected by the Earth's magnetic field though a small fraction of the protons may diffuse radially inward to lower L shells. Virtually none of the flux reaches below about L=2. Based on an inferred fraction of 10^{-3} incident solar-win particles absorbed by the magnetosphere (Hill, 1974), it is likely that <0.1 ng/yr of solar antiprotons are injected into the Earth's trapping region. However, at higher latitudes, some of the solar produced antiprotons could reach the atmosphere and contribute to the polar aurora.

SPACE BASED ANTIMATTER FACTORIES

The concept of moving the generation process to Earth orbit has also been previously suggested. (Haloulakos and Ayotte, 1991) Space based production has the intrinsic advantage that the generated antiparticles do not have to be transported to orbit from the ground. What is more appealing is the potential to place the generator within the magnetic confinement region. All previous concepts have assumed that the antiprotons would first be generated, then cooled and finally transferred to a storage trap. This cooling and transfer process leads to inherent losses, reducing the total collection efficiency. However, in the case of a planetary magnetosphere or a mini-magnetosphere generated by the magnetic field of a spacecraft, the generator can be placed within the trap. This becomes feasible due to the high vacuum environment in space along with the large volume external trapping provided by the dipole field. Placing the generator in this way enables a significant improvement in the capture efficiency and overall energy efficiency of the process. Table (4.3) shows estimates for this in situ generation process based on the scaling of numbers relative to antiproton generation at CERN and Fermilab.

	CERN	**Fermilab**	**In Situ**
Incident Proton Energy (GeV)	26	120	200
Generation Efficiency (pbar/p)	0.4%	4.7 %	8.5%
Angular Capture Efficiency	20%	30%	100%
Momentum Capture Efficiency	1%	1.2%	85%
Handling Efficiency	5%	18%	80%
Total Efficiency (pbar/p)	4×10^{-7}	3×10^{-5}	0.058
Overall Energy Efficiency	1.4×10^{-9}	2.5×10^{-8}	2.7×10^{-4}
Rate at 100 kWe (Prometheus)			9.5 μg/yr
Rate at 1 GWe			95 mg/yr

Table 4.3 – Antiproton generation efficiency. (Extrapolated from Forward, 1985)

If we take the power available in orbit to be the projected electrical power generated by space nuclear reactors now on the drawing board or a large solar power array, nearly 10 micrograms of antiprotons could be generated and stored per year. This represents a significant quantity of antimatter that could be used for very aggressive space propulsion and exploration. The concept is also quite interesting since additional antiprotons could be generated over the course of the trip during transit to further propel to vehicle. A much larger power source (GWe) could conceivably enable milligram class quantities of antiprotons to be generated. This level of antiproton generation is sufficient to propel small interstellar probes to a significant fraction of c. However, it is not clear how such power levels and the incident particle beam could be easily generated in space. The power output needed is equivalent to one large nuclear or coal power plant and an equivalent particle accelerator on Earth has spatial scales that are typically measured in kilometers. Cleary, a fundamentally new approach has to be taken to tackle these challenges.

Positrons have also been suggested as a propellant for exotic space propulsion concepts. However, the mass requirements tend to be larger since the annihilation reaction provides the primary energy stimulus rather than catalyzing other nuclear reactions as is done in many of the antiproton concepts. Though the flux is far lower than protons in the galactic cosmic ray background, the spectrum also includes electrons, ions and positrons. Measurements of the spectrum have shown that for every 10 electrons there will be one (1) positron incident on the atmosphere. Though the relative ratio of positrons to electrons is relatively high, the overall background mass flux is low. However, of more interest are several recent measurements of positrons produced by the Sun as well as trapped positrons measured in low Earth orbit.

In 1998, the space shuttle flew the AMS-01 magnetic spectrometer as a precursor to the more permanent AMS-02 experiment, which was designed to be installed on the international space station. Interestingly, measurements of the positron and electron background showed that there were approximately four times as many positrons as electrons at an altitude of approximately 380 km (Aguilar, 2002). This appears to be the result of trapping pion decay products generated as cosmic rays and the lower portion of the proton radiation belts interact with the upper atmosphere. (Gusev et al., 2003) A stably trapped positron population coincident with the electron belt should be formed at low magnetic L shells as a result.

Recent measurements from RHESSI (Share, 2003) have shown that positrons can also be produced by the Sun under certain conditions. Though even the largest solar flares on the Sun are not energetic enough to produce antiprotons via pair production, the collision of plasma due to solar flares near the surface provides enough energy to produce positron/electron pairs. It was reported that the annihilation of nearly 1kg was observed after a large solar flare. This measurement was taken by observing the gamma rays produced during positron/electron annihilations near the Sun. However, it is unclear how many, if any of these positrons, are able to escape the production region to travel outwards into the solar system.

We report on the study of positron distributions in the geomagnetosphere. This study is based on knowledge of internal source processes within the magnetosphere, knowledge of sources of positrons that form the (time-dependent) outer boundary of the magnetosphere, empirical knowledge of the transport processes within the magnetosphere (as derived from studies of other particle species), loss processes for positrons via mutual annihilation with electrons, degradation in the positron magnetic moment due to non-annihilation electromagnetic interactions with matter in the Earth's plasmaphere, the neutral exosphere and the upper atmosphere, and energy loss through the emission of synchrotron radiation. Emphasis is also placed on the mathematical technique necessary to solve the steady-state elliptic partial differential equation that governs the physical model. Data on the geospace environment are taken from generally accepted models of the exospheric neutral distributions and the time averaged plasmasphere free electron content.

DESCRIPTIVE COORDINATES

In this work we will describe the average steady-state time-independent distribution of geomagnetically confined positrons in terms of the three free parameters: the relativistic magnetic moment, $M = p^2/2m\gamma B$, which is closely related to the first adiabatic confinement invariant and serves as proxy for kinetic energy, the equatorial pitch angle, α, which helps to parameterize the second confinement adiabatic invariant, and the geomagnetic L-shell parameter, L, which serves as proxy for the third confinement adiabatic invariant. For a description of pertinent magnetospheric physics, the reader is referred to treatises by Roederer (1970), Schulz and Lanzerotti (1974) and others. In terms of these free coordinates, the positron distribution function is represented as,

$$f = f(\alpha, L, M; t) \text{ in units of: } \#/[\text{cm}^3 \text{ sr MeV/Gauss}] \qquad (5.1)$$

where t is time, which we will ignore in the time-independent case.

The standard parameters used in the following are: m_e = positron mass (same as the electron mass) = 9.11×10^{-28} gram, v is positron kinetic velocity, γ = the relativistic factor = $1 / [\,1 - (v/c)^2\,]^{1/2}$, c = speed of light = 2.9979×10^{10} cm/sec, p = positron momentum = γ m v, and B = local magnetic induction (in Gauss). Herein Gaussian cgs-units are used with the exception that energies are more conveniently expressed in MeV-units, where 1 MeV = 1.602×10^{-6} erg.

POSITRON SOURCE TERMS

Positrons can be formed as one of the particles in pair production (positron and electron) from energy in the vicinity of matter, such as an atomic nucleus. In such processes, the threshold kinetic energy would be: $E_{th} = 2\, m_e\, c^2$ + kinetic energy of the generated pair. Positrons can also result from nuclear processes that initially produce positive and negative κ- and π-mesons. Since mesons are unstable, π-mesons decay into μ-mesons, which in turn decay into positrons and electrons. It has been shown that under some conditions positron formation can exceed electron production. (i e., Gusev et al., 2001) Cosmic ray protons impinging on the uppermost atmospheres of the planets in our solar system provide the energy to locally initiate these processes within the planetary magnetic field confinement region.

The cosmic ray fluxes also have small components of antimatter, including positrons, antineutrons and antiprotons. This galactic origin external source partly penetrates the geomagnetosphere (and the magnetosphere of other planets) in to an effective cut-off distance that depends on both the antiparticle energy, direction relative to the planet's magnetic axis, and the strength and average configuration of the magnetic field. Empirically, cosmic rays are generally quite time independent on a human experience scale, except that the low energy cosmic ray component is subject to the well-known Forbush decreases during periods of high sunspot activity when the external part of the sun's magnetic field is extra strong and extensive.

The Sun is a source of antiparticles which is a subject of contemporary research. Unlike the galactic cosmic rays, the sun's emission of particles and antiparticles follows activity in the solar corona and the vicinity of the solar surface, and the associated ejections of solar material impinges on the geomagnetosphere (and the magnetospheres of other planets) often cause geomagnetic storms and other magnetosphere-ionosphere Earth-system disturbances.

Empirically, we know that when the Earth's magnetosphere is disturbed by solar induced magnetic storms tens of times per year where solar energetic particles can be injected much deeper into the geomagnetosphere than at times of a quiescent geomagnetosphere. This has the consequence that solar antimatter can also be efficiently injected during magnetic storms, just as solar matter particles can. This is yet an unexplored antimatter source mechanism for the planets. It remains to be seen how large the solar antimatter emission enhancements are in solar ejection events, and if solar positrons and antiprotons are as effectively enhanced in the Earth's magnetosphere as fluxes of electrons and protons are observed to be.

In contrast to the injection of enhanced solar antimatter fluxes into planetary magnetospheres during magnetic storms, impinging cosmic ray antimatter fluxes are largely not enhanced during magnetic storms, and so do not have the advantageous combination of a weak and disturbed geomagnetic shielding combined with impinging flux enhancements. Thus since geomagnetic storm periods are brief compared with the long periods on non-storm conditions, on the average, galactic cosmic ray effects are largely uncorrelated with magnetic storms.

Drs. Galina Pugacheva and Anatoly Gusev of the IKI facility, Space Research Institute of Russian Academy of Science, Moscow, Russia have computed the outcome of the cosmic ray initiated nuclear cascade leading to the production of positrons in the inner magnetosphere at L=1.2. Their source positron function, expressed in flux-appearance units, dj/dt, of # of positrons / (cm^2 s sr MeV) is presented in figure (5.1)

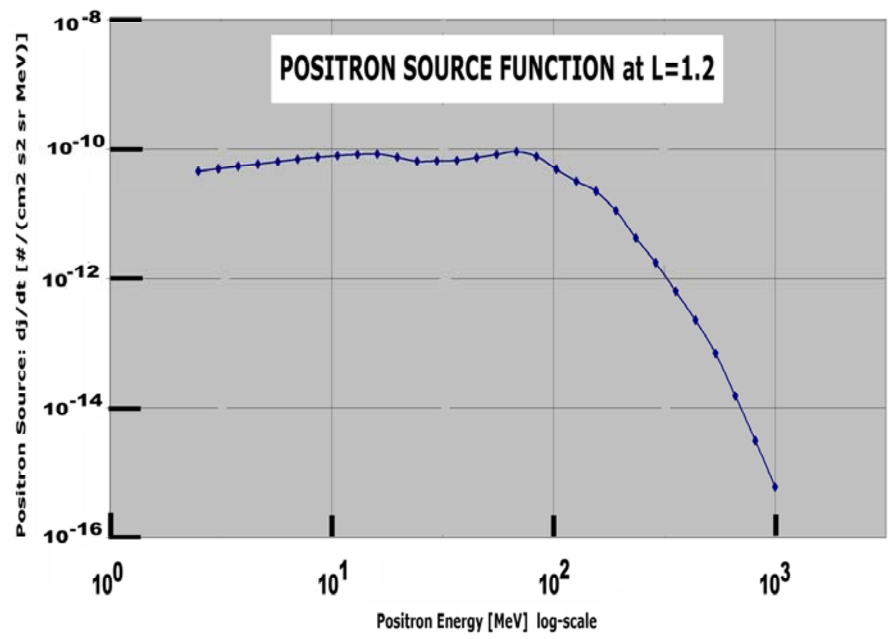

Figure 5.1 – Positron source function at L=1.2.

The width of this inner zone positron source would be quite thin, perhaps effectively just 1/10 L-shell somewhat centered at L=1.2 with likely a steeper fall-off towards lower L-shells, so that at L=1.1 the source might be down by a factor of 10^6. At higher L-shells, the source might fall off less steeply so that at L=1.3 it might be down by a factor of 10^4. And at L=1.4 it might be down by a factor of 10^6 or more.

The angular distribution of the source is likely to be peaked around flat (90 degrees) equatorial pitch angle, and that would be a consequence of the interaction process (radiation belt proton collisions with neutrals), although one might parameterize the source coarsely in terms of a $\sin^N(\alpha)$-distribution with N-values ranging from 0 to perhaps 10 for illustration purposes. It is clear that further investigation of the source process and its distribution in space and angular direction is needed to properly quantify the results.

LOSS AND TRANSPORT PROCESSES

ANNIHILATION LOSSES

Matter ions can charge exchange with other matter particles to become neutral atoms, and so are no longer constrained to follow a magnetic force steering. Such fast neutrals then escape from the magnetospheres of the planets, and this constitutes a near-instantaneous loss of such matter ions. In contrast, antimatter ions do not have a corresponding effective loss mechanism, for there is not an abundance of thermal antimatter with which to exchange charge (no thermal positron supply). Thus unlike protons, antiprotons are not effectively lost by charge exchange.

Magnetospheric electrons are typically lost from the magnetosphere by energy degradation in Coulomb collisions and by scattering in pitch angle by plasma waves (often VLF and ELF turbulence, e.g., Lyons and Thorne, 1973). Trapped positrons are also degraded in energy by (distant) Coulomb interactions, and may also be scattered in pitch angle towards the atmospheric bounce loss cone by some plasma waves. To the best of our knowledge, no study has yet identified the type of plasma waves that might be scattering positrons. Consequently, that aspect cannot here be modeled quantitatively.

Magnetospheric positrons can suffer close encounters with free plasma electrons (in the plasmaphere of the inner magnetosphere), and can interact with bound atomic electrons in the exosphere and upper atmosphere of a planet. For the Earth, these environmental particles include thermal neutral atomic hydrogen, thermal helium, and thermal atomic oxygen. The terrestrial exosphere in the region of the uppermost atmosphere where the atoms execute gravitationally bound ballistic trajectories above the exobase altitude, below which particle collisions are important (as in any dense gas). These close encounters between positrons and neutral atoms can lead to mutual annihilation with an atomic electron, resulting in a pair of gamma rays.

The positron annihilation cross section in interactions with atomic bound electrons is given by Heitler (1954) as:

$$\sigma(Z,\gamma) = [(Z\pi r_e^2)/(\gamma+1)]\ \left\{[\gamma^2+4\gamma+1]/[\gamma^2-1]\ \ln\,[\gamma+(\gamma^2-1)^{1/2}] - [\gamma+3]/[(\gamma^2-1)^{1/2}]\right\} \qquad (5.2)$$

where $r_e = e^2/(m_e c^2) = 2.818 \times 10^{-13}$ cm is the classical value of the electron (and positron) radius, $\gamma = (E_{kin}+E_{rest})/E_{rest}$ is the relativistic factor, and Z is the nuclear charge number of the atom. Thus for the thermal neutral species most abundant in the inner magnetosphere,

$$\sigma_{pH} = \sigma(Z=1,\gamma)\ , \qquad \sigma_{pHe} = \sigma(Z=2,\gamma) \text{ and } \qquad \sigma_{pO} = \sigma(Z=8,\gamma)\ . \qquad (5.3)$$

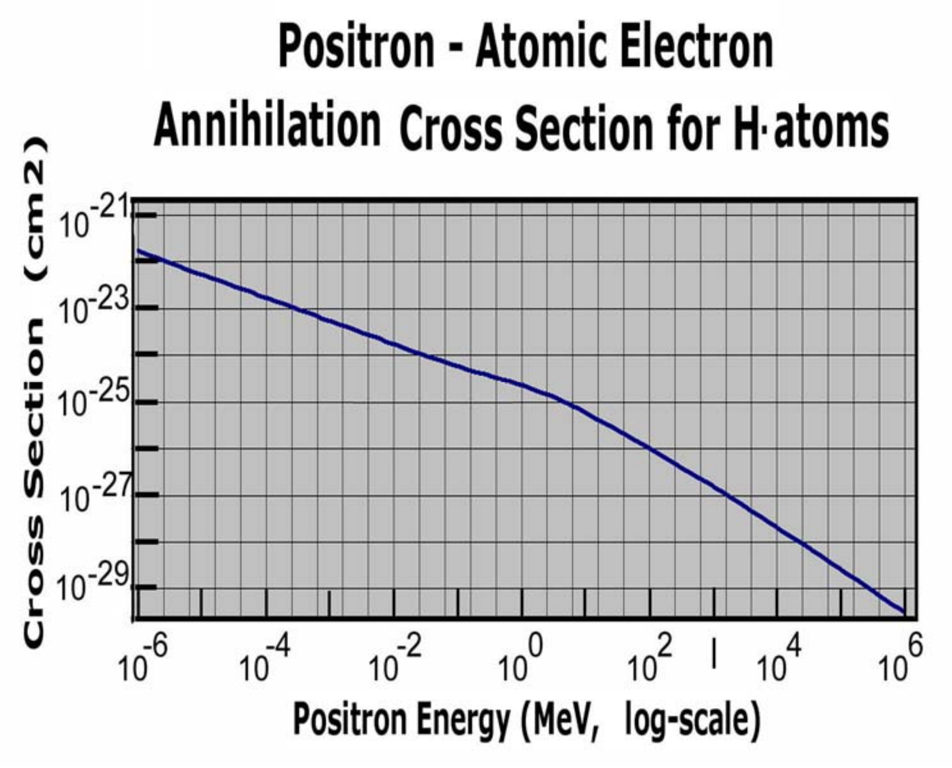

Figure 5.2 – Positron annihilation cross section.

Quantitatively, from annihilation interactions with exospheric atoms, the phase space distribution, f, of positrons is then reduced by the amount:

$$(\partial f/\partial t)_{\mathrm{ANN,atoms}} = [\, \sigma_{pH}\, v\, n_H + \sigma_{pHe}\, v\, n_{He} + \sigma_{pO}\, v\, n_O \,]\, f \qquad (5.4)$$

where v (~c) is the positron velocity, and the (thermal) velocities of the neutral atoms are small enough to approximate them to be v << c, and thus as almost stationary in comparison with the energetic positron velocity. Here n_H, n_{He} and n_O are the number densities (in cm^{-3}) of exospheric neutrals experienced by the positrons. The latter implies an average over the positron bounce trajectory, since the positron experiences a denser material environment near its mirror point (for equatorial pitch angle $\alpha < \pi/2$).

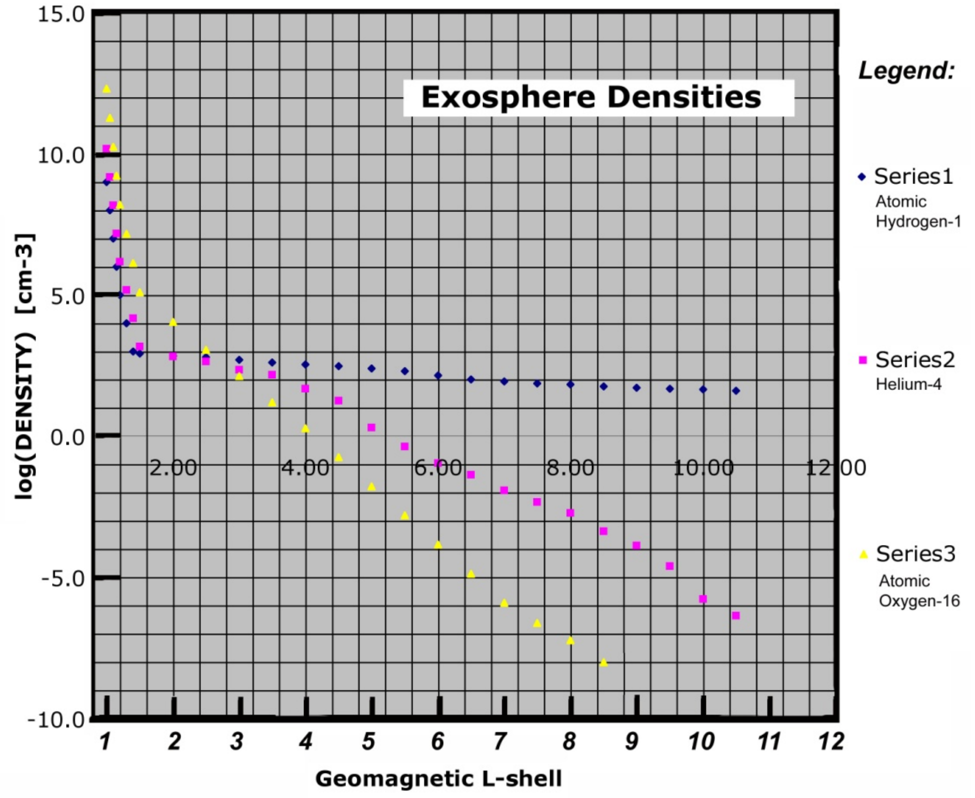

Figure 5.3 – Exosphere density used in positron calculations.

HIGH ENERGY PROCESSES

Positron – free electron mutual annihilation leading to muon-antimuon pair production is described by the cross section,

$$\sigma_{pe} \;=\; (\pi/3) r_m^2 \left\{ \left(E_{thr}/[E_{kin}+E_{rest}]\right) \left(1+[1/2]E_{thr}/[E_{kin}+E_{rest}]\right) \left(1-\, E_{thr}/[E_{kin}+E_{rest}]\right)^{1/2} \right\} \;. \qquad (5.5)$$

The annihilation of positrons and target electrons producing muon pairs in the final state ($e^+e^- \rightarrow \mu^+\mu^-$) may give an appreciable contribution to the total number of muons produced in high-energy electromagnetic cascades.

The threshold positron energy in the laboratory system for this process with the target electron at rest is $E_{thr} = 2m_\mu^2/m_e - m_e \sim 43690$ MeV. Here m_μ and m_e are the muon and electron masses respectively. This implies that positron – free electron mutual annihilation is effective mostly at very high energies in the GeV range. This is visualized in figure (5.5):

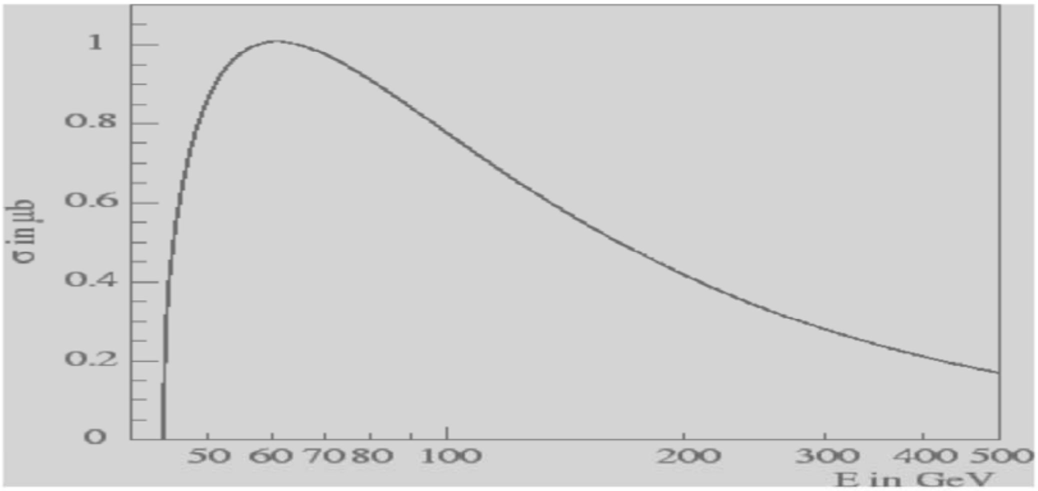

Total cross section for the process $e^+e^- \longrightarrow \mu^+\mu^-$

Figure 5.4 – Muon production cross section.

The cross section as a function of the positron energy is shown in figure (5.2). It has a maximum at $E_{kin}+E_{rest}$ = 1.396 E_{thr} and the value at the maximum is σ_{max} = 0.5426, r_μ^2 = 1.008 microbarn = 1.008 x 10^{-30} cm^2. The annihilation loss term for positron – free electron interaction is then,

$$(\partial f/\partial t)_{ANN,electrons} \;=\; [\, \sigma_{pe}\, v\, n_e \,]\, f \qquad (5.6)$$

where n_e is the number density of free plasmaspheric thermal electrons. the total annihilation term is the sum of these effects so,

$$(\partial f/\partial t)_{ANN} \;=\; [\, \sigma_{pH}\, v\, n_H + \sigma_{pHe}\, v\, n_{He} + \sigma_{pO}\, v\, n_O + \sigma_{pe}\, v\, n_e \,]\, f \qquad (5.7)$$

DEGRADATION OF POSITRONS BY COULOMB PROCESSES

Electromagnetic interactions that do not involve annihilation, generally leads to angular scattering of the positrons. Following the treatment in Rossi and Olbert (1970) we write,

$$(\partial f/\partial t)_{COULOMB} \;=\; (df/\partial M)\,(\partial M/\partial E)\,(\partial E\partial t) \qquad (5.8)$$

where M is the positron magnetic moment,

$$M = E_{kin} \sin^2\alpha \,/\, B, \text{ and } E_{kin} = \text{positron kinetic energy and} \qquad (5.9)$$

$$\partial E_{kin}/\partial t = \Sigma_i \,\{4\pi\, Z_i\, r_e^2\, (m_e c^3\, (E_{kin}+E_{rest}) \,/\, [E_{kin}\, (E_{kin} +2\, E_{rest})]^{1/2})\; F(\beta,Z_i)\}\, \int n_i(s)\, ds \;/\; \int ds \qquad (5.10)$$

with

$$F(\beta,Z_i) \;=\; -2.9 + \ln\{\, (\pi^2\, m_e\, c^4) \,/\, [\, (1-\beta^2)\, (I(Z_i))^2 \,]\, \} \qquad (5.11)$$

since for a purely dipolar geomagnetic field, $\partial M/\partial E_{kin} = \sin^2 A / B$ where A=equatorial pitch angle and $\partial M/\partial t = (\partial E_{kin}/\partial t)\,(\partial M/\partial E_{kin})$ for the Coulomb interaction process.

RADIAL TRANSPORT OF MAGNETICALLY CONFINED POSITRONS

Positrons in the magnetosphere behave in most regards like electrons. Due to their low mass, they can scatter as easily as electrons and respond to fluctuations in the geomagnetic field just like electrons. However, since positrons have positive electric charge they tend to drift around the Earth in the opposite direction compared to electrons of similar kinetic energy. Positrons also gyrate about the geomagnetic field lines in the opposite sense compared to the gyration of electrons. The latter may alter some of the interaction characteristics with magnetospheric plasma waves.

The purely stochastic nature inherent in the radial diffusion process makes the positron radial diffusion characteristics much the same as the radial diffusion characteristics of electrons. Following the research literature (Cornwall, 1972; Spjeldvik, 1979) we have the following expressions for the positron radial diffusion coefficients based on the assumption of a magnetic field power spectrum that statistically follows a ν^{-2} power spectral dependence (with ν being the B-field fluctuation frequency).

The radial diffusion due to geomagnetic fluctuations is,

$$D_{LL,B} = K_B\, L^{10}\ g(\alpha) \tag{5.12}$$

and the radial diffusion due to geoelectric fluctuations is,

$$D_{LL,E} = K_E\, L^{10}\ g(\alpha)\ /\ [L^4 + (ZM/M_0)^2] \tag{5.13}$$

where $g(\alpha) \sim \sin^5\alpha + (1 - \sin^{10}\alpha)\ /\ 10$ and with the net charge number Z = 1 for positrons, and with M_0 = 1 MeV/Gauss (Cornwall, 1972). In these expressions, the overall coefficient depends on the geomagnetic activity level as parameterized by the geophysics kp-index, such that it may be an order of magnitude larger during magnetic storms and somewhat smaller during very geomagnetically quiescent periods. The values applied here are thought representative as long-term averages,

$$< K_B > = 2.3 \times 10^{-14}\ (\mathrm{Lshell}^2)\ \mathrm{sec}^{-1} \quad \text{and} \quad < K_E > = 1.7 \times 10^{-10}\ (\mathrm{Lshell}^2)\ \mathrm{sec}^{-1} \quad . \tag{5.14}$$

ANGULAR SCATTERING OF POSITRONS WITHIN THE MAGNETIC CONFINEMENT

Positrons are scattered in pitch angle by electromagnetic Coulomb interactions. These are stochastic in nature as small-angle scattering is greatly favored by the Rutherford scattering formula. Coulomb interactions between positrons and plasmaspheric electrons/ions and between positrons and neutrals capable of polarization of the electron bound cloud can also cause significant angular scattering (Rossi and Olbert, 1970). However, the effect is probably most pronounced (in comparison with plasma wave scattering) fairly close to the Earth. A formula for Coulomb scattering of electrically charged particles is nominally,

$$D_{\alpha\alpha}^{(\mathrm{COULOMB})} \ = \ (1/2) <(\Delta\alpha_{\mathrm{COULOMB}})^2> / \ \tau_{\mathrm{C\text{-}SCATTER}} \tag{5.15}$$

where $\tau_{\mathrm{C\text{-}SCATTER}}$ is anticipated to strongly depend on location, pitch angle and magnetic moment of the positrons.

To quantify this, we need to invoke the interaction cross section for scattering. Positrons can be scattered (in pitch angle) by free plasma electrons, by ionized matter, and by bound (atomic, molecular) electrons. Let us first look at positron scattering by atoms. The cross section for scattering into a solid angle element $d\Omega$ (in steradians) can be expressed by,

$$(d\sigma/d\Omega)_{\mathrm{ATOM}} = (d\sigma/d\Omega)_{\mathrm{NUCLEUS}} + (d\sigma/d\Omega)_{\mathrm{ELECTRON}} \tag{5.16}$$

where Rutherford scattering theory (e.g., Rossi and Olbert, 1970; p. 222) yields,

$$(d\sigma/d\Omega)_{\mathrm{NUCLEUS}}\, d\Omega = (4 / \phi^4)\, Z^2 Z_t^2\, r_e^2\, [\, m_0 c /(p\beta)\,]^2\, d\Omega \tag{5.17}$$

$$(d\sigma/d\Omega)_{\mathrm{ELECTRON}}\, d\Omega = (4 / \phi^4)\, Z^2 Z_t\, r_e^2\, [\, m_0 c / (p\beta)\,]^2\, d\Omega \tag{5.18}$$

with ϕ being the angle away from the positron's initial forward direction.

It is clear that these expressions greatly favor small-angle ($\phi << 1$ rad) scattering, and thus the scattering effect is via many encounters, and so stochastic in nature: a diffusion phenomenon in angular space. Following Rossi and Olbert (1970) we further have an approximation for the stochastically effective scattering cross section,

$$\xi\, (K) = 8\, \pi\, Z^2 Z_t^2\, [m_0 c/(p\beta)]^2\, r_e^2\, \mathit{ln}[200\, Z_t^{-1/2}] \quad . \tag{5.19}$$

for atoms heavier than hydrogen. This implies a characteristic nuclear scattering frequency,

$$\begin{aligned}\nu_{\mathrm{NUCLEAR\_SCATTER}} &= (1/\tau_{\mathrm{NUCLEAR\_SCATTER}}) \\ &= 8\, \pi\, Z^2 Z_t^2\, [m_0 c/p]^2\, [1/\beta]\, c\, r_e^2 <n_{\mathrm{ATOMS}}> \mathit{ln}[200\, Z_t^{-1/2}]\end{aligned} \tag{5.20}$$

where the bounce-averaged number of (atomic) scattering centers is,

$$<n_{\mathrm{ATOMS}}> = \int n_{\mathrm{ATOMS}}(s)\, ds \;/\; \int ds \tag{5.21}$$

and the characteristic bound electron scattering frequency (inverse time scale) is,

$$\begin{aligned}\nu_{\mathrm{BOUND\_ELECTRON\_SCATTER}} &= (1/\tau_{\mathrm{BOUND\_ELECTRON\_SCATTER}}) \\ &= 8\, \pi\, Z^2 Z_t\, (Z_t + 1)\, [m_0 c/p]^2\, [1/\beta]\, c\, r_e^2 <n_{\mathrm{ATOMS}}> \mathit{ln}[200\, Z_t^{-1/2}]\end{aligned} \tag{5.22}$$

Using these physical approximations, we proceed to estimate the Coulomb scattering based pitch angle diffusion coefficients. We first notice that locally there is no favored dependence on the magnetic field direction in computing these scattering time scales. The only dependence on the equatorial pitch angles of the positrons is in the expression for the observed bounce averaged density of scattering centers. Thus,

$$\tau_{\mathrm{NUCLEAR\_SCATTER}}(\alpha,K) = \beta(K) \,/\, \{8\pi Z^2 Z_t^2\, [m_0 c/p]^2\, c\, r_e^2 <n_{\mathrm{ATOMS}}> \mathit{ln}[200 Z_t^{-1/2}] \tag{5.23}$$

and

$$\tau_{\mathrm{BOUND\_ELECTRON\_SCATTER}}(\alpha,K) = \beta(K) \,/\, \{8\pi Z^2 Z_t(Z_t+1)\, [m_0 c/p]^2\, c\, r_e^2 <n_{\mathrm{ATOMS}}> \mathit{ln}[200 Z_t^{-1/2}] \tag{5.24}$$

where

$$\beta(K)=[K(K+2E_0)]^{1/2}/(K+E_0) \tag{5.25}$$

and

$$r_e = e^2/(4\pi\varepsilon_0 m_0 c^2) = 2.82 \times 10^{-15} \text{ meter} \qquad (5.26)$$

with e being the unit electric charge. Proceeding to the positron pitch angle diffusion coefficients, we define them as the unit mean-square angular spread (in sterradians) per characteristic spreading time,

$$D_{\alpha\alpha}^{(COULOMB)} = (1/2) <(\Delta\alpha)^2> / \tau_{C\_SCATTER}(\alpha,K) \qquad (5.27)$$

with $<(\Delta\alpha)^2> = 1$ and thus,

$$D_{\alpha\alpha}^{(COULOMB)} = 4\pi Z^2 \{Z_t^2 + Z_t (Z_t+1)\} [m_0 c/p]^2 c\, r_e^2 <n_{ATOMS}> \mathit{ln}[200 Z_t^{-1/2}] / \beta \qquad (5.28)$$
$$= 4\pi Z^2 \{Z_t^2 + Z_t (Z_t+1)\} [m_0 c/p]^2 c\, r_e^2 <n_{ATOMS}> \mathit{ln}[200 Z_t^{-1/2}] * (K+E_0) / \{[K(K+2E_0)]^{1/2}$$

As noted above, no specific study of magnetospheric plasma wave interactions with positrons are known to us. It is known that electrons are efficiently scattered by VLF and ELF turbulence, especially within the bounds of the Earth's plasmasphere. The somewhat complicated theory for resonant electron scattering by Landau and cyclotron resonance is detailed in Lyons et al. (1972) and in Lyons and Thorne (1972). It seems likely that positrons may well also be scattered by plasma waves, although the sense of positron gyration is opposite to that of electrons, so the interaction may differ somewhat from the electron scattering. In simulation, positron scattering can either be ignored, it may be parameterized in an ad-hoc fashion, or it may be included with the same efficiency as for the resonant electron scattering. We have taken the former approach: $D_{WAVE} \sim 0$, although extension to include scattering is well within the scope of the simulation technique developed herein.

BOUNDARY OF THE CONFINEMENT REGION

In many earlier works on electrons and protons trapped in the Earth's magnetic field, a fixed outer boundary at L=7 (or L=6.6) has been taken. Strictly, there is a geomagnetic cut-off that is energy- (more precisely, magnetic moment) dependent, and thus the outer boundary really should be different for different magnetic moment particles. This also applies to antiparticles. However, this boundary is also dependent an on instantaneous geomagnetic field topology, so the precise details remain a bit difficult to model accurately. The approach taken here is to use the average time dependent situation.

If the refinement of boundary condition for cosmic ray positrons is used, then we can apply the classical Alfven stability limit by imposing the condition that,

$$n = \rho_{Particle} / \rho_{MagnField} << 1 \qquad (5.29)$$

Here $\rho_{Particle}$ is the particle gyro-radius averaged over a gyro-loop, and $\rho_{MagnField}$ is the characteristic local inhomogeneity scale length of the magnetic field, B. Nominally Alfven set $n \sim 0.05$. From single particle kinetics one computes

$$\rho_{Particle} = p / (qB/c) = R / (B/c) \quad \text{…. in Gaussian cgs-units} \qquad (5.30)$$

Unit charge **e** = $1.60217733 \times 10^{-19}$ Coulomb (SI-unit)
= $4.80653199 \times 10^{-10}$ StatColulomb (Gaussian cgs-unit)

where $p = \gamma m_0 v$ = relativistic momentum, **$q = \pm e$** is particle net charge for singly charged particles, **m_0** is the particle rest mass and **v** is the particle speed. Also R = p / q is the particle's magnetic rigidity. The particle rest energy is then $E_{REST} = m_0c^2$**.**
The characteristic scale length for spatial variation in a magnetic field we estimate as,

$$\rho_{MagnField} = |B| \ / \ |\mathrm{grad}\ B|. \tag{5.31}$$

In the pure dipole approximation to the geomagnetic field, we have,

$$|B|=B_{Earth}L^{-3}[4\text{-}3\cos^2\lambda]^{1/2} \ / \ \cos^6\lambda \tag{5.32}$$

where λ is magnetic latitude (λ=0 at the magnetic equator), and $L=R/R_{Earth}$ is dipole L-shell parameter, such that for the dipolar magnetic field lines,

$$r=LR_{Earth}\cos^2\lambda \tag{5.33}$$

with r being radial distance from the dipole center to a field point at the magnetic equator, and so L = R/R_{Earth} at the equator where λ=0. Here R_{Earth} = 6371 km = 6.371 x 10^8 cm, and the geomagnetic field induction on the Earth's surface ($r=R_{Earth}$) on the equator (where L=1, λ=0) is B_{Earth} = 0.312 Gauss. Limiting the analysis to the geomagnetic equator (λ=0), we have,

$$\begin{aligned}\rho_{MagField} &\sim |\ B\ |\ /\ |\ \mathrm{grad}\ B\ | \\ &= |\ B_{Earth}\ L\text{-}3\ |\ /\ |\ \partial/\partial r\ [B_{Earth}\ L\text{-}3]\ | \\ &= |\ B_{Earth}\ L\text{-}3\ |\ /\ |\ \partial/\partial(LR_{Earth})\ [B_{Earth}\ L\text{-}3]\ | \\ &= |\ B_{Earth}\ L\text{-}3\ |\ /\ \{\ 3\ (B_{Earth}/R_{Earth})\ L\text{-}4\ \} \\ &= (1/3)\ L\ R_{Earth}\end{aligned} \tag{5.34}$$

As noted, the criterion for stable trapping is,

$$n = \rho_{Particle} \ / \ \rho_{MagnField} << 1 \tag{5.35}$$

which implies that,

$$n = [\gamma\ m_0\, v\ c \ / \ (q\ B_{Earth}\ L^{-3})] \ / \ \ (1/3)\ L\ R_{Earth} \tag{5.36}$$

for the equatorial region: **λ**=0. Working this a little further yields,

$$n = [\ (3\ \gamma\ m_0\, v\ c\ L^2)/\ (q\ B_{Earth}\ R_{Earth}\ )] << 1 \quad . \tag{5.37}$$

By assigning a reasonable value to n, say n=0.05, one can define a "critical" trapping or confinement limit **L**-shell associated with that **n**-value,

$$n = [\ (3\ \gamma\ m_0\, v\ c\ _{Lcrit}{}^2)/\ (q\ B_{Earth}\ R_{Earth}\ )] << 1 \ . \tag{5.38}$$

We now seek an expression for γv in terms of the particle kinetic energy, E_{KIN} (in MeV), and so we play with relativistic formulae,

$$\gamma v = v \ / \ [1 - v^2/c^2]^{1/2} \tag{5.39}$$

where c=2.9979 x 10^{10} cm/sec is the speed of light in vacuum. We set,

$$\gamma = E_{TOT} / E_{REST} = (E_{KIN} + E_{REST}) / E_{REST} \qquad (5.40)$$

where $E_{REST} = m_0c^2$ and also

$$v = c\,[1 - 1/\gamma^2]^{1/2} = c\,[1 - 1/(E_{KIN} + E_{REST}) / E_{REST}\,\gamma^2]^{1/2}. \qquad (5.41)$$

Putting this together yields,

$$\begin{aligned} \gamma v &= v / [1 - v^2/c^2]^{1/2} \\ &= c\,[1 - 1/ \{(E_{KIN} + E_{REST}) / E_{REST}\}^2]^{1/2}\,(E_{KIN} + E_{REST})/ E_{REST} \qquad (5.42) \\ &= c\,[E_{KIN}^2 + 2\,E_{KIN}\,E_{REST}]^{1/2} / E_{REST} \\ &= c\,[(E_{KIN}/E_{REST})^2 + 2(E_{KIN}/E_{REST})]^{1/2}\,. \end{aligned}$$

We now insert this intermediary result into our expression for n,

$$n = [3m_0L_{crit}^2c^2/(qB_{Earth}R_{Earth})]\,[(E_{KIN}/E_{REST})^2 + 2(E_{KIN}/E_{REST})]^{1/2} << 1. \qquad (5.43)$$

Fixing a value for n (say, Alfven's original estimator: $n \sim 0.05$), we can solve for the maximum L-value for particle stability as a function of the particle's kinetic energy E_{KIN} (in MeV),

$$L_{CRIT} = \{(n\,q\,B_{Earth}\,R_{Earth})/(\,3m_0c^2)\,[(E_{KIN}/E_{REST})^2 + 2(E_{KIN}/E_{REST})]^{-1/2}\}^{1/2}\ . \qquad (5.44)$$

This is the "critical **L**-shell" in Gaussian cgs-units within which the particle is stably trapped (in the adiabatic theory sense), and outside of which the particle is likely to wander chaotically, eventually to get lost from the trapping region. Figure (5.5) shows L_{CRIT} versus E_{KIN} for electrons (same for positrons) and for protons (same for antiprotons).

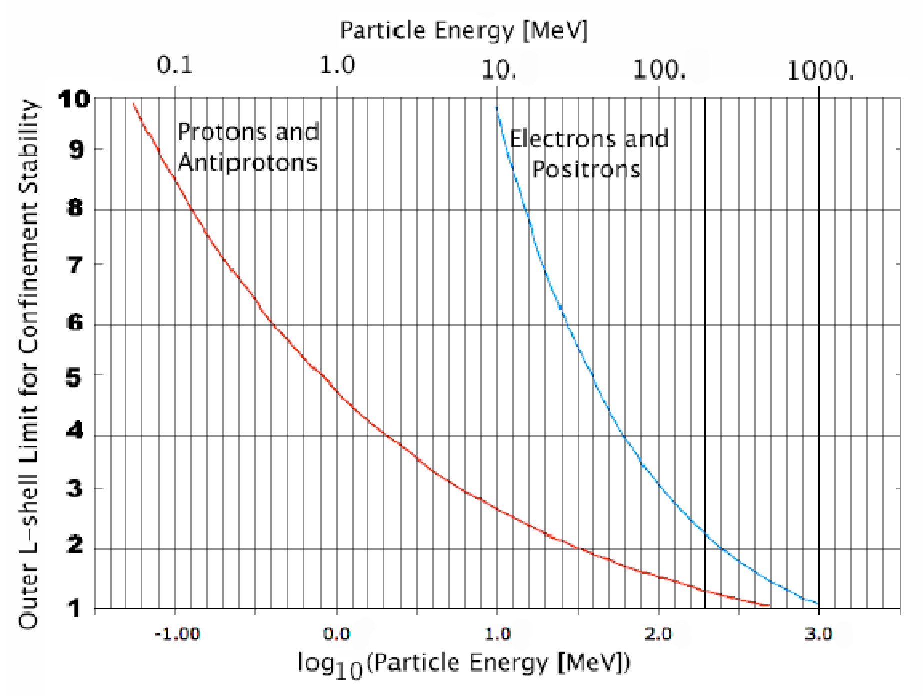

Figure 5.5 – L shell stability limits.

Vice verse, particles from the outside have little chance of penetrating the geomagnetic field farther in that to this L-shell. So this is a rough delimiter between stably confined particle fluxes at $L < L_{CRIT}$. And so L_{CRIT} would serve as a coarse delimiter of how far into the geomagnetic field an energetic particle can come. Of course, there is a region around L_{CRIT} where the particle orbits are quite complicated, as a transition between trapping confinement at lower L-values and directly open orbits to/from outer space at higher L-values. If precise knowledge of such orbits should be desired, then numerical orbit tracing in this transition domain would be necessary.

In practical usage, the geomagnetic field differs from a dipole in several respects, and values of L_{CRIT} beyond $L_{CRIT} \sim 10$ are not meaningful since the geomagnetic field is highly distorted at such distances from the Earth. Furthermore, values of L_{CRIT} below $L_{CRIT} \sim 1$ are not meaningful either since essentially no particles penetrate that far (below the surface of the Earth). In the angular parameter, we have imposed the condition that $\partial f/\partial\alpha = 0$ at $\alpha = 0$ and at $\alpha = \pi/2$.

The boundaries of the magnetic moment dimension are treated as follows: We extend the magnetic moment domain to sufficiently high values at M_{MAX} so that it is a good approximation to impose $f(\alpha,L,M_{MAX}) = 0$. There is no need to impose any condition at M_{MIN} so $f(\alpha,L,M_{MIN})$ becomes a derived result. A dipolar magnetic field can be expressed by:

$$B = (B_{EARTH}\, L^{-3})\, [4 + 3 \cos^2\lambda]^{1/2} / \cos^6\lambda] \qquad (5.45)$$

where for this case $L = R / R_{EARTH}$ and λ = magnetic latitude so that $\lambda = 0$ constitutes the magnetic equator, and $\lambda = \pi/2$ indicates the direction of the magnetic dipole axis. Here $R_{EARTH} \sim 6371$ km is the mean radius of planet Earth.

SIMULATION MODEL OF CONFINED POSITRONS

Following the well-established research literature on transport, source and loss of magnetically confined particles (Nakada and Mead, 1966; Corwall, 1972; Schulz and Lanzerotti, 1974; Spjeldvik, 1979), we write the governing equation for magnetospheric positrons in the form:

$$(\partial f/\partial t) = (\partial f/\partial t)_{SOURCE} + (\partial f/\partial t)_{RAD\text{-}DIFFUSE} + (\partial f/\partial t)_{PA\text{-}SCATTER} + (\partial f/\partial t)_{COULOMB} + (\partial f/\partial t)_{ANNIHILATE} \qquad (5.46)$$

subject to boundary conditions in the outer magnetosphere where a fixed positron energy spectrum is imposed at the appropriate radial distance as expressed by the geomagnetic L-shell parameter, $f(\alpha,L_{MAX},M)$ = fixed. Al the innermost radial distance, here taken as the Earth's surface, we impose the condition of zero phase space distribution function: $f(\alpha,L_{MIN}{=}1,M) = 0$. From the above treatment of the specific parameters, we write:

$$(\partial f/\partial t)_{SOURCE} = \text{numerical source data from Pugacheva and Gusev.} \qquad (5.47)$$

$$(\partial f/\partial t)_{RAD\text{-}DIFFUSE} = L^2\, \partial/\partial L\, [\, L^{-2}\, (D_{LL,B} + D_{LL,E})\, \partial f/\partial L\,] \qquad (5.48)$$

$$(\partial f/\partial t)_{PA\text{-}SCATTER} = [1/h(\alpha)]\, \partial/\partial\alpha\, [\, h(\alpha)\, (D_{COUL} + D_{WAVE})\, \partial f/\partial\alpha\,] \qquad (5.49)$$

$$(\partial f/\partial t)_{COULOMB} = (\partial M/\partial E)\; (\partial E/\partial t)\; df/\partial M \qquad (5.50)$$

$$(\partial f/\partial t)_{ANNIHILATE} = -\, \Lambda\, f \qquad (5.51)$$

Here $h(\alpha) = T(\alpha)\sin(2\alpha)$ and $T(\alpha)$ is the bounce time dependence on the equatorial pitch angle, α. For details, see Roederer (1970) or Schulz and Lanzeotti (1974). Numerical approximations to $T(\alpha)$ have been given by several authors, and a common expression is $T(\alpha) \sim 0.62 + 0.31\sin(\alpha)$.

Equation for the Geomagnetosphere Positron Content:

The above governing equation can be cast in time independent form appropriate for simulating the steady state time independent content of positrons in the geomagnetosphere. We simplify notation by setting:

$$S = (\partial f/\partial t)_{\mathrm{SOURCE}} \tag{5.52}$$

$$D_{LL} = D_{LL,B} + D_{LL,E} \tag{5.53}$$

$$D_{\alpha\alpha} = D_{\mathrm{COUL}} + D_{\mathrm{WAVE}} \tag{5.54}$$

$$\Psi = (\partial M/\partial E)\ (\partial E/\partial t) \tag{5.55}$$

$$\Lambda = (1/f)\ (\partial f/\partial t)_{\mathrm{ANNIHILATE}} \tag{5.56}$$

Thus, we obtain governing transport-source-loss equation cast as the elliptic partial differential equation,

$$S + L^2\,\partial/\partial L\,[\,L^{-2} D_{LL}\,\partial f/\partial L\,] + h^{-1}\,\partial/\partial\alpha\,[\,h\,D_{\alpha\alpha}\,\partial f/\partial\alpha\,] + \Psi\,\partial f/\partial M - \Lambda f = 0\ . \tag{5.57}$$

BASELINE RESULTS

Many numerical methods can be employed. We have here chosen to utilize the accelerated Gauss-Siedel technique in which finite differences as used where derivative expressions occur. Boundary conditions are imposed as fixed (time-independent) values, and values beyond the geomagnetic cut-off boundaries are just the interplanetary average values for the positron function.

The iterative procedure is begun with all unknown values set to unity, and these values are updated as information from nearby grid points become available. In practice, information from the boundaries works itself into the computational domain consistent with the governing equations as outlined in the above description. The solution is considered arrived at when there is no longer an appreciable change (say, within a factor of 10^{-9} of the previous iteration) in all of the grid point values.

Figure (5.6) shows computed positron differential flux between 0.1 and 10,000 MeV/Gauss at L=1.1 through L=2.3 for equatorially mirroring positrons. Figure (5.7) shows the computed positron differential flux between 0.1 and 1,000 MeV at L=1.5 through L=6.5 for equatorially mirroring positrons. Figure (5.8) shows the computed positron differential flux between 0.1 and 1,000 MeV at L=1.1 through L=2.3 shown as radial profiles for equatorially mirroring positrons.

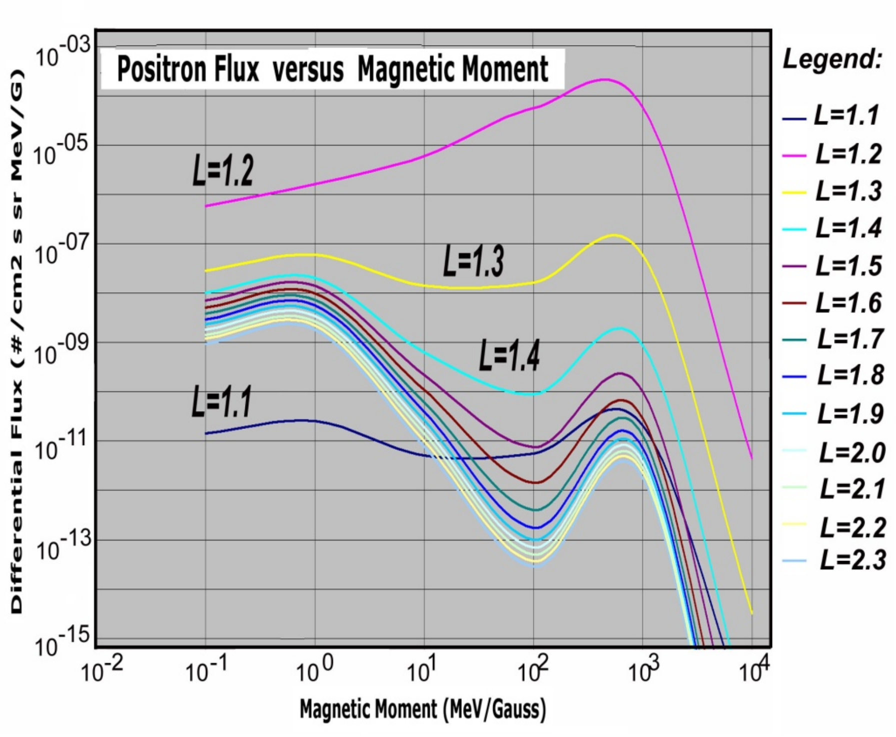

Figure 5.6 – Positron flux versus magnetic moment.

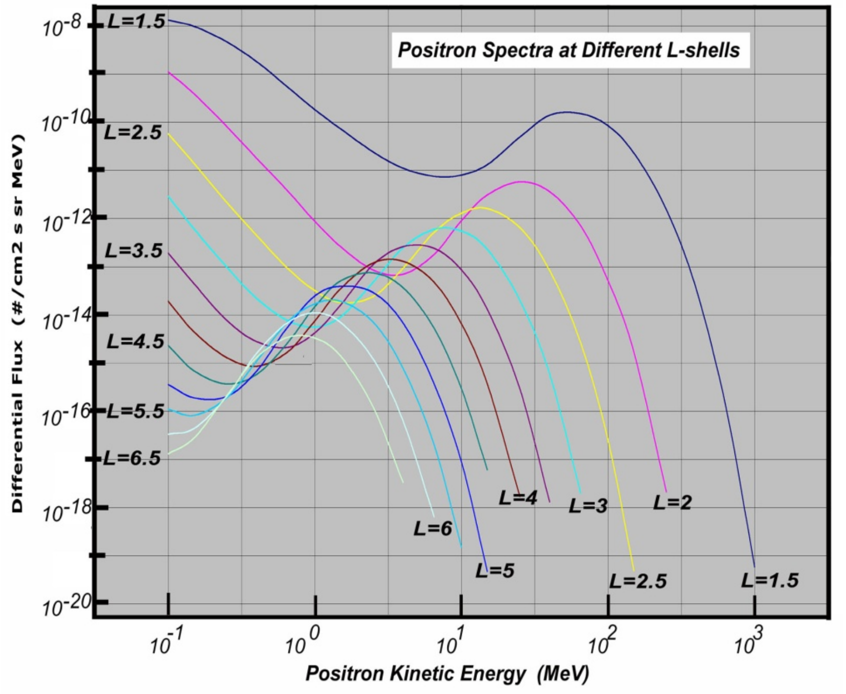

Figure 5.7 – Positron energy spectra for different L-shells.

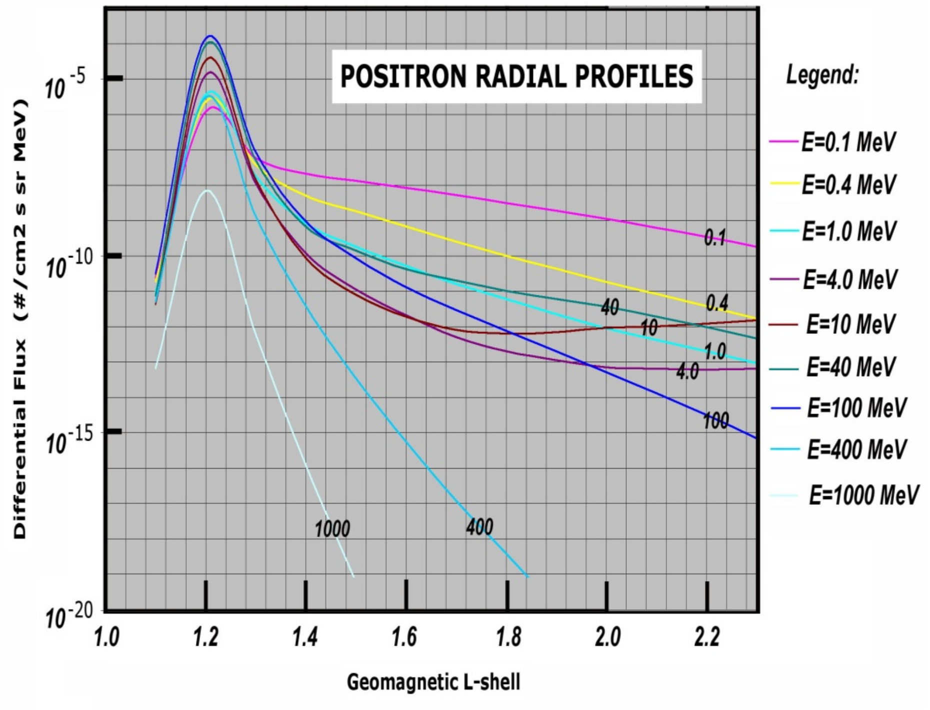

Figure 5.8 – Positron radial distributions for different energies.

GCR SOURCE SCALING

The results shown above are based on a single sharply peaked internal source of positrons, which results from the interaction of the proton belt with the upper atmosphere. However, the estimated fluxes are significantly lower than those measured by the AMS experiment at L~1.06 and low magnetic latitudes. The most likely explanation for this is that there is another internal source of positrons not included in the model. Such a source is likely to be the interaction of cosmic rays with the upper atmosphere.

The effect of the GCR source was evaluated by developing a source function that varied with altitude. To simulate this, the output spectrum from the proton belt interaction was directly scaled by the density profile of the atmosphere along with a constant scale factor to represent the relative production provided from each source. The resulting spectrum was added to the model as an additional source term. The uniform factor used to scale the input was selected by matching the model output to empirical data from the AMS experiment (Aguilar, 2002). A factor of 3 x 10^8 provided the best match to measurements from the 1998 flight. The validity of the scaling is questionable but a more complete investigation is beyond the scope of the current effort. Figure (5.9) shows the resulting integral positron flux based on the assumptions discussed above. Integrating the flux over phase space yields a total trapped positron supply of 0.9 micrograms. However, the predicted flux appears to be higher than the electron flux between L=1.05 and L=1.2 which likely indicates that the scaling relationship is not valid. A more in depth evaluation of all source functions should be completed in the future.

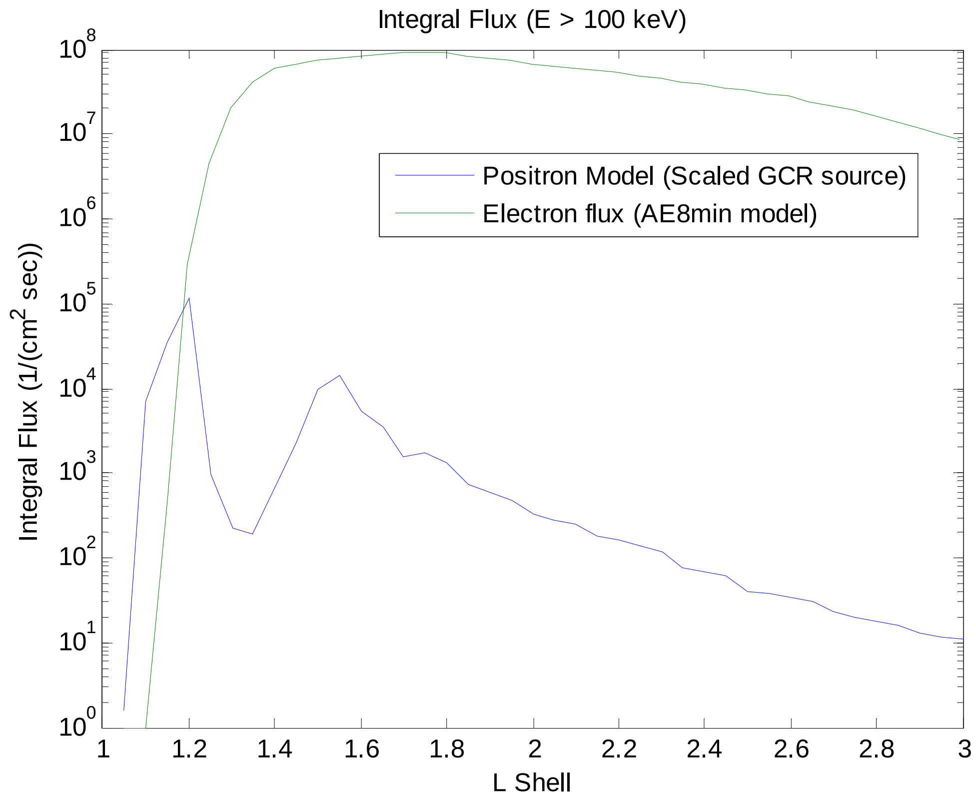

Figure 5.9 – Comparison to electron flux model.

CHAPTER 6 – COLLECTOR MODELING

The results described in previous sections suggest that localized, naturally occurring populations of antimatter can be exploited for a variety of applications including, among others, space propulsion. However, at best these populations occur in concentrations that are orders of magnitude below the storage densities required for operational systems. If we are to take advantage of natural sources of antimatter, we must first develop a means to concentrate these tenuous populations and trap them for extended periods. This chapter will introduce some of the proposed mechanisms for concentrating or focusing incident particle fluxes, as well as the analytical and computational models used to study them. Chapter (7) will assess the performances of prototype systems.

LORENTZ FORCE MOTION

Before we begin, let us review some of the governing physics. The motion of any charged particle through an electromagnetic field is governed by the Lorentz force law,

$$\vec{F} = q(\vec{E} + \vec{v} \times \vec{B})\,. \tag{6.1}$$

A positively charged particle exhibits acceleration in the direction of an applied electric field, and curves perpendicularly around an applied magnetic field according to the right-hand rule. In many cases, it is simpler to express a particle's trajectory as a superposition of a relatively fast circular motion around a particular point referred to as the "guiding center" and a (typically) slower drift of same. In the simplest case of a uniform static magnetic field, absent any other forces or fields, the Lorentz force is perpendicular to the magnetic field and the particle trajectory, resulting in helical trajectories at a constant speed. The gyro- or cyclotron frequency and the gyro- or Larmor radius are, respectively,

$$\omega_c = \frac{qB}{m}; \quad r_L = \frac{v}{\omega_c}\,. \tag{6.2,6.3}$$

The effects of additional fields and forces can be quantified by a general force drift,

$$\vec{v}_f = \frac{1}{q}\frac{\vec{F} \times \vec{B}}{B^2}\,. \tag{6.4}$$

The simplest cases are electric and gravitational fields, for which drift velocities are easily and intuitively derived. For other drifts, such as the so-called "grad-*B*" drift, the responsible force is more complex – say, the force on a magnetic dipole in a gradient. And in many cases, the particle's own acceleration gives rise to "fictitious" forces that account for specific drifts such as the "curvature" and "polarization" drifts. Despite these quirks, an accurate accounting of all forces and their respective drifts results in a complete description of a particle's motion.

PLASMAS

If we wanted simply to influence the motion of a single particle in a vacuum, we could proceed with only the above equations of motion and design any number of relatively simple systems. In practice, most applications will require operation amidst some background population – a planetary atmosphere, a comet tail, or even the solar wind. Our framework is incomplete unless we also include certain bulk effects.

The screening of electric fields, a phenomenon commonly referred to as Debye shielding, places a fundamental limit on the influence of electric fields in plasmas. The presence of free charge carriers allows the plasma to shield local charge imbalances over distances on the order of a few Debye lengths,

$$\lambda_D = \sqrt{\frac{\varepsilon_0 k_B T}{ne^2}}\ . \tag{6.5}$$

For the Earth's magnetosphere and the solar wind, typical values of the Debye length vary from 1~100m. This places an upper bound on system size.

The propagation of electrostatic and electromagnetic waves is also affected, in that the presence of the plasma medium results in a deviation from the vacuum dispersion relation $\omega = ck$. For a given plasma density and temperature, and appropriate dispersion relation, we can define for a given mode the quantity

$$N^2 = \frac{c^2 k^2}{\omega^2}\ , \tag{6.6}$$

analogous to an index of refraction and find that propagation occurs only if $N^2 > 0$. For most wave modes pertinent to this study the above condition is satisfied by oscillations at frequencies greater than the plasma frequency,

$$\omega > \omega_p \equiv \sqrt{\frac{n e^2}{\varepsilon_0 m}}\ . \tag{6.7}$$

DRIFT-LIMITED SYSTEMS

Collection systems that rely solely on the use of static magnetic fields to concentrate an incoming flux of particles are said to be "drift-limited," in that their performance is limited by the drift velocities that they induce. Consider the case of a magnetic field created by a current-carrying loop, as depicted in Figure (6.1). As a particle traces its helical orbit along a field line it will experience a stronger magnetic field as it approaches the center of the loop, resulting in a decreasing gyroradius, until the particle loses all momentum in the direction of its travel and reverses direction. This is known as the grad-*B* drift; the ability of a particle to penetrate near to the center of the system is limited by its kinetic energy, and its orientation with respect to the field line it follows, or pitch angle. The effect of the grad-*B* drift on low-energy particles can be significant – as will be shown in Chapter (7), for a reasonably sized "single-loop" device operating in the Earth's radiation belts very few particles approach within the radius of the device. Instead, most

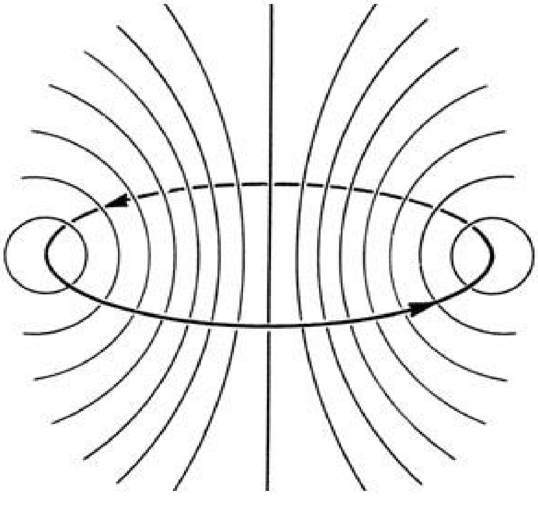

Figure 6.1 – Magnetic field lines of a current loop.

particles are deflected to the surrounding lower-field-strength regions resulting in only marginal focusing over a large volume.

A variant of the single-loop system makes use of not one but, in fact, several circular current loops of radius *r* arranged symmetrically in a circular array of radius *R*. When operated in tandem, the center of the system is by symmetry a low-field-strength region common to all current loops in the system. Figure (6.2) depicts such an "N-loop" system, for N=8. The N-loop approach increases focusing at the center of the device, at the cost of additional power and mass for each additional loop. However, overall efficiency is notably poor for low to moderate values of N; the "gaps" between each loop create relatively low field strength regions through which particles can escape from the moderate-strength central region. Performance is improved by increasing the value of N – more loops decreases the spatial dimensions of each "gap" – until these "escape routes" are closed off, and since system performance is monotonically increasing in N, it is useful to examine the limiting case of $N = \infty$.

It is easy to show that this limit is mathematically equivalent to the case of two concentric loops of radii *R* + *r* and *R* – *r*, carrying equal but opposite currents. The resulting field geometry lends itself to high performance, as the magnetic field strengths near the center of the device are exceptionally low. Further, unlike the N-loop systems that require that each current loop be indistinguishable to maintain symmetry, "concentric loop" systems allow added flexibility in that the radii and currents of both loops are free parameters. Chapter (7) details extensively the performance and optimization of concentric loop systems.

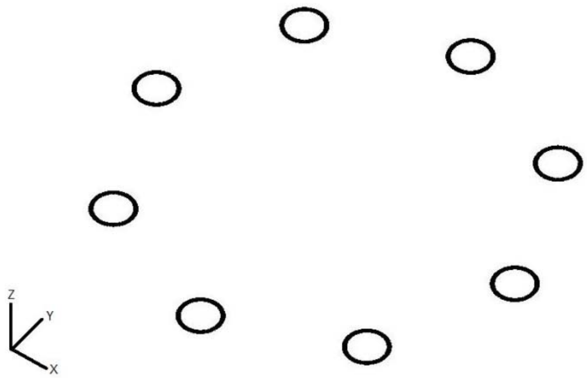

Figure 6.2 – Three-quarter view of an N-loop system, for N = 8.

The above systems exhibit fair performance, however they are exceedingly impractical in that they are designed to provide increasingly shallow gradients – minimizing the effects of the grad-*B* drift – without real regard for mass or power efficiency. Typical single-loop systems, for example, require radii of 1-10km and currents exceeding 10^8A in order to establish a sufficiently large radius of influence to collect from the tenuous GCR source. Recent work has focused on establishing large-scale magnetic fields with minimal infrastructure by using a rotating magnetic field (RMF) to magnetize electrons in a background plasma. For frequencies above the ion cyclotron frequency $\omega_{ci} = eB / m_i$, the response of the ion population to the rotation of the field can be neglected resulting in a net current in the direction of rotation, and thus a net magnetic field symmetric about the axis of rotation. Figure (6.3) (Slough, 2007) depicts the inflation of such a field – the blue field lines represent the RMF attributed to the driver antennae, while the red traces indicate the response of the background electron population. The resulting large-scale field lines are shown in red. The performance and efficiencies of these "Plasma Magnet" systems are analyzed extensively in Chapter (7).

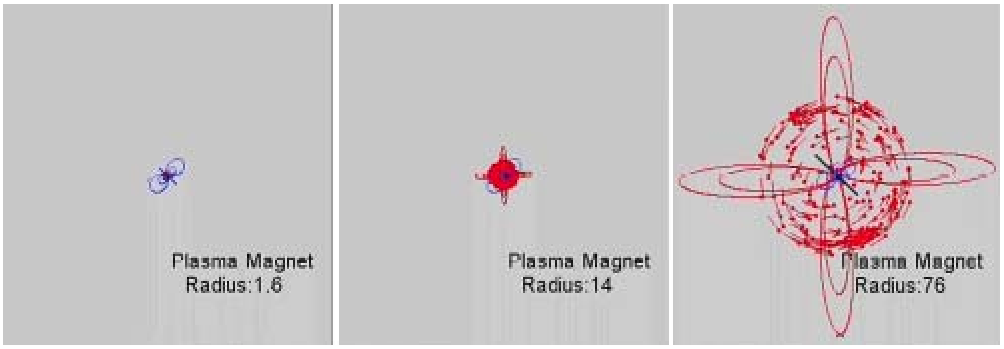

Figure 6.3 – Plasma magnet field inflation (Slough, 2007).

DEBYE-LIMITED SYSTEMS

The ability of a plasma to screen electric fields places a fundamental limit on the efficiency of systems that rely on electric potential gradients to focus incident particles. While these limits can be severe in laboratory plasmas, the electron densities under solar wind or magnetospheric conditions are typically much lower, resulting in Debye lengths on the orders of 10m and 100m, respectively. Any electrostatic fields generated by the device would be capable of only localized penetration into the plasma background, far short of the length scales required to collect a significant flux. Further, increasing plasma densities resulting from the concentration of incident particles would amplify the shielding effect up to a critical density.

One means of circumventing these limitations is through the use of discrete, graduated electric fields operating in series. Incident particles respond only to the local electric field, designed to place them on trajectories leading to subsequent field regions – a type of electromagnetic lensing. A recent study (Jackson, 2004) suggests the use of charged concentric spherical grids to focus ~1GeV antiprotons from the GCR flux. The proposed system consists of an outer grid biased at +10MeV to reflect solar wind protons and positrons; an intermediate grid biased at –1GeV to decelerate the incident antiprotons; and finally an inner trapping grid biased to some sufficiently positive voltage for long-term storage. A schematic is shown in Figure (6.4).

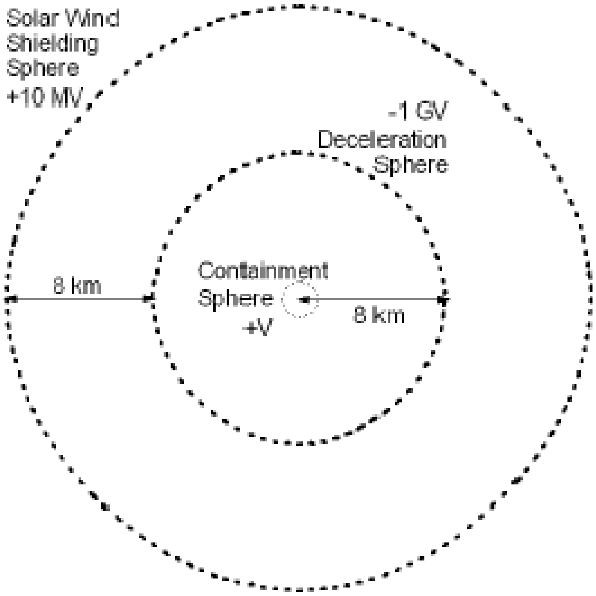

Figure 6.4 – Electrostatic collector proposed for the collection of GCR antiprotons (Jackson, 2004).

MODELING OVERVIEW

In practice, any conceivable system will generally require three modes of operation:

- Startup. The creation of large-scale electromagnetic disturbances will require correspondingly large quantities of energy. The power system must be capable of driving the system to steady-state operation within a practical time scale; as a practical limit, worst-case calculations are normalized for a one-year startup period.
- Focusing. Overall system performance is ultimately quantified by the rate at which antiparticles are collected; the ability of the system to concentrate and localize incident particle fluxes represents the fundamental limit of performance.
- Trapping. Some mechanism must be included to directly influence the localized antiparticle concentrations and ultimately transition them into long-term storage. We define a "trapped" particle as one whose trajectory is bounded within some reasonable distance from the device center, for a reasonably long duration. All matter of electrostatic and electromagnetic traps are viable options.

For the remainder of this chapter, we will focus primarily on analytical and computational techniques used in the simulation of particle focusing.

COMPUTATIONAL TECHNIQUE

We wish to study the motion of a charged particle – in this case, an antiproton – in the presence of electromagnetic fields. These fields may be uniform or non-uniform, static or dynamic, so long as they are well defined in both space and time. Given a set of initial coordinates in phase space $(x_0, y_0, z_0, u_0, v_0, w_0)$, the path of the particle through the simulation volume must be determined. For an adequate statistical population, we apply large-scale Monte Carlo analyses over a range of physical parameters spanning the design space.

As described in Chapter (6), the motion of a charged particle through an electromagnetic field is governed by the Lorentz force law. We can express the particle's trajectory using a system of six first order differential equations for position and relativistic momentum,

$$\frac{d\vec{s}}{dt} = \vec{V}, \tag{6.8}$$

$$\frac{d\vec{p}}{dt} = q\left(\vec{V} \times \vec{B} + \vec{E}\right), \tag{6.9}$$

which can be readily solved numerically. To that end, a simulation environment was developed in MATLAB using the well-known ODE45 package – an adaptive time-scale, fourth- and fifth-order pair Runge-Kutta-Fehlberg integration algorithm. ODE45 provides high accuracy for reasonable computation cost, with minimal additional development; however, other integration methods may be adapted to obtain similar results.

Each particle is assigned an initial position and velocity on the simulation boundary, and traced as it passes through the simulation space under the influence of electromagnetic forces induced by the collector's generated fields. To minimize computational cost, we consider a particle's trajectory "complete" once it either i) strikes the surface of the device, or ii) attains a distance greater than 1%

in excess of its initial distance from the device center (i.e., the particle passes outside the simulation boundary). Figure (6.5) shows an example trajectory for a GCR antiproton incident on the Earth's magnetic environment.

Rather than simulating single particles and applying the relevant Monte Carlo analyses "ex post facto," a novel approach was developed to vectorize the integration process. Expanding the original system of six first-order differential equations into a matrix of six-by-N differential equations, we effectively solve all N particle trajectories simultaneously, eliminating a significant degree of overhead computation and reducing computational cost by as much as 15- to 100-fold, allowing for the simulation of significant (10^5-10^6) particle counts over the course of a few hours on a reasonably fast desktop machine (2.0 GHz, dual-core CPU).

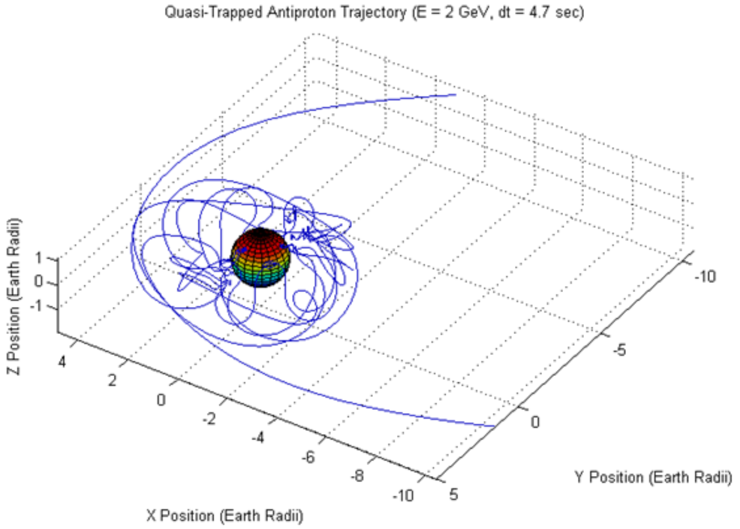

Figure 6.5 – Example GCR antiproton trajectory around Earth.

FIELD MODELING

In order to accurately simulate particle trajectories, we must first develop high-fidelity models of any electromagnetic fields, ambient or artificial, present in the system. In most cases, the ambient magnetic fields may be treated as uniform, and we will neglect ambient electric fields. Thus, it remains only to calculate the electromagnetic fields generated by the collector.

In the case of a single current loop with current *I* and radius *R*, the approach is relatively straightforward. By making use of elliptic integrals, we may obtain a closed-form solution for the magnetic field at an arbitrary point (Montgomery and Terrel, 1961). In particular, we have that,

$$B_\xi = B_0 \left(E(k) \frac{1-\alpha^2-\beta^2}{Q-4\alpha} + K(k) \right), \tag{6.10}$$

$$B_\rho = B_0 \frac{\gamma}{\pi\sqrt{Q}} \left(E(k) \frac{1+\alpha^2+\beta^2}{Q-4\alpha} - K(k) \right), \tag{6.11}$$

where B_ξ and B_ϱ are the axial and radial components of the magnetic field, respectively; $B_0 = \mu_0 I / 2R$ is the magnetic field intensity at the center of the loop; $\alpha = \rho / R,\ \beta = \xi / R,\ \gamma = \xi / \rho,\ Q = (1+\alpha)^2 + \beta^2$ are non-dimensional spatial coordinates; and *K(k), E(k)* are the complete elliptic integrals of the first and second kind, respectively. Their argument, $k = \sqrt{4\alpha / Q}$, is sometimes defined alternately as $m = k^2$, or $\alpha = \sin^{-1} k$. Note that for generality we have introduced a fixed cylindrical coordinate system (ϱ,ξ,θ) centered on the axis of the current loop.

To model the magnetic field associated with a Plasma Magnet configuration, we require three steps. First, we assume a geometry for the rotating antenna assembly, and calculate the time-varying magnetic field. For simplicity, we model the RMF antenna as two current loops, both centered on the origin but oriented perpendicular to each other in space, driven by oscillating currents separated by 90º in phase, as shown in Figure (6.6).

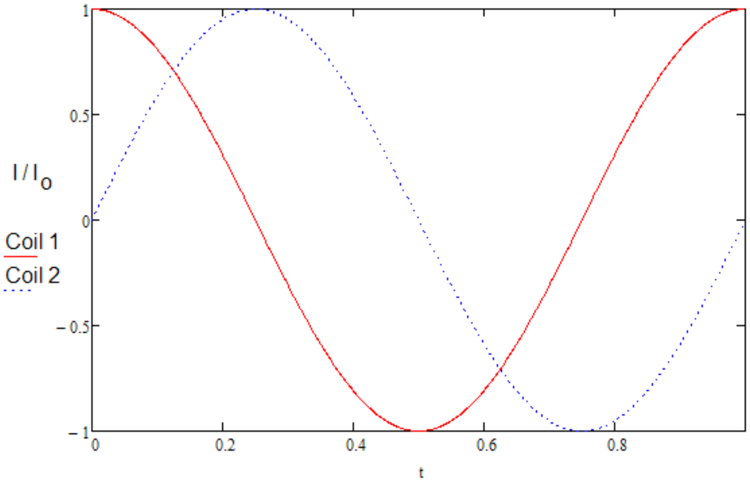

Figure 6.6 – Current profiles for a two-loop RMF antenna.

Next, we assume bulk characteristics for a background, neutral plasma, and use trapping limits (Pugacheva, 2002) to determine the extent to which the rotating magnetic field penetrates the plasma. In particular, we expect to find a characteristic radius r_{max} beyond which the RMF is too weak to fully magnetize free electrons.

Figure (6.7) depicts the penetration of a 1MA, 20m antenna RMF into a 10eV background plasma. The red curve represents the magnetic field intensity of the RMF as a function of radial distance from the antenna. The blue curve represents the minimum required magnetic field intensity to magnetize a free electron as a function of radial distance from the antenna. Following the methodology of Pugacheva et al., we consider an electron "magnetized" if its gyroradius is at most 1/10th the local magnetic field line radius of curvature. Approximating the field as a dipole, this equates to a gyroradius of at most 1/30th the radial distance from the antenna:

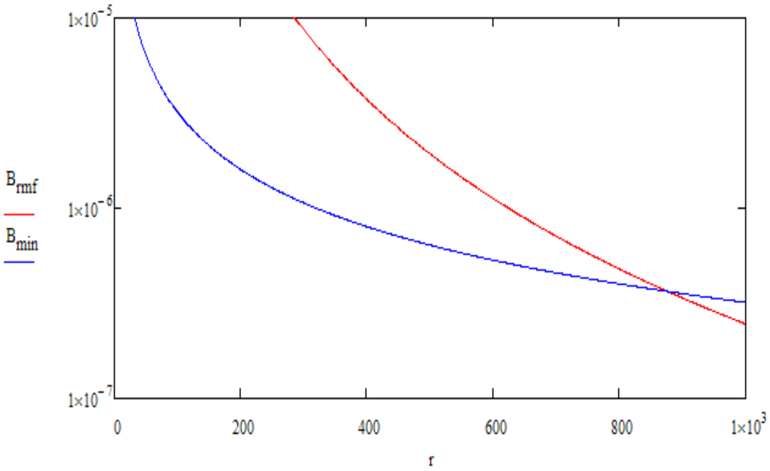

Figure 6.7 – RMF Penetration for 20m antenna operating at 1MA.

$$r_g = \frac{m_e v(kT_e)}{qB} < \frac{r}{30}, \tag{6.12}$$

$$B_{\min} = \frac{30\, m_e v(kT_e)}{q\, r}. \tag{6.13}$$

We thus find that the penetration depth of the RMF into the background plasma is given by the intersection of the two curves depicted above. Given a density profile for the background plasma, we may proceed to integrate the resulting current density induced by the RMF to yield the overall Plasma Magnet field. In particular, recall from Equations (6.10) and (6.11) that the magnetic field is the sum of a superposition of differential current loop elements, so that

$$B = \iint B_0 \Gamma(\vec{r}\,'). \tag{6.14}$$

That is to say, each differential current loop contributes a central field intensity, which is then scaled by a geometric term $\Gamma(\vec{r}\,')$ (the parenthetical terms in (6.10) and (6.11)) where $\vec{r}\,'$ denotes the relative separation of the differential current element from the point of calculation.

From the definition of B_0, we have that

$$B = \frac{\mu_0}{2} \iint n(r)\, q\, \omega \Gamma(\vec{r}\,')\, dA, \tag{6.15}$$

but we must take care to properly define the limits of integration. Recall that the RMF is only strong enough to magnetize electrons up to a radial distance $r_{\max}$ from the center of the antenna. Since magnetized electrons are confined to particular field lines, we include only those field lines that lie entirely within a distance $r_{\max}$ from the center of the antenna. Figure (6.8) depicts the magnetization region of a typical Plasma Magnet configuration. The large red circle approximates the farthest contour on which the field intensity is sufficiently high for magnetization. The shaded red regions represent the field lines lying entirely within the magnetization region. Approximating again the field as a dipole, we thus discretize the space bounded by the minimally trapped field line into concentric cylindrical current shells, each with width dr and height

$$\Delta z = r_{\max}^{1/3} r^{2/3} \sqrt{1-\frac{r^{2/3}}{r_{\max}^{2/3}}}, \tag{6.16}$$

such that we arrive at a closed-form expression for the magnetic field intensity,

$$B = 2\pi\mu_0 \int_0^{r_{\max}} \int_0^{\Delta z} n(r)\, q\, \omega\, \Delta z\, \Gamma(\vec{r}\,')\, dz\, dr. \tag{6.17}$$

An alternative derivation (Krasheninnikov, 1999) may be used to arrive at equation (6.17). While the details are beyond the scope of this report, the general approach takes the magnetic flux function φ as a solution to the Grad-Shafranov equation. The resulting expression for the magnetic field,

$$\vec{B} = \frac{B_0 R_0^{\alpha+2}}{\alpha\, r^{\alpha+2}} \left(\hat{\theta} \frac{\alpha\, h}{\sqrt{1-\mu^2}} + \hat{r} \frac{dh}{d\mu} \right), \tag{6.18}$$

where

$$\mu = \cos\theta, \quad \alpha = \frac{1}{\sqrt{\beta}}, \tag{6.19,6.20}$$

and *h* is a power series expansion in *θ*. We see that for high β plasmas, the magnetic field intensity vanishes as $1/r^2$, as opposed to the traditional $1/r^3$ in vacuum.

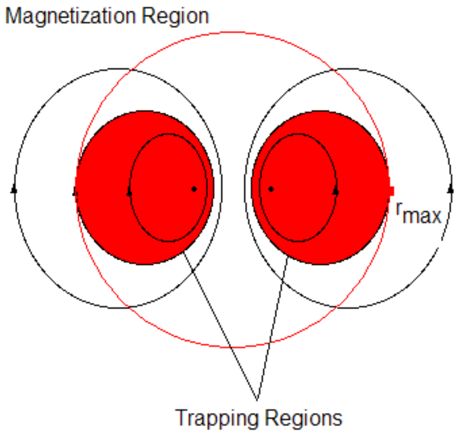

Figure 6.8 – Trapping regions for a typical RMF configuration.

INPUT MODELS

As described in previous chapters, there are two principal sources of antiprotons in our solar system. The first is the relatively dense population of antiprotons trapped in planetary magnetic fields, for which we can readily calculate differential flux models. In general, these antiprotons exhibit highly predictable bounce and precession motions as they respond to the planetary fields.

For a device operating in an equatorial orbit, we can reasonably model the input flux as a uniform shower of particles whose guiding centers travel with velocities parallel to the axis of the device. The distributions of energies and pitch angles are governed primarily by the production processes that replenish the population, as well as atmospheric interaction. The former shapes the distribution in energy, while the latter results in an upper limit (or "loss cone") on equatorial pitch angles. Around Earth, for example, antiprotons trapped in the radiation belts typically exhibit energies in the 10-250MeV range, with a loss cone of approximately 20°.

The relatively dense populations supported by planetary fields yield encouraging collection rates, simply by virtue of a naturally larger incident flux. They are, however, fundamentally limited by loss processes – the entire supply of antiprotons trapped in the Earth's radiation belts amounts to only a few hundred nanograms. Any significant collection from planetary sources would quickly exhaust the available supply, and the timescales for replenishment from pair production processes are typically much longer than any timescales involved in collection. In that respect, a much more promising source is the GCR flux itself.

The principle disadvantages of collecting directly from the GCR flux are two-fold. First, GCR antiprotons exhibit energies much greater than those found in planetary magnetic fields; the peak in the GCR spectrum occurs at approximately 2GeV, with non-negligible differential fluxes approaching as high as 10GeV. This makes GCR antiprotons considerably more difficult to focus and trap, for they spend far less time under the influence of any electromagnetic fields. Further, while practically infinite in supply, the GCR antiproton flux is exceedingly tenuous. Despite these shortcomings, however, it remains true that the GCR flux represents an essentially inexhaustible supply, with no preferential direction or pitch angle to limit collection efficiency.

FLUX MAPPING

In order to quantify performance, we must establish a suitable metric to characterize a given system's ability to focus incident fluxes. The simplest and most practical metric is simply local density; for a given trapping efficiency, the greater the number of particles present in a given region the more particles may be trapped by the system for long-term storage. Taking advantage of axial symmetry, we discretize the simulation space using cylindrical coordinates r,z,θ. The resultant "bins" take the shape of rings, with square cross-sections, centered on the device's axis of symmetry.

For a given particle, mapping the trajectory onto such a discretized space is equivalent to projecting the particle's trajectory onto the r-z plane. Applying Monte Carlo analyses, we can readily sum over the contributions from all particles, thereby "counting" the total number of particles passing through each bin. Together with the total flux incident on the system, and given a total number of simulated particles, the raw particle counts are converted to a local flow rate; that is, the number of particles (alternatively, the mass) passing through each bin per unit time. Figure (6.9) depicts a sample flux map calculated for a system operating in the GCR flux.

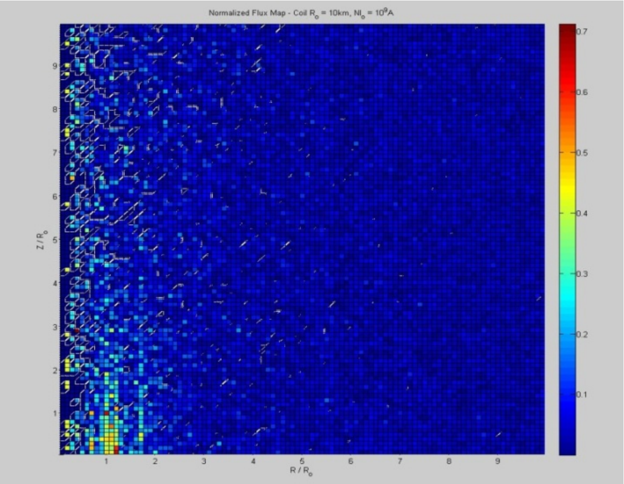

Figure 6.9 – Sample flux map depicting relative concentration in the r-z plane.

BUCKINGHAM PI ANALYSIS

The trajectories and initial conditions of source particles were recorded in the hope that trends in certain defining characteristics of "trapped" particles could be found. The problem of dealing with a large number of physical variables can be simplified by using dimensional analysis and the Buckingham Pi theorem. According to this theorem, we can reduce the number of dimensional parameters, deriving non-dimensional variables from the original parameters. These dimensionless variables are known as pi groups. The Buckingham Pi theorem also facilitates the design of scale models for trapping mechanism concepts.

Loosely stated, an equation involving a certain number *m* of physical parameters, and an additional number *n* of independent fundamental dimensions that are used to express those parameters, can be rewritten in terms of a lesser number *p* of dimensionless variables. This number is usually equal to the difference (*m – n*) of the number of variables and the number of independent dimensions that are needed to represent them. One of the main advantages of the theorem is its flexibility. As long as the vector space spanned by the original variable dimensions is also spanned by the dimensions of a set of pi groups, we may assume that said pi groups comprise a complete set of variables that completely define the system. Therefore, we set out to find the set of pi groups that take the most physically meaningful forms. In fluid mechanics, for instance, Mach and Reynolds Numbers are typical pi parameters.

For a typical, axially-symmetric, drift-limited system we can list 12 relevant physical variables; two coordinates for the position of a given particle (r, φ), three components for the initial kinetic energy of the particle (E_x, E_y, E_z), the mass and charge of the particle (m, q), the strength of the ambient magnetic field (B_{amb}), the radii of the outer and inner coils (R_O, R_I), and the currents in the outer and inner coils (I_O, I_I). The four (4) dimensions used to express these variables are length, mass, time and charge. That leaves us with eight (8) choices for the pi groups, which we choose to be (i) the ratio of the inner and outer coil radius (R_i / R_o); (ii) the ratio of the inner and outer coil current (I_i / I_o); (iii) the initial pitch angle of the particle relative to the local magnetic field (α_0); (iv) the relative strength of the magnetic field due to the system against the ambient field (B / B_0); (v) the relativistic beta (β); (vi) the ratio of the Larmor Radius and the outer coil radius (r_L/R_o); (vii) the particle's kinetic energy relative to magnetic field energy (E_k / E_B); and (viii) the initial polar angle (φ). Analyzing these dimensionless parameters allows for qualitative assessments of efficiency for the various proposed trapping mechanisms.

Having developed accurate and robust field models for simple one- and two-loop systems, as well as RMF driven systems, we may assess various prototype configurations. In particular, we wish to quantify collection rates and efficiencies for the various systems described in Chapter (6). In calculating raw collection rates, we may intuitively match prototype systems to baseline missions -- LEO, Jovian, Interstellar, etc – requiring certain a priori quantities of fuel. It should be noted, however, that due to radical differences in scale and concept, it is not always reasonable to compare systems by their gross performance. In these cases, alternative metrics are desired which incorporate such factors as launch mass/cost and operating power among others.

In this chapter, the various collector concepts are analyzed. For each concept, we attempt to arrive at "optimal" configurations which maximize some relevant performance metric; total collection rate (TCR), measured in nanograms per year; mass-specific collection rate (MSCR), measured in nanograms per year per kilogram device mass; power-specific collection rate (PSCR), measured in nanograms per year per watt; and cost-specific collection rate (CSCR), measured in nanograms per year per U.S. Dollar.

For each of the various system concepts described below, we make several key assumptions. First, where applicable, the current state of the art in superconductor technology (Zubrin, 2000) is assumed (current density of 1.7 x 10^8 A/m^2, material density of 9 x 10^3 kg/m^3); second, a period of one year is allotted for any start-up and/or transient phenomena; third, for all systems, launch costs are determined according to the present day Atlas V Program's incremental launch costs of approximately $8,800 USD/kg (Isakowitz and Hopkins, 2004); finally, where relevant, power systems have been scaled according to current state-of-the-art production limits of approximately 40 W/kg (Larson et al., 2005).

The various systems will be assessed according to present day limits of practicality. In many cases, particularly when optimizing for TCR, the adage "bigger is better" holds true; and yet it would make little sense to define a baseline system as being "infinitely large." As a practical limit, we place an upper bound on the total system mass of 10^6 kg, approximately the projected mass of the International Space Station. In other cases, power will be the limiting variable – here, we limit the design space to systems drawing on the order of hundreds of kilowatts (10^5 W) or less, in line with recently proposed power concepts such as the Prometheus nuclear program.

SINGLE- AND N-LOOP SYSTEMS

Initial estimates of system performance for single-loop systems were derived in Phase I. The approach was purely analytical, and focused on the effect of the curvature drift on incident particles. Specifically, the pitch angle of an incident particle will increase as it approaches the throat where the magnetic field intensity is greatest. The mirror point where the particle is repelled and returns along its original trajectory occurs when the pitch angle reaches 90 degrees. For any arbitrary magnetic field configuration, the relationship between the pitch angle (α), particle momentum (p), and magnetic field strength (B) may be written as

$$\frac{p_1^2 \sin^2(\alpha_1)}{B_1} = \frac{p_2^2 \sin^2(\alpha_2)}{B_2}, \tag{7.1}$$

for any two points (1), (2), along the particle's trajectory. This expression is based on the first adiabatic invariant and it remains valid even if an electric potential parallel to the field lines changes the particle's momentum. However, it is *not* valid in cases where the gradient of the magnetic field is large; specifically, equation (7.1) holds only if the change in magnetic field strength is negligible over a single Larmor orbit. Thus, while the adiabatic invariant is useful in solving analytically for the motion of non-relativistic particles in a large, locally homogeneous magnetic field (i.e., particles trapped in the Earth's magnetic field), it is a poor metric for estimating collection rates from highly localized, intense magnetic fields collecting from a relatively high-energy population, as is the case for most single-loop systems. Indeed, Phase I estimates suggested collection rates on the order of tens to hundreds of micrograms per year; subsequent simulations have reduced these numbers by several orders of magnitude.

The primary culprit is the grad-B drift. Whereas the effect of the curvature drift is to retard the particle's motion parallel to its local field line, the grad-B drift induces a perpendicular drift that further reduces the particle's directed momentum. The relatively larger field strengths in the near-field regions, together with the much smaller physical scale of the system, create incredibly steep gradients in the magnetic field that ultimately deflect a significant fraction of the incident particle flux. This effect makes single-loop systems extraordinarily good radiation shields, but unfortunately very poor collectors. To quantify this effect, let us examine the validity of the adiabatic invariant for typical antiprotons trapped in the Earth's radiation belts. We require that the magnetic field not vary appreciably over length scales on the order of one Larmor radius, or

$$r_L << \frac{B}{\nabla B}. \tag{7.2}$$

In practice, this condition is not satisfied for regions where either (i) the magnetic field strength is relatively low (i.e., the far-field region); or (ii) the local curvature of the field lines is relatively high. Thus in order to accurately assess the performance of single-loop systems (and thus, by extension, both N-loop and concentric loop systems), we must abandon previous analytical approaches and instead apply first principles to simulate particle trajectories directly, with a few key assumptions. For all simulations, we model the incident particle characteristics according to established flux data for both the Earth's radiation belts (see Chapter 2), and the GCR flux (see Chapter 4). Following the methodology described in Chapter (6), we generate flux maps to depict the relative concentration of the incident flux in the r-z plane. In order to quantify performance, we size the bins of the flux map assuming an electrostatic trap; that is, we assume that the radius of influence for any trapping mechanism is bound by the local Debye length (10-100m in the Earth's magnetosphere). The conversion to collection rate is a simple matter of multiplying the relative concentration by the total incident flux per unit time.

For single loop systems, there are two principal independent variables: (i) the radius of the device; and (ii) the operating current. Figures (7.1) and (7.2) depict the TCR in nanograms per year for various single loop configurations.

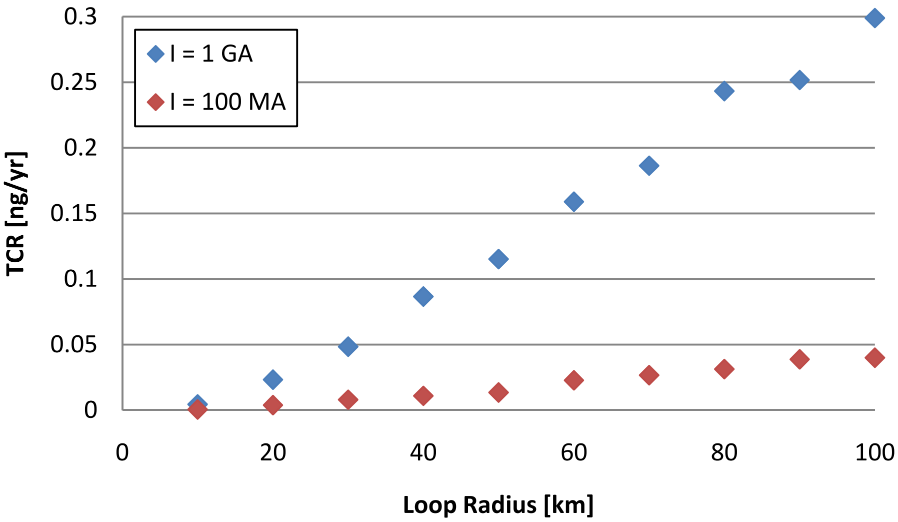

Figure 7.1 – TCR for Single Loop Systems in GCR Flux.

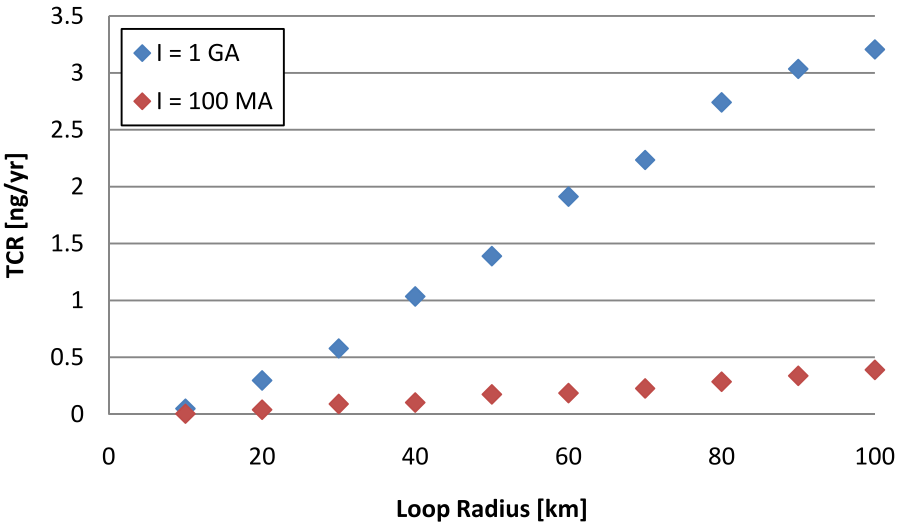

Figure 7.2 – TCR for Single Loop Systems in Earth Flux.

Immediately we observe that the total collection rate scales directly with the physical dimensions of the device. That is, for a given operating current, larger systems focus incident particles at a greater rate. Further, system performance is also found to scale with the operating current. Indeed, for single loop systems, maximizing TCR is as simple as building the largest coil possible, and operating at the highest attainable current. For devices measuring hundreds of kilometers and operating at billions of amperes, collection rates rival those of earth-based production (see Chapter 1). In practice, however, these systems are beyond the realm of practicality. Current superconductor technology sets a prohibitive lower limit on system mass, and typical systems draw power at rates exceeding the GW range, as shown in Table (7.1).

Radius \ Current	**100 MA**			**1 GA**		
	Mass	*Power*	*Cost*	*Mass*	*Power*	*Cost*
10 km	$3\cdot10^{8}$ kg	28.2 MW	\$2.8$\cdot10^{12}$ USD	$3\cdot10^{9}$ kg	2.8 GW	\$2.8$\cdot10^{13}$ USD
40 km	$1\cdot10^{9}$ kg	124 MW	\$1.1$\cdot10^{13}$ USD	$3\cdot10^{10}$ kg	12.4 GW	\$1.1$\cdot10^{14}$ USD
70 km	$2\cdot10^{9}$ kg	225 MW	\$2.0$\cdot10^{13}$ USD	$3\cdot10^{10}$ kg	22.5 GW	\$2.0$\cdot10^{14}$ USD
100 km	$3\cdot10^{9}$ kg	328 MW	\$2.8$\cdot10^{13}$ USD	$3\cdot10^{10}$ kg	33 GW	\$2.8$\cdot10^{14}$ USD

Table 7.1 – Mass, Power, and Cost Figures for Typical Single Loop Systems.

In light of the staggering costs and power draws associated with these systems, there is significant motivation to optimize not over raw performance, but rather over mass- and power-specific collection rates as shown in Figures (7.3) through (7.6).

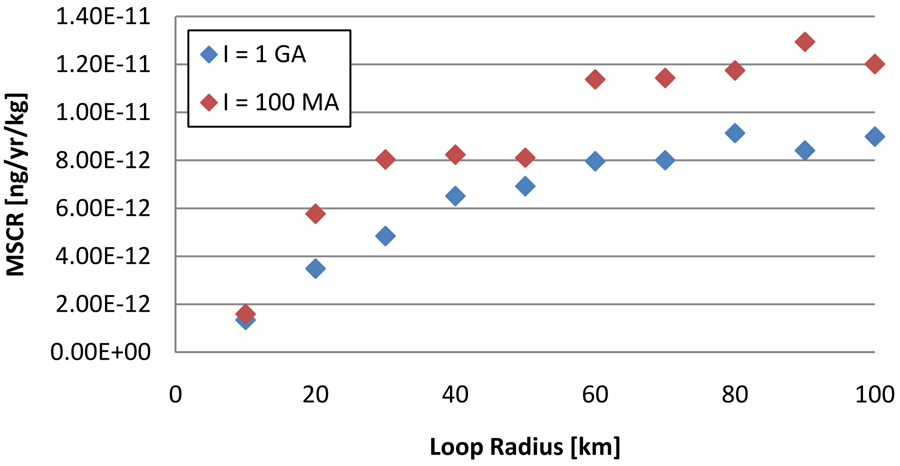

Figure 7.3 – MSCR for Single Loop Systems in GCR Flux.

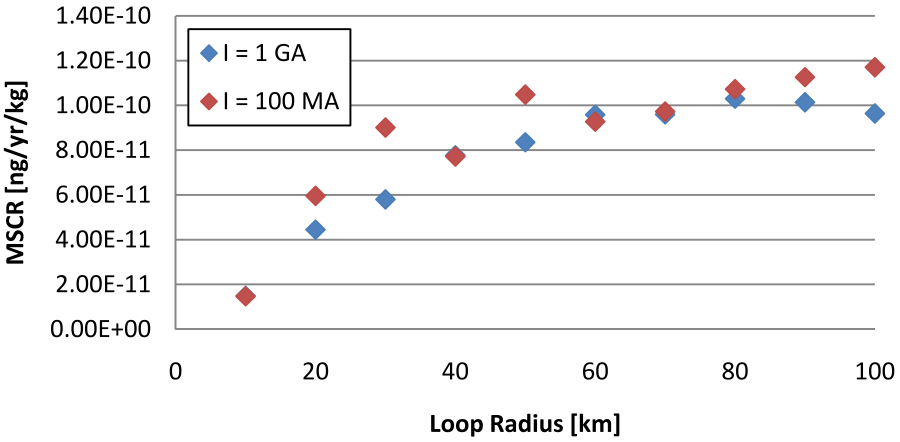

Figure 7.4 – MSCR for Single Loop Systems in Earth Flux.

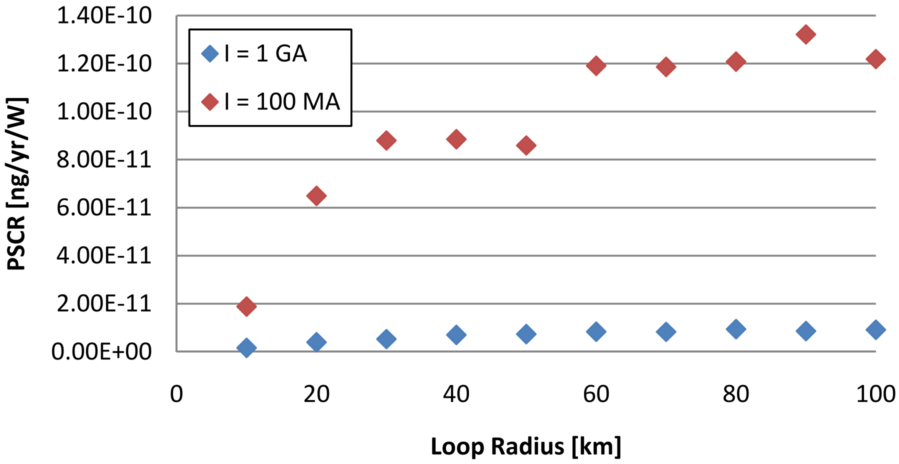

Figure 7.5 – PSCR for Single Loop Systems in GCR Flux.

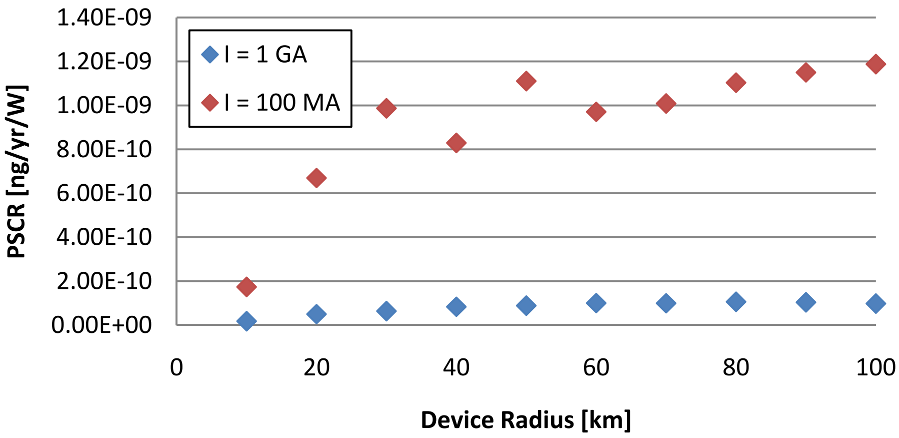

Figure 7.6 – PSCR for Single Loop Systems in Earth Flux.

Based on the above data, we find that lower-current systems are vastly more efficient from both a mass and power perspective. Armed with this knowledge, and given practical constraints such as a maximum launch mass or maximum power consumption, we can make objective comparisons between various points in the design space. In various single-loop simulations, strong trends emerged to suggest that optimal mass- and power-efficiency is achieved by maximizing the coil radius and minimizing operating current. However, because the limiting case of an infinitely large device operating a zero current is physically meaningless, we must bound the design space by specifying a minimum TCR. For single loop systems, operating at currents below 100 MA fails to produce practical collection rates, and such systems are thus not considered. Having established a minimum current, and thus bounded the design space, we may proceed with objective comparisons between systems using only mass, power, and TCR as performance metrics; a 100 km, 100 MA collector, for example, will outperform a 10 km, 1 GA collector of equal mass with an 88% decrease in power consumption (see Table 7.1).

As described above, typical single-loop systems generate magnetic fields that are simply ill-suited to efficient collection. The vast majority of the incident flux is deflected away from the device, so collection must occur at either very low rates, or over impractically large volumes. The use of multiple single-loop systems in tandem, as described in Chapter (6), allows us to exploit this effect to improve performance. However, simulations suggest only a marginal increase (approximately a five-fold improvement in collection rate) in performance for N-loop systems, for $N \geq 10$. While efficiency improves with increasing N, so too does total power and mass, thus rendering N-loop systems equally impractical. The limiting case of $N = \infty$, however, is of particular interest.

CONCENTRIC LOOP SYSTEMS

As discussed in the previous section, as well as in Chapter (6), concentric loop systems represent the mathematical and practical limit of an N-loop configuration with $N = \infty$. Figure (7.7) illustrates the superposition of current in each loop (shown in red), resulting in two net current flows (shown in blue), each of which gives rise to its own magnetic field.

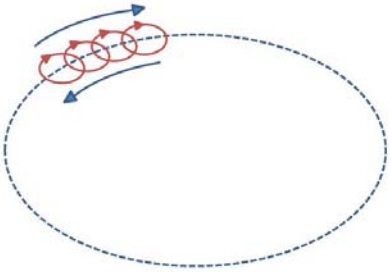

Figure 7.7 – Superposition of current in the limit of $N \rightarrow \infty$.

The opposing polarities of these fields, due to the difference in the direction of current flow, allow us to establish localized null-points in the magnetic field (regions where the net magnetic field is negligible) which are conducive to improved focusing; overall field gradients are reduced, and any high-field regions are localized near the coils, away from the center of the device. With the addition of the second coil, two new variables are introduced which relate directly to performance: (i) the radius of the inner coil; and (ii) the operating current of the inner coil. For simplicity, we replace these two variables with a set of non-dimensional counterparts; namely, (i) the ratio of inner loop radius R_i to outer loop radius R_o; and (ii) the ratio of inner loop current I_i to outer loop current I_o. The former is naturally limited to values between 0 and 1, while the latter is practically limited by the fact that a single power system must operate both current loops. As a conservative limit, we bound the ratio of currents to within one decade of unity, i.e. 0.1 to 10.

The first step in optimization is to eliminate one of these new variables. Specifically, we seek to determine a favorable operating point in either R_i/R_o or I_i/I_o. As shown in figures (7.8) through (7.10), we see that overall performance is largely insensitive to variations in the current ratio, except for the case when the ratio of loop radii approaches unity. In these cases, we observe a distinct linear trend in performance with increasing inner loop current. This is not altogether surprising – the limiting case of equal radii is equivalent to a single-loop system! And we have already seen that increasing the operating current leads to an increase in TCR for such systems. By operating at high ratios of loop radii and high inner loop currents, and thus localizing the high-field regions near the loops and away from the focusing regions, we achieve significantly increased performance at minimal mass and power penalties relative to single-loop systems.

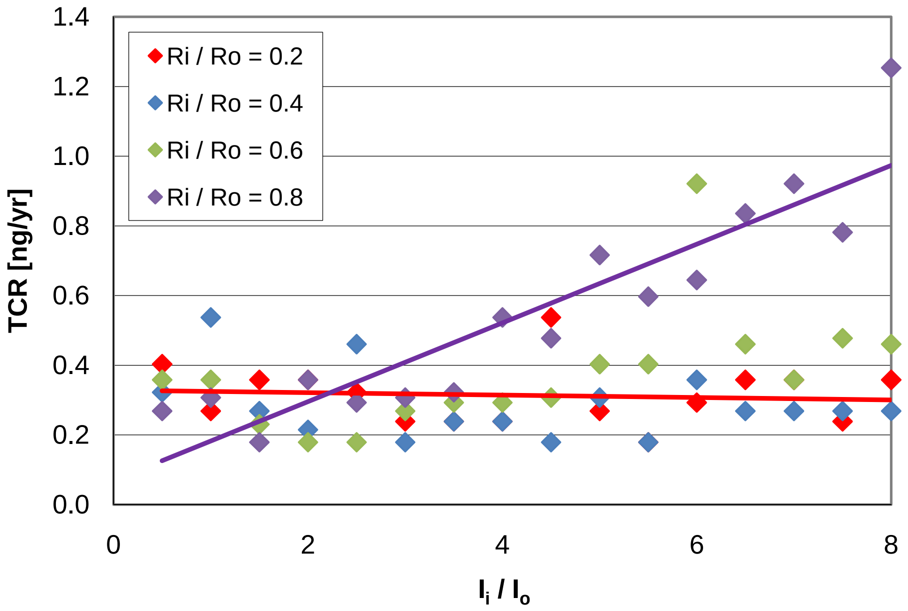

Figure 7.8 – TCR for 10km, 1GA Concentric Loop Systems in Earth Flux.

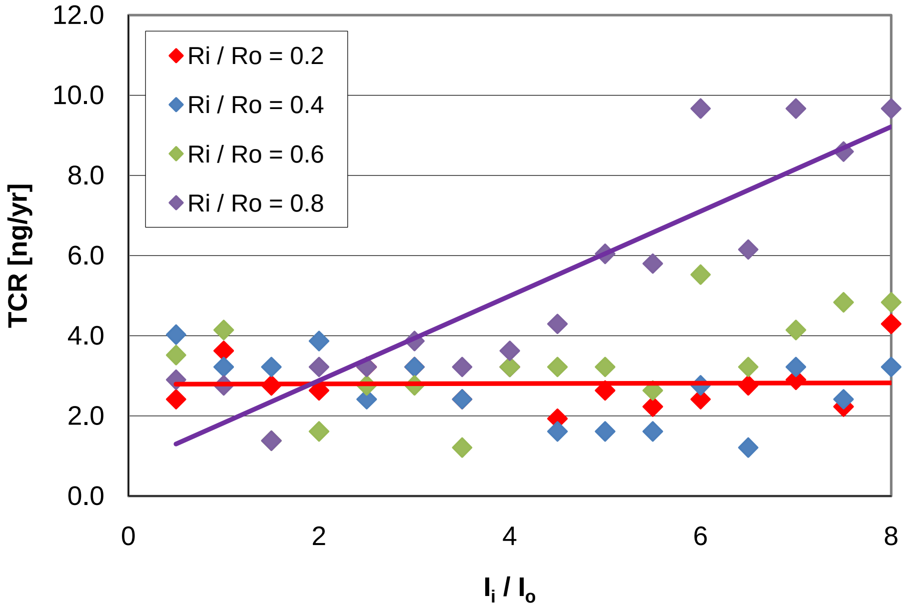

Figure 7.9 – TCR for 30km, 1GA Concentric Loop Systems in Earth Flux.

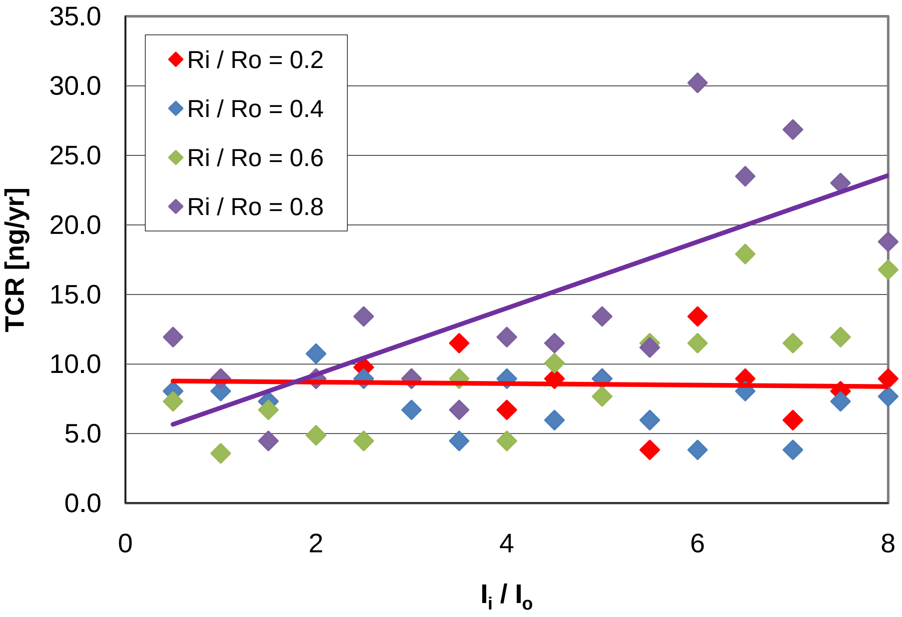

Figure 7.10 – TCR for a 50km, 1GA Concentric Loop System in Earth Flux.

Table (7.2) lists total collection rates for "practical" concentric loop systems. The outer loop current is fixed at 100 MA, and the inner loop radius and current are 0.8 and 8 times, respectively, those of the outer loop. For large systems, collection rates approach tens of nanograms per year – a significant improvement over single- and N-loop systems!

Outer Loop Radius \ Current	**I_o = 100 MA, R_i/R_o = 0.8, I_i/I_o=8**			
	Mass	*Total Power*	*Cost*	*Collection Rate*
10 km	$3\cdot10^{9}$ kg	3 GW	\$$2.8\cdot10^{13}$ USD	~0.49 ng/yr
40 km	$1\cdot10^{10}$ kg	10 GW	\$$1.1\cdot10^{14}$ USD	~3.1 ng/yr
70 km	$2\cdot10^{10}$ kg	20 GW	\$$2.0\cdot10^{14}$ USD	~6.7 ng/yr
100 km	$3\cdot10^{10}$ kg	30 GW	\$$2.8\cdot10^{14}$ USD	~9.6 ng/yr

Table 7.2 – TCR for practical Concentric Loop Systems.

STEP LADDER SYSTEMS

The "step ladder" concept is based on the principles of ion and electron optics. The trajectory of an incident particle is modified by a series of electrostatic rings, known as an Einzel lens, which guide charged particles along a desired path. The charge rings are placed within a few Debye lengths of one another to prevent large scale electrostatic shielding, which would reduce the effectiveness of the system. A significant challenge of this collection concept is the need to maintain position control of the charged rings. The rings will naturally repel one another due to the like charge found on each though this can be partially mitigated by the charge shielding that develops when they are placed much more than a Debye length away from one another.

Figure (7.11) depicts the focal length relations for standard accelerating (a) and decelerating (b) Einzel lenses. For the simplest case of a two-stage configuration, and assuming a maximum focal stage separation of 100 km, and an inlet radius of 100 km, we require relative changes in kinetic energy across each stage satisfying $\varphi_2 \sim -0.1\varphi_1$. Performance is then limited only by the fraction of the incident flux entering the inlet at the proper orientation. Conservative estimates suggest collection rates exceeding 10^{-5} ng/yr, although collection rates of 10^{-2} ng/yr may be possible if the system can be kept dynamically stable for separation distances under a few hundred meters. Despite the low collection rates, the advantage of the system is that the mass can be extremely low and they require virtually no power since the wires only hold a potential rather than carrying a large current. A 1mm thick wire that has been coated with a radioactive emitter to generate the potential could weigh less than 10,000 kg for a 100km system.

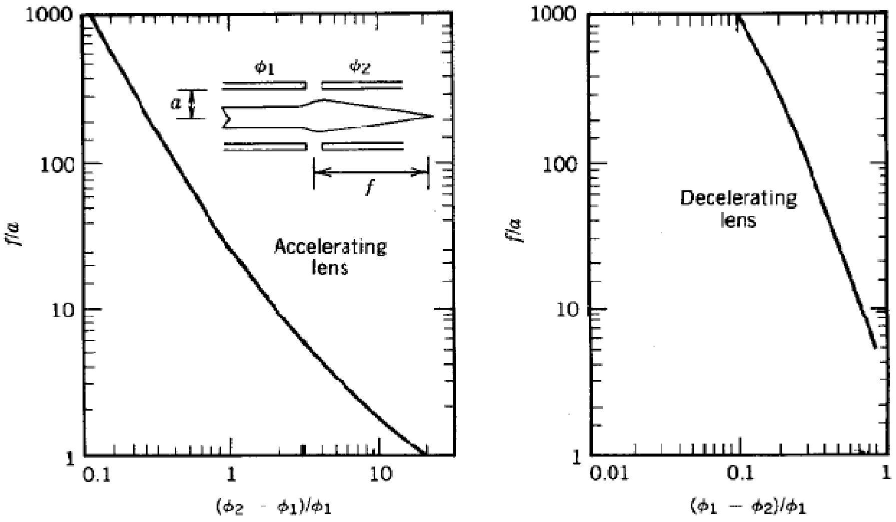

Figure 7.11 – Focal length relations for (a) accelerating and (b) decelerating Einzel lenses (MIT, 2007).

ELECTROSTATIC SPHERES

The use of electrically charged spheres for harvesting antimatter was previously studied by Jackson (2006). He proposed using wire mesh spheres to electrostatically collect antiprotons from the cosmic ray background. However, there appear to be a number of serious challenges with this solution. The concept calls for collecting just over one nanogram (1 ng) of antiprotons per year from three coincident spheres placed in interplanetary space. The design involves surrounding a 16-kilometer-diameter 'deceleration' sphere at -10^9 V with a 32-kilometer-diameter outer 'shielding' sphere charged to $+10^6$ V to repel solar wind protons. This is a dynamically unstable configuration and poses significant issues for maintaining control. However, the more pressing issue is the need for antiproton cooling when passing through the deceleration sphere. Jackson suggests using electron/positron cooling to further decelerate incident antiprotons with MeV to GeV of residual energy. The momentum must be completely removed otherwise the particle will be repelled from the device if it exits the deceleration sphere. Using the suggested electron cloud density, more than 10^{38} electrons are required. The mass of the cooling gas alone is nearly 10^9 kilograms and generates a tremendous space charge containment problem. Solutions must be found for obtaining 10^9 kg of positrons to neutralize the plasma and for preventing annihilation of the electron-positron mix. A possible alternative would be to use RF plasma wave coupling to slow incident particles for trapping, though this was not studied by Jackson.

PLASMA MAGNET SYSTEMS

As discussed in Chapter (6), the Plasma Magnet concept consists of a relatively small (10-100m) four-loop antenna (see figure (7.12)) situated within a neutral plasma. By supplying current to opposing loops with a relative phase difference, a rotating magnetic field (RMF) is established near the antenna. The RMF is operated at a sufficiently high frequency so as to elicit a response in the electron population, while the motion of the proton population (due to their relatively high mass) may be ignored. The resulting current due to the electron motion sustains a large-scale magnetic field within the plasma. The principle driver of performance is the RMF antenna's ability to influence the electron population; the more electrons driven by the RMF, the stronger the resultant magnetic field. We can quantify this by establishing a magnetization criterion, and determining a penetration depth for the RMF that will depend on (i) the antenna coil radius; (ii) the antenna operating current; and (iii) the temperature of the bulk plasma. Figure (7.13) depicts the maximum penetration distance along the plane of the RMF antenna for a bulk plasma based on solving for the radius in equation (6.13).

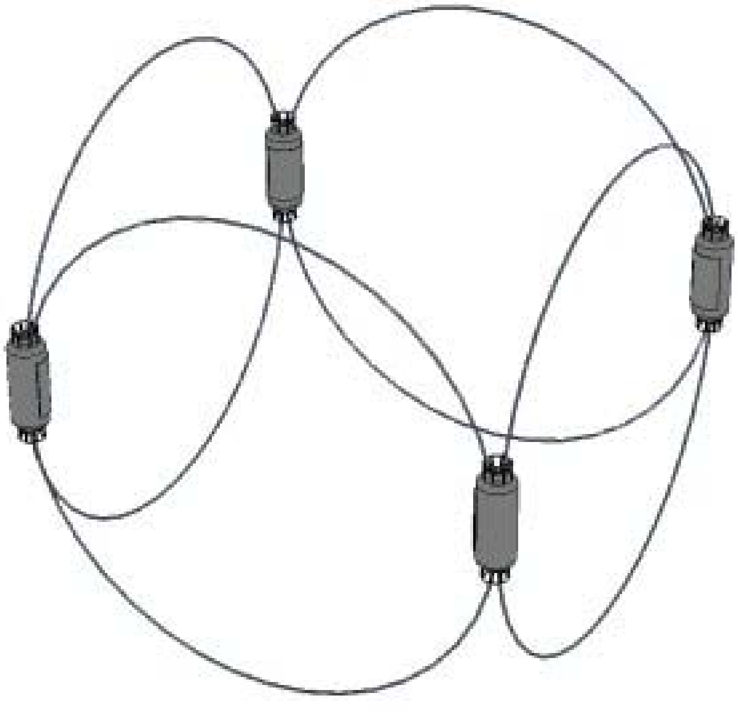

Figure 7.12 – Artist's Rendition of an RMF Antenna Assembly for Plasma Magnet Applications

RMF Penetration – and, by extension, collection performance – varies linearly with antenna loop radius for a given operating current. However, while penetration is improved by operating at lower plasma temperatures and higher currents, the resultant rise in resistivity dramatically increases power consumption. These competing effects will be discussed further at the end of this section.

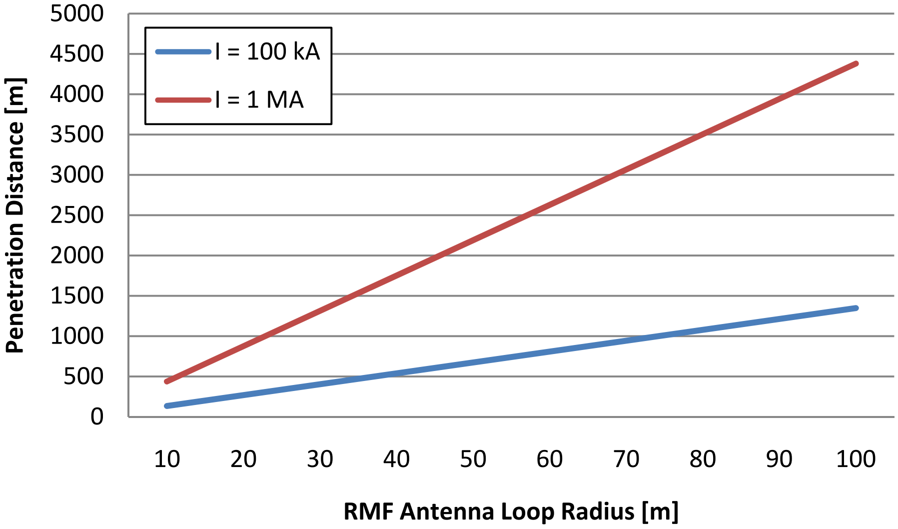

Figure 7.13 – RMF Penetration into a 10 eV Plasma.

Figures (7.14) and (7.15) show TCR for various Plasma Magnet configurations in the Earth Flux at 10^{18} m^{-3} and 10^{16} m^{-3} plasma densities, respectively, and an operating current of 100 kA. As expected, the "larger is better" trends observed in the single loop systems remain prevalent. For typical configurations studied, the intensities and volumes of influence of the resultant magnetic fields were comparable to those generated using single- or concentric-loop systems. However, the principal advantage of the Plasma Magnet lies in the use of a distributed, low-density plasma as the charge-carrying species; this leads to dramatically reduced gradients and low system mass with a corresponding improvement in overall performance. Overall antiproton collection rates exceed micrograms per year for typical systems that are just 100m in size while drawing just a few hundred kilowatts of power! This implies that the complete device could be inserted into its operational orbit with a single launch.

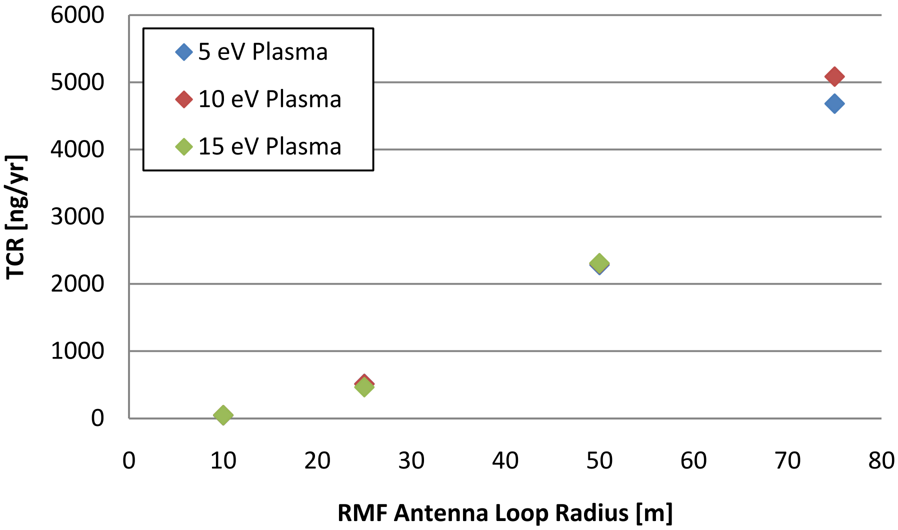

Figure 7.14 – TCR for Plasma Magnet Systems at 10^{18} m^{-3} plasma density, 100kA.

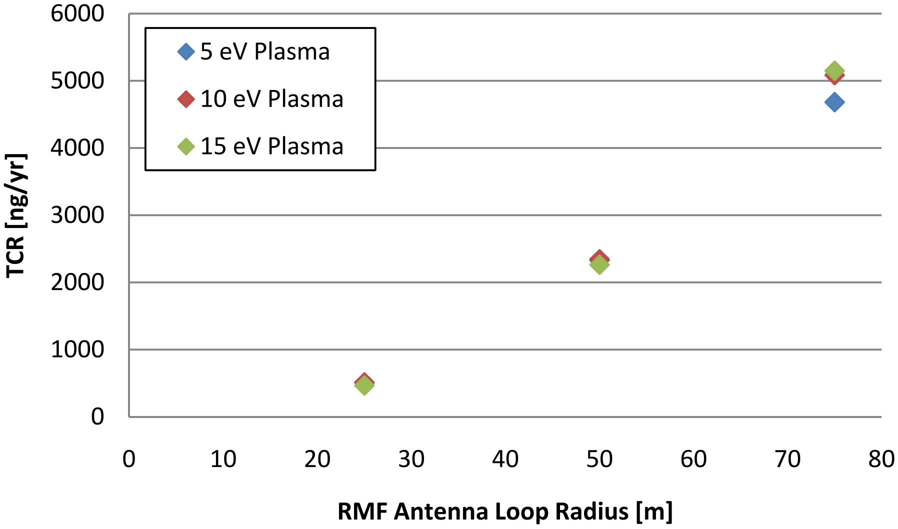

Figure 7.15 – TCR for Plasma Magnet Systems at 10^{16} m^{-3} plasma density, 100kA.

Perhaps the most surprising result is the relative insensitivity of performance to plasma density. In theory, higher plasma densities should result in increased magnetic field intensity, and thus improved collection performance. However, the corresponding increase in the magnetic field gradient retards this effect. Fortunately, this works to our advantage. Assuming a uniform resistivity of $\eta = 5.2 \cdot 10^{-4} \cdot kT_{eV}^{-3/2} ohm \cdot m$ throughout the magnetization region and integrating, we may express the power required to maintain driven current,

$$P_{RMF} = \int_V \eta j_\theta^2 dV \, , \tag{7.3}$$

where $j_\theta = n \, q_e \, \omega \, r$ is the azimuthal current density. We see then that the RMF power varies as the square of the plasma density, and inversely with plasma temperature. Figures (7.16) and (7.17) depict the mass-specific collection rates for various Plasma Magnet configurations in the Earth Flux at 10^{18} m^{-3} and 10^{16} m^{-3} plasma densities, respectively, and an operating current of 100 kA; By operating at relatively low plasma densities and high temperatures we reduce power consumption, and thus system mass with virtually no penalty to performance. While MSCR was found to scale favorably with decreasing plasma density and increasing plasma temperature, of interest is the reversal in behavior with respect to device size. At high densities (and thus high resistivity), the mass of the power system dominates – smaller devices are desired to mitigate the high power consumptions, despite the reduction in TCR. For lower densities, however, the mass of the power system becomes less significant, allowing for larger devices to maximize collection efficiency.

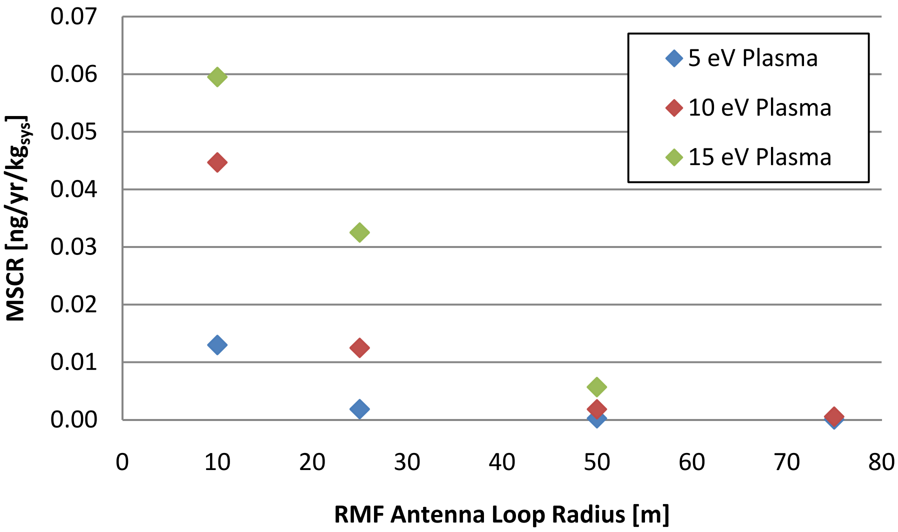

Figure 7.16 – MSCR for Plasma Magnet Systems at 10^{18} m^{-3} plasma density, 100kA.

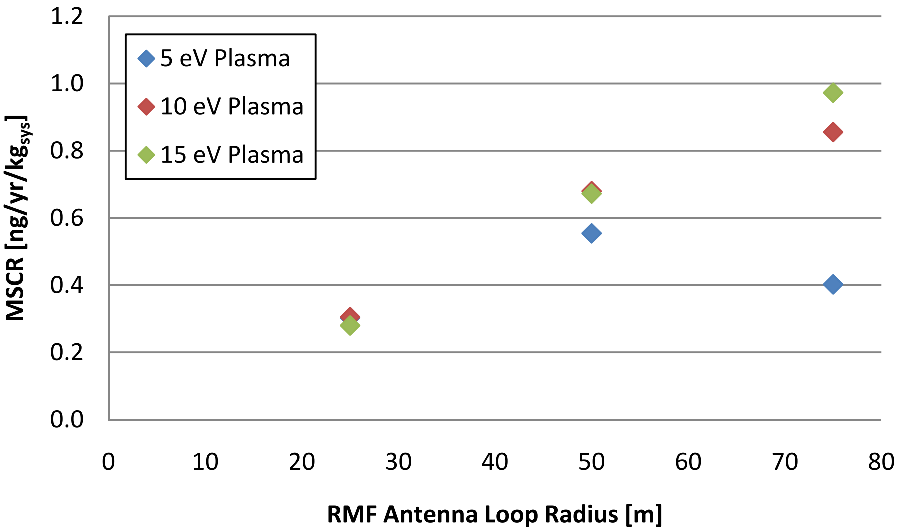

Figure 7.17 – MSCR for Plasma Magnet Systems at 10^{16} m^{-3} plasma density, 100kA.

So far, we have seen almost exclusively monotonic trends in performance; we are faced with the same dilemma as before, in that we must define some practical limits in lieu of "optimizing" toward an infinitely large device operating in a zero-density, infinite-temperature plasma. One useful metric to consider is total capacity – how much antimatter fuel can we reasonably expect to store? The confinement of charged particles in a magnetic field is limited (Brillouin, 1945) to a maximum achievable density of

$$n_B = \frac{B^2}{8\pi m c^2}, \tag{7.4}$$

at which the repulsive electrostatic and centrifugal forces on the confined particles are balanced against the Lorentz force supplied by the RMF. For antiprotons, the storage of practical quantities (10-100 ng) within a volume enclosed by the device requires plasma densities exceeding 10^{16} m^{-3}. The following tables depict the relevant figures of merit for various Plasma Magnet configurations operating at this minimum plasma density in the Earth flux.

RMF Antenna Radius	Collection Rate [ng/yr]	Antenna Mass[kg]	RMF Power [W]	Power System Mass [kg]	Total Mass [kg]	Cost [USD]
25	511.29	1662.35	1.1k	27.38	1689.73	$14.9M
50	2328.80	3324.71	35k	876.00	4200.71	$37.0M
75	4681.57	4987.06	266k	6652.50	11639.56	$102M

Table 7.3 – Figures of Merit for Plasma Magnet Configurations with $n=10^{16}$, $kT=5eV$ Plasma

RMF Antenna Radius	Collection Rate [ng/yr]	Antenna Mass[kg]	RMF Power [W]	Power System Mass [kg]	Total Mass [kg]	Cost [USD]
25	508.45	1662.35	158	3.94	1666.29	$14.7M
50	2345.50	3324.71	5.04k	126.03	3450.73	$30.4M
75	5085.84	4987.06	38.3k	957.00	5944.06	$52.3M

Table 7.4 – Figures of Merit for Plasma Magnet Configurations with $n=10^{16}$, $kT=10eV$ Plasma

RMF Antenna Radius	Collection Rate [ng/yr]	Antenna Mass[kg]	RMF Power [W]	Power System Mass [kg]	Total Mass [kg]	Cost [USD]
25	465.26	1662.35	51	1.26	1663.62	$14.6M
50	2262.56	3324.71	1.62k	40.40	3365.11	$29.6M
75	5149.64	4987.06	12.3k	306.75	5293.81	$46.6M

Table 7.5 – Figures of Merit for Plasma Magnet Configurations with $n=10^{16}$, $kT=15eV$ Plasma

DISCUSSION

PERFORMANCE COMPARISON

The Plasma Magnet emerges as the clear winner in direct comparison with all other concepts. As previously alluded to, the use of distributed, low-density plasma results in significantly shallower field gradients that suppress the natural tendency of the magnetic field to shield against incident radiation. Power consumption and total system mass are also significantly reduced with the elimination of superconducting coils as the charge carrying mechanism. Table (7.6) lists figures of merit for baseline systems of each of the concepts. The collection rates

As shown below, a baseline Plasma Magnet system is well within reach given current or near-future technology. In fact, as shown in Table (7.7), the above system exceeds current Earth-based production efficiency by more than an order of magnitude! Operating in the more tenuous GCR flux, collection rates exceeding 0.12 ng/yr are attainable with the baseline system design. Substantial improvements in collection rate would be expected with a system design optimized for the GCR flux. In total, if antimatter is required for space propulsion, the plasma magnet is more than five orders of magnitude more cost effective when considering the storage traps used to transport the antiparticles to orbit.

Parameter	**Single-Loop**	**N-Loop**	**Concentric Loop**	**Step Ladder**	**Jackson Sphere**	**Plasma Magnet**
Coil Radius	100 km	10 km	100 km	100 km	16 km	100 m
Operating Current	10^9 A	10^9 A	10^9 A	N/A	N/A	10^5 A
Plasma Density	N/A	N/A	N/A	N/A	N/A	2×10^{16} m^{-3}
Plasma Temperature	N/A	N/A	N/A	N/A	N/A	15 eV
Coil Mass	3.3×10^{10} kg	$10 \times 3.3 \times 10^9$ kg	6.6×10^{10} kg	10,000 kg	12,000 kg	6,600 kg
Power	32.8 GW	28.2 GW	65.6 GW	N/A	10 GW	200 kW
Power System Mass	8.2×10^8 kg	7.05×10^8 kg	1.6×10^9 kg	N/A	2.5×10^8 kg	5.2×10^3 kg
Total Mass	3.4×10^{10} kg	3.3×10^{10} kg	6.8×10^{10} kg	10,000 kg	10^9 kg	12,000 kg
Collection Rate	0.2 ng/yr	1 ng/yr	4 ng/yr	0.01 ng/yr	1 ng/yr	8.6 μg/yr
Launch Cost	$\$3.0 \times 10^{14}$ USD	$\$3.0 \times 10^{14}$ USD	$\$6.0 \times 10^{14}$ USD	$\$8.8 \times 10^7$ USD	$\$8.8 \times 10^{12}$ USD	$\$1.0 \times 10^8$ USD
Figure of Merit	$\$1.5 \times 10^{15}$ USD/ng/yr	$\$3.0 \times 10^{14}$ USD/ng/yr	$\$1.5 \times 10^{14}$ USD/ng/yr	$\$8.8 \times 10^9$ USD/ng/yr	$\$8.8 \times 10^{12}$ USD/ng/yr	$\$1.2 \times 10^4$ USD/ng/yr

Table 7.6 – Baseline system comparison.

	CERN/Fermilab	**Plasma Magnet**
Production Rate	2 ng/yr	25 ng/day
Storage Capacity	4 pg	110 ng
Storage Time	$> 10^5$ s	$> 10^7$ s
Generation Cost	$\$4.8 \times 10^5$ USD/ng	N/A
Launch Cost	$\$\sim 10^9$ USD/ng	9.0×10^5 USD/ng[**]

Table 7.7 – Comparison of Plasma Magnet systems with Earth-based production.

PARTICLE TRAPPING

While the previous sections have thoroughly addressed the problem of focusing incident particle fluxes, no analysis has yet been carried out on the trapping process for the system – the application of the Brillouin limit merely sets a fundamental limit on capacity. In order to trap an incident particle, two steps are required: first, the system must be able to degrade the particle's kinetic energy to a sufficiently low level so as to keep the particle from escaping on an open trajectory; second, the system must subsequently transfer the particle either onto a closed magnetic field line of the system, or into some form of electromagnetic trap.

[**] Based on a one-time collection of the full 110 ng capacity.

Several possible mechanisms may be used to accomplish the former:

- Slab Interaction: A slab of material is placed along the incident particle's trajectory. Scattering processes reduce the particle's kinetic energy, but care must be taken to maintain a sufficiently low cross-section for annihilation. Another disadvantage of this technique is the large mass required to slow the particle sufficiently.

- RF Coupling: Polarized RF waves may be used to selectively degrade particle energy to promote the trapping of a particular species based on the gyro motion of the particle. This can be used to bias the system to collect antiprotons instead of protons based on their opposite charges.

- Electrostatic Deceleration: Charged bodies are used to exert a retarding force on incident particles by making the particle traverse a potential well. Once again, the opposite polarity of protons and antiprotons can be used to bias collection towards one species or another.

A retarding potential generated by two oppositely charged wire meshes could be used to form a large capacitor across the entrance of the trapping region. A properly biased potential (on the order of the particle's energy) would remove the majority of an antiproton's momentum while accelerating a proton so it passes through this system without being trapped. Polarized RF sources can also be used to remove residual momentum and ensure capture. Both mechanisms preferentially operate on particles with the proper charge enabling the separation of protons and antiprotons based on their opposed charges.

ADDITIONAL CONSIDERATIONS

Several issues merit additional consideration and/or further research. The use of superconducting material in many of the above system concepts introduces the need for thermal control. These materials operate at cryogenic temperatures, and even the latest high temperature superconductors will need innovative cooling systems to achieve high current densities and maximize performance. Active cooling and/or bringing consumable cryogenic liquids to cool the coils would be less desirable than relying on passive thermal control. Both types of systems are well established in the space industry – though perhaps not at this scale. Passive cooling works by using selective coatings to reduce the absorbtivity (α) in the optical spectrum where most of the Solar energy is concentrated, while maximizing the emissivity (ε) in the infrared region of the spectrum so heat can be dissipated to the cool 3K deep space background. This is especially challenging when operating near planets since there will be a large view factor to the relatively warm planet.

Ideally, a single film with a low absorbtivity/emissitivy ratio could be used for cooling, though directionally oriented multi-layer insulation (MLI) may be required to cool the coils when operating near Earth. Figure (7.18) shows the calculated temperature based on the effective solar absorptivity/emissivity ratio. To keep the coil temperature below 100K (and preferably much lower) MLI insulation would be required when operating near Earth. Operating the device at Jupiter or beyond is likely to be feasible with second surface film coatings only since Sheldahl currently offers a product with the desired solar absorptance to emittance ratio. Details of the thermal control system will need to be investigated in more detail as part of future research activities.

Dynamic stability is also an important consideration meriting further research, particularly in light of the strong magnetic fields associated with many of the above concepts. Operating a spacecraft with a large intrinsic dipole field may introduce large torques or external forces based on its interaction with the external environment. A current loop experiences a torque when exposed to an ambient

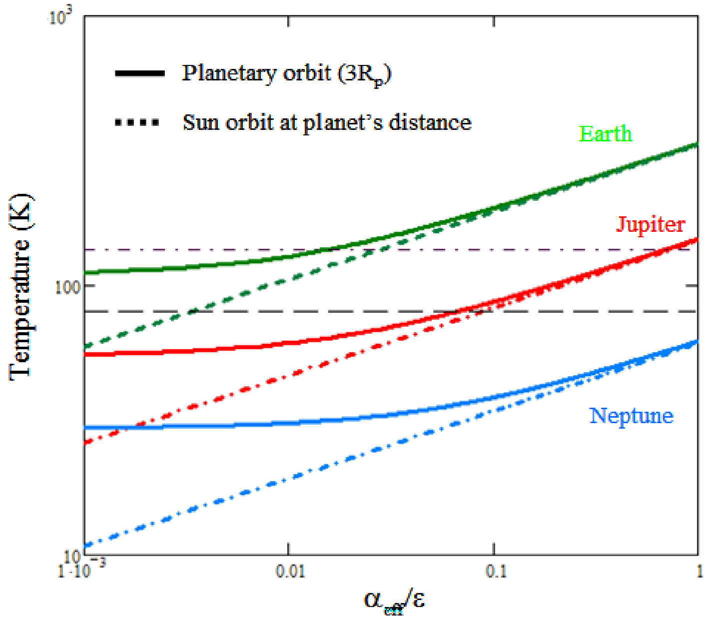

Figure 7.18 – Average coil temperature for various operating scenarios.

magnetic field that forces the dipole to align with the local field lines. If no damping is present, the loop will precess around the field lines due to any initial misalignment. While there is no net external force induced when the coils are located within a constant field, translation can still occur in the presence of field gradients.

Finally, any experimental verification of system performance as well as the design and testing of trapping mechanisms should be carried out using properly scaled systems. Specifically, by the Buckingham Pi theorem, all non-dimensional parameters impacting performance should retain their values. For laboratory-scale experiments, this will require the use of electrons rather than antiprotons, and thus care must be taken to account for additional loss mechanisms (bremsstrahlung, synchrotron, etc.). For an analysis possible laboratory scaling and the effect of synchrotron losses, please refer to Appendix B.

TECHNOLOGY DEVELOPMENT REQUIREMENTS

The collection and use of antimatter produced naturally in the space environment requires four fundamental advances: an understanding of the natural distribution of antimatter, a highly efficient collector, a stable storage medium, and a mechanism to induce thrust. The proposed collection system does not require the development of any fundamentally new technology to make it work. However, the demonstration of key technologies and significant improvements in several areas would improve the risk weighted economic feasibility. To this end, we have identified the following technologies that need to be demonstrated at a TRL level of seven (7) or above.

TECHNOLOGIES (IN ORDER OF IMPORTANCE)

- Compact mass spectrometer placed in highly eccentric orbit. In situ measurements of antimatter fluxes in the Earth's radiation belt and around the Jovian planets have not been made. The models developed as part of this program should be verified by direct experimental evidence before significant resources are committed to implementing a full system. Current orbital missions do not have the spatial and/or property coverage to characterize the relevant environment. A compact mass spectrometer capable of differentiating protons, antiprotons, electrons, and positrons should be developed and flown in a highly eccentric orbit with an apogee of at least six Earth radii (6 R_E) to completely characterize the antiproton and positron environment. Such a system will also contribute greatly to radiation belt knowledge and the interaction between the magnetosphere and the Sun.
- Large-scale demonstration of a plasma magnet. The technology is a critical path item that appears to provide the only mass-efficient system capable of collecting significant quantities of antiprotons. The RF generation equipment and its integration with large-scale coils in the space environment need to be demonstrated.
- Low mass, high strength, long strand, ultra-high current loops. Though the plasma magnet significantly reduces the need for high current wires, RF coils would still benefit from higher current densities. High temperature superconductors with current densities much greater than 10^{10} A/m^2 at 90K will enable far more compact and mass-efficient systems.
- Radiation tolerant in-orbit power source. The particle collection system is required to operate in a high radiation environment. Though the magnetic field will shield the system from much of the incoming flux, a radiation tolerant power source is necessary to generate the initial current before the field is fully established. The intrinsic energy contained in the field dictates that a high power source be available in order to charge the system in a reasonable time. A space-qualified nuclear reactor with a power output of at least 100 kWe is desirable.
- Antiproton catalyzed fission/fusion engine. Nanograms to micrograms of antiprotons do not have enough intrinsic energy to propel a spacecraft to high velocities when exclusively using the annihilation products. Instead, most concepts rely on using antiprotons to induce fission reactions. The antiprotons catalyze nuclear reactions in sub-critical fissile material to propel the vehicle by leveraging the nuclear material in a safe and controllable manner.
- Passive cooling systems. Reduced-mass multi-layer thermal blankets for passive temperature control of large structures with $T_{max} < 90K$ at 1 AU will improve the overall mass efficiency and reduce requirements on the high temperature superconductors wires used.
- Affordable lift. Reducing the cost to orbit with new affordable heavy lift options, though not strictly required, will improve overall feasibility.

FUTURE RESEARCH

This program investigated the basic feasibility of extracting antiparticles from the natural environment for use in space propulsion. Most of the fundamental issues have been investigated which has given us a feel for the major effects and potential of the technology. However due to the premature end to the program, many of the phase II plans were not fulfilled. A great deal of additional analysis, experiments, and testing will be required to precisely quantify the potential of the technology. The following are some of the key items that need to be explored in more detail before committing to hardware development.

- Earth antiproton radiation belt model refinement
    - The albedo antineutron source statistics should be improved to enable a more precise and better fit to be developed. In particular, particle tracing should be used to evaluate rigidity cutoff effects in more detail.
    - Higher order terms in the magnetic field model should be included in the decay injection and loss models.
    - The efficiency of injecting antiprotons from an external source (GCR flux) should be investigated as an additional source term.
    - The time averaged steady state model should be replaced with a dynamic model of the environment to model its evolution as the solar environment changes.
- Positron model
    - The overall model needs to be refined with additional work focused on better quantifying the source and loss terms.
    - The production and escape of solar positrons should be modeled in detail. In addition, the efficiency of injecting these into the Earth's radiation belts should be evaluated.
- Jovian radiation belt model refinement
    - The dusty rings and other debris around each planet should be included in the models directly.
    - The more careful analysis of rigidity cutoff effects based on particle tracing through detailed magnetic field models should be included in future analyses.
    - The effect of Moons orbiting in a plane inclined from the magnetic equator should be included in future models, especially for Uranus and Neptune where this could alter the loss terms significantly.
    - A better model for diffusion rate coefficients should be added when/if they become available.

- Increase the magnetic scoop model fidelity and supplement with experimental data.
    - The behavior of the plasma magnet is very complex and needs to be explored in greater detail. Additional transport modeling needs to be completed using a 3D, time-dependent model of the RMF.
    - The electron current model should be augmented to include collisional effects, pressure gradients, and other loss mechanisms. Ideally, a full MHD equilibrium model should be applied to characterize the driven current.
    - The specifics of the transfer of incoming field lines onto closed field lines for trapping needs to be designed and verified with detailed modeling and experiments.
    - Experimental verification of the plasma magnet field model can be completed by driving electrons in a scale model placed in a plasma test chamber.
    - A higher-resolution model of non-neutrality in the Brillouin limit should be used to improve fidelity.
    - Design specifics should be worked out in more detail; this includes thermal and power subsystem design.
- The system design should be refined.
    - The integrated propulsion system needs to be flushed out to determine if transferring the particles to another vehicle for use is required.
    - The relative value of intrinsic radiation shielding should be quantified.
- Precursor and flight system concepts should be explored in more detail
    - The development program will progress through the following sequence
        - Analytical modeling
        - Detailed modeling
        - Experimental ground based verification
        - Science verification by piggybacking on other missions
        - Proof of concept LEO flights
        - Flight system development
    - Probable flight opportunities should be investigated.
- A more detailed look at the technology development requirements should be completed.
    - This, along with risk estimates should be used to refine the feasibility estimates.

- Identifying key development elements that are common to other exploration or science missions is essential to maximize the probability of success. In particular, identifying other high value science objectives (e.g. the search for dark matter) that share similar science goals should be emphasized to maximize the return on investment for potential experiments and flight opportunities.

High-energy galactic cosmic rays (GCR) are pervasive through our galaxy and constantly bombard the upper atmosphere of Earth with energies up to 10^{20} eV per nucleon. The exact nature of the flux is uncertain, but the particles are believed to originate from events both in and out of our galaxy (Biermann and Sigl, 2002). Moskalenko et al. (2002) provides an overview of GCR propagation in the context of interstellar antiproton generation. The GCR flux can also interact with the Earth's atmosphere to locally produce antiparticles (Huang, 2003). When a high energy proton strikes a particle in the interstellar medium or in a planet's atmosphere, its kinetic energy can be converted to matter when above the energy threshold,

$$E_{th} = m_P\left(2 + \frac{4}{A}\right), \qquad A.1$$

where m_p is the mass of a proton and A is the mass of the atmospheric or interstellar constituent struck by the incident particle. A proton-proton reaction results in the two original protons plus a proton and antiproton generated through pair production such that

$$p + p \rightarrow p + p + p + \overline{p}\,. \qquad A.2$$

Likewise, an equivalent process can generate a neutron/anti-neutron pair. The antineutron subsequently decays into an antiproton, positron, and neutrino with a half-life of just over 10 minutes in the reference frame of the particle.

The ratio of protons to antiprotons is an important measurement in the search for dark matter as well as a number of other physical processes including bounding restrictions on the amount of antimatter that can exist in the universe. As a result, a significant number of experiments have been performed to measure the ratio between the natural proton background and the antiproton flux. Over a period of several decades, measurements have been made in high altitude balloons, LEO satellites and spacecraft (including the space shuttle). Figures (A.1) and (Figure) from Picozza et al.

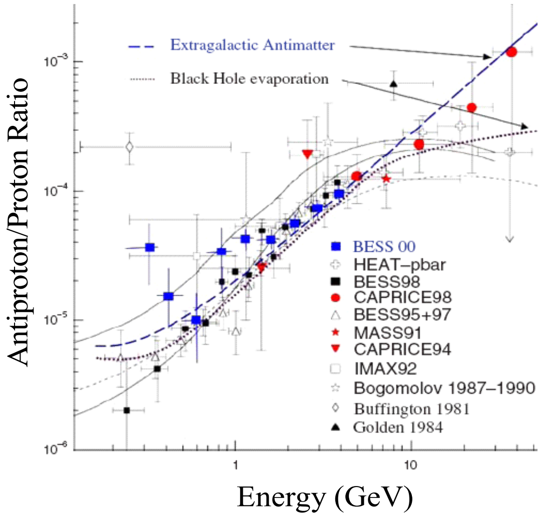

Figure A.1 — Measured Proton/Antiproton Ratio. (Based on Picozza et al., 2003)

(2003) summarize the resulting measurements obtained. The antiproton/proton ratio is approximately 10^{-4} when integrated over the total particle population though there is a strong dependence on the particle's energy. A dependence on solar cycle is also seen. (Labrador and Mewaldt, 1997) Positrons contribute to nearly 10% of the overall electron and positron flux.

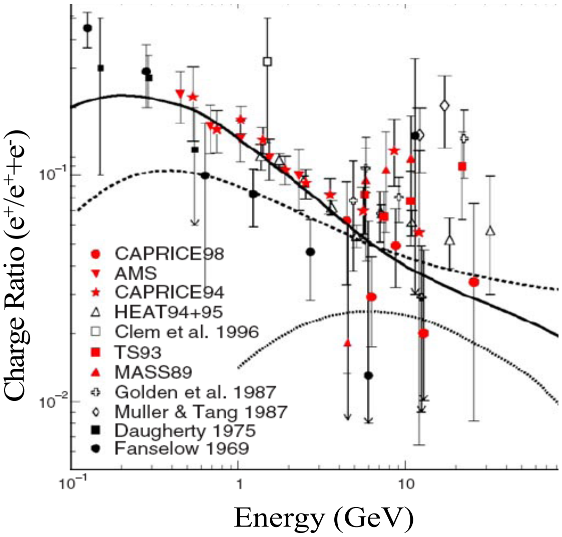

Figure A.2 - Measured Positron Fraction. (Based on Picozza et al., 2003)

Charged particles moving in a magnetic field are influenced by the Lorentz force,

$$\mathbf{F} = q(\mathbf{v} \times \mathbf{B} + \mathbf{E}) \tag{A.3}$$

where q is the charge, $\boldsymbol{v}$ is the particle velocity, $\boldsymbol{B}$ is the magnetic field and $\boldsymbol{E}$ is the electric field. The path of antiprotons, positrons, and other charged particles will be heavily influenced by the magnetic field of a planet. As described by Walt (1994), the magnetic field potential of the Earth is,

$$\psi = R_E \sum_{n=1}^{\infty} \left(\frac{R_E}{r} \right)^{n+1} \sum_{m=1}^{n} g_n^m \left(\cos m\phi + h_n^m \sin m\phi \right) P_n^m (\cos\theta), \tag{A.4}$$

where R_E is the radius of the Earth, r, θ, ϕ are the position variables of the point being considered, and the other terms are constants which represent empirically derived field parameters for the planet. The lowest order, and dominant term, of the Earth's magnetic field is a simple dipole.

When under the influence of the magnetic field, some fraction of internally generated particles is properly aligned to become trapped in the magnetic field of the Earth. This is identical to the normal trapping that occurs with protons, electrons and other nuclei to form the Van Allen radiation belts of the planet. The trapped particles follow a trajectory that spirals around magnetic field lines as shown in figure (A.3).

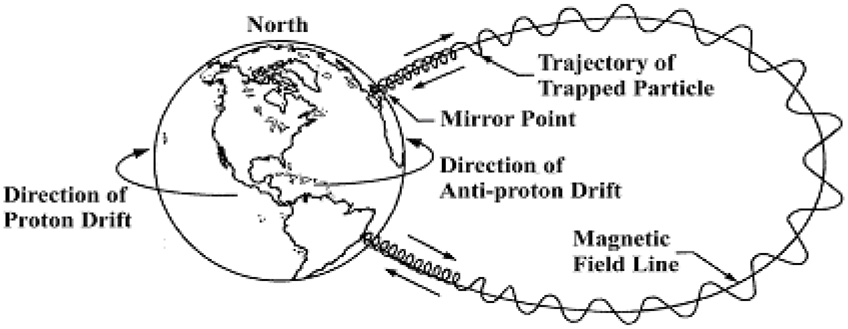

Figure A.3 - Trapped charged particle motion in a magnetic field

The gyroradius, or the distance between the mean trajectory (guiding center) and the spiral radius is,

$$\rho = \frac{p_\perp}{Bq} = \frac{m_0 \gamma v_\perp}{Bq} \qquad A.5$$

where $v_\perp$ is the particle's velocity perpendicular to the mean trajectory and γ is the relativistic correction factor for high-energy particles. Particles of opposite charge will spiral in the reverse direction of each other.

The particles are trapped due to the influence of a mirroring force as the particle approaches the higher field strength near the poles. The mirror force,

$$F_z = -q v_\perp \frac{\rho}{2} \frac{\partial B_z}{dz} \qquad A.6$$

is independent of the polarity of the particle's charge and forces the particle to bounce between mirror points in the Northern and Southern hemispheres. The pitch angle α,

$$\tan\alpha = \frac{v_\perp}{v_\parallel} \qquad A.7$$

is modified due to the mirror force as it approaches the mirror point near the poles. At a pitch angle of 90^0, the particle has been effectively repelled and bounces back to its mirror point in the opposite hemisphere. The approximate bounce period for Earth,

$$\tau_b = 0.117\left(\frac{R_0}{R_E}\right)\frac{1}{\beta}\left[1 - 0.4635\left(\sin\alpha_{eq}\right)^{3/4}\right]\text{sec} \qquad A.8$$

is a function of the equatorial crossing distance R_o, and equatorial pitch angle α_{eq}, along with the velocity relative to light, β. The trapped particles are slowly transported through various diffusion processes (e.g. magnetic field fluctuations) (Schultz and Lanzerotti, 1974) until a quasi-static balance between the source and loss functions is ultimately reached (Spjeldvik, 1977). The radiation belt can be described as a six dimensional average phase space density (*f*) where the components represent the three position and three momentum values for the trapped particle population. The time evolution of the generated radiation belts in phase space is described by diffusion coupled with appropriate source and loss terms such that,

$$\frac{\partial f}{\partial t} = L^2 \frac{\partial}{\partial L}\left[\frac{D_{LL}}{L^2}\frac{\partial f}{\partial L}\right] + Sources + Losses, \qquad A.9$$

where L is the magnetic shell that the particle is traversing and D_{LL} is the diffusion constant, which describes the radial diffusion of the particles due to the collective action of various natural mechanisms operating in the magnetosphere. These combined processes produce a quasi-static radiation belt of charged particles resident in the magnetic field lines of the planet. Barth et al. (2003) and Hargreaves (1992) describe the pertinent models for the environment surrounding the Earth. The empirically derived AP8 radiation belt model shown in Figure A.4 gives the resulting fluxes expected for protons trapped in the Earth's radiation belts.

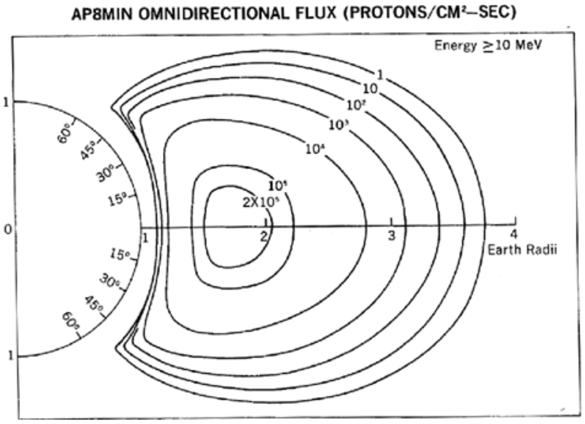

Figure A.4 – Radiation belt proton fluxes (AP8).

Though traditionally the radiation belts are thought to be comprised mostly of high-energy protons and electrons, antiparticles that are otherwise identical (aside from their charge) can be similarly trapped provided there is an appropriate internal source mechanism. The pair production mechanism described in equation (2) can act as such a source to populate the belt with antiprotons either directly or through antineutron decay. A similar number of antiprotons and antineutrons are produced in the atmosphere though antineutron decay is the dominant source.

Fewer of the directly produced antiprotons from the antiproton belt since there is a fine balance between the generation and loss processes. Unlike the neutral antineutrons, which can travel unimpeded through the magnetosphere to decay somewhere deep in the radiation belts, antiprotons are immediately trapped along the L-shell where the pair production took place. Therefore, most of the antiprotons will be produced deep in the atmosphere where loss rates are high thereby yielding a negligible trapped flux. Loss rates are lower at higher altitudes but there is less source material (atmosphere) which results in a low interaction cross section for pair production. The peak production and trapping occurs at an altitude of approximately 1200 km. (Pugacheva, 2002)

APPENDIX B – EXPERIMENT SCALING

The operation of the collection system can be verified with experiments. In particular, the ability to transfer external particles to the inner field lines of the mini-magnetosphere for trapping needs to be evaluated. This can be accomplished by appropriately scaling the full system to laboratory dimensions. The high-energy antiproton flux can be replaced with low energy electrons generated from a filament source. Initial experiments should evaluate the ability to divert the current onto closed magnetic field lines, by simply inserting a collection electrode at the local potential. Follow-on experiments could evaluate the time evolution of particle density in the trap either by inserting a Langmuir probe, or by dumping the accumulated charge into a collector plate after ever-increasing time intervals.

Scaling the system presents a particular challenge. Table (B.1) shows the relevant parameters of the full-scale system compared to two representations scaled for laboratory experimentation. Key terms that are to be held constant are the ratio between the coil radius and the particle gyro radius, the magnetic field mirror ratio, and the trap stability parameter related to the Larmor radius relative to the radius of curvature of the field lines. The magnetic field strengths shown for the two experimental configurations are below the ambient Earth magnetic field and will require either active or passive shielding to be achieved. This reduced field strength is necessary to limit the dipole current to a level that is readily achievable at the required length scale. To provide uniformity of the field to this level, a passive shielding of mumetal is preferred. The more restrictive (0.2 micro-Tesla) value can be achieved using a 0.3 mm layer of mumetal around the inside of the test chamber. This is approximately the size of the thinnest foil that is commercially available, and is easily obtained.

Parameter	**Full Scale**	**Experiment 1**	**Experiment 2**
B_0 (Background B-field)	30 μT	3 μT	0.3 μT
I_0 (Operating current)	10^5 A	10^5 A	10^5 A
n (Plasma density)	2 (10^{16}) m^{-3}	5 (10^{20}) m^{-3}	5 (10^{19}) m^{-3}
R_0 (RMF antenna loop radius)	100 m	10 cm	10 cm
m (Particle mass)	1.7 (10^{-27}) kg	9.1 (10^{-31}) kg	9.1 (10^{-31}) kg
E (Particle energy)	250 MeV	50 eV	0.5 eV
q (Particle charge)	-1.6 (10^{-19}) C	-1.6 (10^{-19}) C	-1.6 (10^{-19}) C

Table B.1 – Particle lifetimes for full- and laboratory-scale scenarios.

One aspect of the experiment that can be completely scaled when the antiprotons are replaced with electrons is the loss due to synchrotron radiation. For a charged relativistic particle moving in a magnetic field, the synchrotron power loss is given by,

$$P_{synchrotron} = \frac{q^2}{6\pi\varepsilon_0 c^3} a \,. \qquad \text{B.1}$$

From the standard definitions of relativistic velocity, acceleration, and gamma,

$$v = c\sqrt{1 - {m_0}^2 c^4 / E^2} \,, \qquad \text{B.2}$$

$$a \equiv \gamma^2 v^2 / r_g, \tag{B.3}$$

$$\gamma \equiv 1/\sqrt{1 - v^2/c^2}, \tag{B.4}$$

and the expression for the radius of gyration,

$$r_g = \gamma m_0 v / qB, \tag{B.5}$$

we may express equation (B.1) as,

$$P_{synchrotron} = \frac{E^2 B^2 q^4}{6\pi\varepsilon_0 {m_0}^4 c^5}\left(1 - \frac{{m_0}^2 c^4}{E^2}\right). \tag{B.6}$$

For a given energy, the radiated power for electrons exceeds that for antiprotons by 13 orders of magnitude! This loss mechanism must be accounted for if electron trapping experiments are to be carried out on a laboratory scale. Table (B.1) illustrates the relative lifetimes of trapped particles in a magnetic field. Scaled confinement of individual electrons is limited to timescales on the order of minutes to hours, presenting ample opportunity to carry out any necessary measurements or observations.

	Full Scale	***Test Case 1***	***Test Case 2***
Particle	*Antiproton*	*Electron*	*Electron*
B Field Strength	628.35mT	41.41mT	4.14mT
Kinetic Energy	1GeV	1.4eV	0.015eV
Lifetime	368.373 yrs	25.063 min	41.772 hrs

Table B.2 – Particle lifetimes for full- and laboratory-scale scenarios.

APPENDIX C – DRIFT VELOCITIES

Drift	Expression
Gravitational	$\vec{v}_g = \frac{m}{q}\frac{\vec{g}\times\vec{B}}{B^2}$
Electric Field ($\vec{E}\times\vec{B}$)	$\vec{v}_E = \frac{\vec{E}\times\vec{B}}{B^2}$
Non-uniform Electric Field	$\vec{v}_E = (1+\frac{1}{4}{r_L}^2\nabla^2)\frac{\vec{E}\times\vec{B}}{B^2}$
Grad-*B*	$\vec{v}_{\nabla B} = \frac{\varepsilon_\perp}{qB}\frac{\vec{B}\times\nabla B}{B^2}$
Curvature	$\vec{v}_R = \frac{\varepsilon_\parallel}{qB}\frac{\vec{R}_c\times\vec{B}}{{R_c}^2 B}$
Polarization	$\vec{v}_p = \frac{m}{qB^2}\frac{d\vec{E}}{dt}$
Diamagnetic	$\vec{v}_D = -\frac{\nabla p\times\vec{B}}{qnB^2}$

REFERENCES

- Agostinelli et al., "Geant4: A Simulation Toolkit", *Nuclear Instruments and Methods.* A506:250-303, 2003.
- Augenstein, B.W., "RAND Workshop on Antiproton Science and Technology, October 6-9,1987: Annotated Executive Summary," *RAND Note N-2763-AF*, October 1988.
- Aguilar, M., et al., "The Alpha Magnetic Spectrometer (AMS) on the International Space Station: Part I – results from the test flight on the space shuttle", *Physics Reports* 366, pg 331-405, 2002.
- Barker, D.L, N. Shah, H. Schmitt, "High Density Storage of Excited Positronium Using Photonic Bandgap Traps", US Patent #6,813,330, November 2, 2004.
- Barth, J.L., C.S. Dyer, and E.G. Stassinopoulos, "Space, Atmospheric, and Terrestrial Radiation Environments", *IEEE Transactions on Nuclear Science*, Vol. 50, No. 3, June 2003.
- Bickford, J., "Extraction of Antiparticles Concentrated in Planetary Magnetic Fields", *NIAC Phase I Final Report*, March 2006.
- Biermann, P.L. and G. Sigl, "Introduction to Cosmic Rays", arXiv:astro-ph/0202425 v1 22 Feb 2002
- Bilitza, D. "International Reference Ionosphere 2000", *Radio Science,* 36, #2, 261-275, 2001.
- Brillouin, L, "A Theorem of Larmor and Its Importance for Electrons in Magnetic Fields", *Physical Review*, Vol. 67. No. 7-8, April 1 and 15, 1945.
- Bussard, R.W., "Galactic matter and interstellar flight", *Astronautica. Acta.* Vol 6, pp 179-94, 1960.
- Cassenti, B.N., "Concepts for the Efficient Production and Storage of Antimatter," *AIAA–93–2031*, presented at the 29th Joint Propulsion Conference, Monterey, CA, Jun 28–30, 1993.
- Cassenti, B., "Mass Production of Antimatter for High-Energy Propulsion", *Journal of Propulsion and Power*, Vol. 16, No. 1, January-February 2000.
- Chapline, G. "Antimatter Breeders," *Journal of the British Interplanetary Society*, Vol 35, pp. 423–424, 1982.
- Chen, F.F., "Introduction to Plasma Physics", *Plenum Press*, 1974.
- Cheng, A., et al., "Energetic Ion and Electron Phase Space Densities in the Magnetosphere of Uranus", *Journal of Geophysical Research*, Vol. 92, No. A13, December 30, 1987
- Chirikov, B.V., "Particle Dynamics in Magnetic Traps", *Reviews of Plasma Physics*, Vol. 13, 1987.
- Cooper, J., "Nuclear Cascades in Saturn's Rings: Cosmic Ray Albedo Neutron Decay and Origins of Trapped Protons in the Inner Magnetosphere", *Journal of Geophysical Research*, Vol. 88, No. A5, pgs 3945-4954, May 1, 1983.
- Cornwall, J. M.: "Radial Diffusion of Ionized Helium and Protons: A Probe for Magnetospheric Dynamics", *Journal of Geophysical Research*, 77, 1756, 1972.
- Derome, L, "Atmospheric Protons and Antiprotons from sea level to satellite altitudes", *28th International Cosmic Ray Conference*, pgs. 2069-2071, 2003.
- Dessler, A. J. (editor), "Physics of the Jovian Magnetosphere", Cambridge University Press, 1983.
- Divine, N., and H. B. Garrett, "Charged Particle Distributions in Jupiter's Magnetosphere", *Journal of Geophysical Research*, Vol. 88, No. A9, pgs. 6889-6903, September 1, 1983.
- Edwards, K., "Propulsion and Power with Positrons", NIAC Fellows meeting presentation, March 24, 2004.
- Forward, R. L., "Antiproton Annihilation Propulsion", *AFRPL TR-85-034*, September 1985.
- Forward, R. L, and J. Davis, "Mirror Matter: Pioneering Antimatter Physics", *Wiley,* 1988.
- Gaidos, G., et al, "Antiproton- Catalyzed Microfission/Fusion Propulsion Systems for Exploration of the Outer Solar System and Beyond," AIAA 98-3589, July 1998.
- Goertz, C., "Further observational support fo rtht lossy radial diffusion model of the inner Jovian magnetosphere", *Journal of Geophysical Research*, Vol. 84, pg 87-92, 1979.
- Gray, L., and T. E. Kalogeropoulos, "Possible Bio-Medical Application of Antiprotons", *IEEE Transactions in Nuclear Science*, Vol. NS-29, No. 2, April 1982.
- Greaves, R.G., and C.M. Surko, "Antimatter Plasmas and Antihydrogen", *Physics of Plasmas*, 4(5), May 1997.
- Gubar, Y., "A Simple Analytical Model for Radial Diffusion of Charged Particles in the Magnetospheres of Jupiter, Saturn, and Uranus", *Cosmic Research*, Vol. 39, No. 1, 2001, pp. 101–104. Translated from Kosmicheskie Issledovaniya, Vol. 39, No. 1, 2001, pp. 109–112.

- Gusev, A., A., I. M. Martin, G. I. Pugacheva, A. Turtelli, and W. N. Spjeldvik, "Energetic Positron Population in the Inner Zone", *Il Nuovo Cimento*, vol. 19C, No. 4, p.461-467, 1996.
- Gusev, A. A., U. B. Jayanthi, I. M. Martin, G. I. Pugacheva and W. N. Spjeldvik, "Nuclear Reactions in the Uppermost Earth Atmosphere as a Source for the Magnetospheric Positron Radiation Belt" , *J. Geophys. Res.*, vol. 106, No. A11, p. 26111-26115, 2001.
- Gusev, A.A., U.B. Jayanthi, K.T. Choque, G. I. Pugacheva, N. Schuch and W.N. Spjeldvik, "Antiproton radiation belt produced by cosmic rays in the Earth's magnetosphere.", *Geophysical Research Letters*, Vol.30, No. 4, 1161, 2003.
- Gusev, A.A., U.B. Jayanthi, I.M. Martin, G. I. Pugacheva, and W.N. Spjeldvik, "On Positron Radiation Belt in the Earth's Magnetosphere.", *Brazilian Journal of Physics*, Vol. 30, No. 3, Sept. 2003.
- Hargreaves, J.K., "The Solar-Terrestrial Environment", *Cambridge Atmospheric and Space Science Series*, 1992.
- Hedin, A. E., "MSIS-86 Thermospheric Model", *Journal of Geophysical Research*, 92, 4649, 1987.
- Heitler, W., "The Quantum Theory of Radiation", Clarendon Press, Oxford, England, 1954.
- Hill, T.W., "Origin of the plasma sheet", *Rev Geophysical Space Physics* 12:379-388, 1974.
- Holzscheiter, M.H., R. A. Lewis, E. Mitchell, J. Rochet, and G. A. Smith, "Production and Trapping of Antimatter for Space Propulsion Applications", *AIP Conference. Proceedings*. 387, 1493 (1997)
- Howe, S., and G. Smith., "Enabling Exploration of Deep Space: High Density Storage of Antimatter", *NIAC Phase I Final Report*, April 1998.
- Huang, C.Y., L. Derome, and M. Buenerd, "Secondary Antiproton Flux Induced by Cosmic Ray Interactions with the Atmosphere", *Physical Review D.*, Vol 68, pgs 053008, 2003.
- Hudson, M.K., et al., "Radiation Belt Formation during Storm Sudden Commencements and Loss During Main Phase", *Advances in Space Research*, 21(4), pgs 597-607, February 1998.
- Haloulakos, V., and A. Ayotte,, "The Prospects For Space-Based Antimatter Production", *AIAA-91-1987*, Joint Propulsion Conference, Sacramento, CA, June 24-26, 1991.
- Hood, L, "Radial Diffusion in Saturn's Radiation Belts: A Modeling Analysis Assuming Satellite and Ring E Absorption", *Journal of Geophysical Research*, Vol. 88. No. A2, pgs 808-818, Feb 1, 1983.
- Hora, H., "Estimates of the Efficient Production of Antihydrogen by Lasers of Very High Intensities," *OptoElectronics*, Vol 5, 1973, pp. 491–501.
- Hovestadt, et al., "Evidence for Solar Wind Origin of Energetic Heavy Ions in the Earth's Radiation Belt", *Geophysical Research Letters*, Vol. 5, No. 12, December 1978.
- Howe, S.D., and G. P. Jackson, "Antimatter Driven Sail for Deep Space Exploration", NIAC 2004 Fellows Meeting Presentation, October 2004.
- Ifedili, S.O., "Atmospheric Neutrons and Their Contributions to the Earth's Radiation Belts", *Journal of Geomagnetic and Geoelectric*, **43**, 255-266, 1991.
- Isakowitz, S.J., Hopkins, J.B., and Hopkins, J.P, Jr., "International Reference Guide to Space Launch Systems." Fourth Edition, 2004.
- Jackson, G., "Commercial Production and Use of Antiprotons", *Proceedings of EPAC 2002*, Paris, France, 2002.
- Jackson, G., "Antimatter Harvesting in Space", *NIAC Phase I Final Report*, March 2006.
- Jentsch, V., "On the Role of External and Internal Source In Generating Energy and Pitch Angle Distributions of Inner-zone Protons*", Journal of Geophysical Research*, Vol. 86, p.701-710, Feb 1981.
- Kallenrode, M., "Space Physics: An Introduction to Plasmas and Particles in the Heliosphere and Magnetospheres", *Springer Books*, pg 367, 2004.
- Krasheninnikov, S., P. Catto, and R.D. Hazeltine. "Magnetic Dipole Equilibrium Solution at Finite Plasma Pressure." *Physical Review Letters*, Volume 82, Number 13, 29 March 1999.
- Kress, B.T., M.K. Hudson, K.L. Perry, and P.L. Slocum, "Dynamic Modeling of Geomagnetic Cutoff for the 23-24 November 2001 Solar Energetic Particle Event", *Geophysical Research Letters*, Vol. 31, L04808, doi:10.1029/2003GL018599, 2004.
- Labrador, A. W., and R.A. Mewaldt, "Effects of Solar Modulation on the Low-Energy Cosmic-Ray Antiproton/Proton Ratio", *The Astrophysical Journal*, 480:371-376, 1997 May 1.
- LaPointe, M. R., "Antimatter Production at a Potential Boundary," *Joint Propulsion Conference and Exhibit,* July 2001, AIAA-2001-3361.

- Larson, W. et al., "Human Spaceflight: Mission Analysis and Design", McGraw Hill Space Science Series, 2004.
- Letaw, J.R., R. Silverberg, C.H. Tsao, "Proton-nucleus total inelastic cross sections – an empirical formula for E greater than 10 MeV", *Astrophysical Journal Supplement Series*, Vol. 51, pgs. 271-275, March 1983.
- Lyons, L. and R. M. Thorne: "Equilibrium Structure of Radiation Belt Electrons", *Journal of Geophysical Research*, 78, 2142, 1973.
- MIT, "Electric and Magnetic Field Lenses", 22.09 Chapter 6 lecture notes, available online at 'http://www.mit.edu/afs/athena/course/22/22.09/ClassHandouts/Charged%20Particle%20Accel/CHAP06.PDF', last accessed, August 30, 2007.
- Montgomery, D.B., and J. Terrell, "Some Useful Information for the Design of Air-Core Solenoids", Francis Bitter National Magnet Laboratory, 1961.
- Moskalenko, I.V., A. W. Strong, J. F. Ormes, and M.S. Potgieter, "Secondary Antiprotons and Propagation of Cosmic Rays in the Galaxy and Heliosphere", *The Astrophysical Journal*, 564, January 10, 2002.
- Nicholson, P. D., and L. Dones, "Planetary Rings", *Reviews of Geophysics*, Supplement, pgs 313-327, April 1991.
- Northrop, T.G., "The Adiabatic Motion of Charged Particles", *Interscience Publishers*, 1963.
- Picozza, P., and A. Morselli, "Antimatter research in space"*, Journal of Physics G: Nuclear and Particle Physics*, 29 (2003), 903-911.
- Pugacheva, G., A.A. Gusev, U.B. Jayanthi, N.J. Schuch, W.N. Spjeldvik, and C. H. Choque, "Antiprotons confined in the Earth's inner magnetosphere", *Astroparticle Physics* 20, pgs 257-265, 2003.
- Roederer, J. G., Dynamics of Geomagnetically Trapped Radiation, Springer-Verlag,New York, 1970.
- Rossi, B. and S. Olbert, "Introduction to the Physics of Space", McGraw Hill, 1970.
- Sanger, E., "The Theory of Photon Rockets," *Ing. Arch.*, Vol 21, 1953.
- Selesnick R. et al., "A theoretical model of the inner proton radiation belt", *Space Weather*, Vol. 5, S04003, 2007.
- Schmidt, G.R., H.P. Gerrish, J.J. Martin, G.A. Smith, and K.J. Meyer, "Antimatter Production for Near-term Propulsion Applications", *Joint Propulsion Conference and Exhibit*, Los Angles, CA, 1999, AIAA-99-2691.
- Schmidt, G.R., H.P. Gerrish, J.J. Martin, G.A. Smith, and K.J. Meyer, "Antimatter Requirements and Energy Costs for Near-Term Propulsion Applications", *Journal of Propulsion and Power*, Vol. 16, No. 5, September-October 2000.
- Schulz, M., "The Magnetosphere" in "Geomagnetism" edited by J.A. Jacobs, Vol 4. pp 202, *Academic Press*, 1991.
- Schulz, M. and L.J. Lanzerotti, "Particle Diffusion in the Radiation Belts", *Springer-Verlag*, 1974.
- Schwadron, N., and T. Cravens, "Implications of Solar Wind Composition for Cometary X-Rays", *The Astrophysical Journal*, 544:558-566, 2000.
- Share, G. H. et al, "High-Resolution Observation of the Solar Positron-Electron Annihilation Line", *The Astrophysical Journal*, 595:L85-L88, 2003 October 1.
- Sina, R., et al., "Antiproton Spectrum in the Galactic Wind Model", *Adv. Space Res.* Vol. 27, No. 4, pp705-710, 2001.
- Slough, J. "The Plasma Magnet", *NIAC Phase II Final Report*, 2006.
- Spjeldvik, W. N., "Equilibrium Structure of Equatorially Mirroring Radiation Belt Protons", *Journal of Geophysical Research*, Vol. 82, No. 19, July 1, 1977.
- Spjeldvik, W. N.: "Expected Charge States of Energetic Ions in the Magnetosphere", *Space Science Reviews*, 23, 499-538, 1979.
- Spjeldvik, W.N., A.A. Gusev, I.M. Martin, G.I. Pugacheva, S. Bourdarie, and N.J. Schuch, "Theory for Antiproton Content of Planetary Magnetospheres", *IAGA-Scientific Symposia*, Toulouse, France; July 18-29, 2005.
- Störmer, C., "The Polar Aurora", *Oxford University Press*, 1950.
- Tan, L.C., and L.K. Ng, "Calculation of the Equilibrium Antiproton Spectrum*", Journal of Physics G: Nuclear Physics*, 9, pgs. 227-242, 1983.

- Walt, M., “Introduction to Geomagnetically Trapped Radiation”, *Cambridge University Press*, 1994.
- Zubrin, R., “The Magnetic Sail”, *Phase I NIAC Final Report*, January 7, 2000.